

Template-assisted electrodeposition of nickel and nickel copper 3D microcomponents

Présentée le 29 juin 2020

à la Faculté des sciences et techniques de l'ingénieur
Unité de rattachement pour scientifiques IMX
Programme doctoral en science et génie des matériaux

pour l'obtention du grade de Docteur ès Sciences

par

Patrik SCHÜRCH

Acceptée sur proposition du jury

Prof. C. Ludwig, président du jury
Prof. F. Nüesch, Dr L. V. S. Philippe, directeurs de thèse
Prof. A. West, rapporteur
Prof. S. Pané i Vidal, rapporteur
Dr S. Mischler, rapporteur

Acknowledgements

After years of work for this thesis, I would like to thank the people who made it possible. I would like to thank Laetitia Philippe and Frank Nüesch for the supervision and to Johann Michler for the opportunity to work in his laboratory. To all of my collaborators, even though collaboration was not always as successful as we had hoped for. To my fellow coworkers and office mates for the support and helping hands as well as the good times spent at work or at Rosie's. Furthermore, to my family and friends for all their support.

All in all, this was a wonderful, interesting and challenging experience.

Thun, 17.04.2018

P.S.

Abstract

New types of metamaterials and architected material require metallic materials with precise structural design in the microscale. However, additive manufacturing of metallic structures in the microscale has proven difficult, as the demand for the material quality and accuracy of the 3D structure is high. Of the multitude of techniques available, template-assisted electrodeposition (TAE), also known by its German abbreviation, LIGA, has shown excellent results for the production of 2D components. With new lithography techniques, especially two-photon lithography (TPL), TAE shows promise of microscale additive manufacturing for 3D metal structures.

This thesis aims to investigate the electrodeposition into a 3D template and discuss the influence of the template on the local current density and the resulting microstructure of the deposit. 3D finite element simulations were used to understand the process of template filling. The electrodeposited structures were investigated towards their shape accuracy as well as their microstructure. Various deposited structures were used for micromechanical investigation with the explicit regard of inspecting their properties and performance for future use in MEMS-devices. Simple pillars were investigated at first to inspect the mechanical properties and arrangement of the templates in arrays. In this work, subsequently, 3D micro springs were produced and their properties compared with theoretical mechanical simulations. These springs exhibited significant strength, unprecedented in microsprings of this size.

Following simple templates, more complex templates with multiple ongoing growth fronts were examined. Micromechanical shear test specimen were produced and the template design was investigated. These templates were also used to investigate the effectiveness of pulse electrodeposition was investigated to fill corners. Furthermore, the microstructure showed elongated grains along the growth direction allowing insight into the deposits growth. Where to growth fronts meet an accumulation of grain boundaries was visible in the microstructure, but showed no porosity. Building on these results, microlattices with a body center cubic structure were designed and tested. The microlattices showed remarkably high strength as well as excellent promise for energy absorption. Building on the success of the technique and the previous structures, the electrodeposition of Copper Nickel alloys was investigated. A 3D time-dependent pulse electrodeposition simulation was created and the deposition of large 2D components were simulated and compared to experimental values.

Overall, through these specific case studies, it was shown that TAE combined with TPL produces microcomponents with excellent accuracy, homogenous microstructures with no significant defects and excellent mechanical properties. The method has shown reproducibility. The

insight gained by the electrodeposition simulation can be used in the future for others to emulate the process or create their electrodeposition simulation.

keywords: electrodeposition, additive manufacturing, nanocrystalline nickel, two-photon lithography

Zusammenfassung

Neue Metamaterialien und Materialien mit einer auferlegten 3D Struktur benötigen additive Herstellungsverfahren im mikroskaligen Bereich. Diese Verfahren sind technisch anspruchsvoll um Metallstrukturen herzustellen, die sowohl den qualitativen Ansprüchen bezüglich der Mikrostruktur wie auch dem Präzisionsanspruch an die Geometrie gerecht werden. Eine der vielversprechendsten Methoden für die Herstellung von mikroskaligen Metallstrukturen ist eine Kombination aus Lithographie und galvanischer Abscheidung. Diese Technik ist auch bekannt als LIGA (Lithographie, Galvanik, Abformung) und wird häufig verwendet zur Herstellung von 2D Mikrokomponenten. Mit neuen Lithographietechniken wie der Multiphotonlithographie ist es möglich 3D Formen zu kreieren, die danach durch Galvanik mit Metall aufgefüllt werden können. Die Kombination aus dem LIGA-Verfahren mit der Zweiphotonlithographie ist eine vielversprechende Technik zur Herstellung von 3D Metallstrukturen mit mikroskaliger Präzision.

In dieser These wurde die galvanische Abscheidung in eine 3D Form zu untersuchen und den Einfluss der Geometrie der Form auf die Galvanik und das abgeschiedene Material untersucht. Ein 3D finite Elemente Modell der galvanischen Abscheidung von nanokristallinen Nickel wurde entwickelt um den Einfluss der Geometrie zu verstehen. Die hergestellten Strukturen wurden dann bezüglich der Präzision zum ursprünglichen Design verglichen und auch die Mikrostruktur des abgeschiedenen Metalls wurde untersucht. Einige der hergestellten Strukturen wurden dann auch auf ihre mechanischen Eigenschaften getestet, um deren zukünftigen Einsatz als mikroelektromechanische Systemkomponenten zu evaluieren.

Anfangs wurden 2D Mikrosäulen aus nanokristallinem Nickel hergestellt um die mechanischen Eigenschaften des Materials zu testen und die Möglichkeit zur simultanen Herstellung von mehreren Strukturen zu untersuchen. Anschließend wurden 3D Mikrofedern hergestellt und die mechanischen Eigenschaften mit den theoretisch zu erwartenden verglichen. Diese Federn zeigten hohe mechanische Festigkeit.

Nach diesen Strukturen mit einer galvanischen Abscheidungsfront wurden 3D Formen mit mehreren zusammenwachsenden Abscheidungsfronten untersucht. Mikromechanische Scher-Test-Strukturen wurden hergestellt und verschiedene Lithographie-Formdesigns wurden untersucht. Diese Strukturen wurden mit Umkehr-Puls Abscheidung hergestellt und der Einfluss des Umkehr-Puls auf die Möglichkeit Ecken einer Form komplett zu füllen, wurde untersucht. Diese Nickelstrukturen besaßen eine Mikrostruktur mit länglichen Körnern in Wachstumsrichtung. Das Zusammenwachsen der zwei Abscheidungsfronten erzeugte eine nicht-poröse aber sichtbare Ansammlung von Korngrenzen. Auf diesen Resultaten

aufbauend wurden Mikrogitter hergestellt mit verschiedenen Wachstumsfronten mit kubisch-raumzentrierten Elementarzellen, mit mehr verschiedenen Wachstumsfronten. Diese Nickelgitter wurden mechanisch getestet und zeigten hohe Festigkeit für kubische raumzentriertes Design und eine vielversprechende Energie Absorbierung.

Als letztes Kapitel dieser Arbeit wurden die Abscheidung von einer Nickel Kupfer Metalllegierung untersucht. Ein 3D Finite Element Model wurde erstellt um die elementare Zusammensetzung der Abscheidung vorauszusagen. 2D Komponenten wurden hergestellt und die Zusammensetzung und Abscheidungsgeschwindigkeit mit dem Modell verglichen.

Zusammengefasst, wurde durch diese Fallstudien wurde gezeigt, dass das LIGA-Verfahren in Kombination mit Zweiphotonlithographie Mikrokomponenten mit exzellenter Präzision produzieren kann, die Strukturen eine homogene Mikrostruktur ohne grosse Defekte, und hervorragende mechanische Eigenschaften aufweisen. Mit diesem Verfahren können 3D Metallstrukturen reproduzierbar hergestellt werden. Das erstellte Model erzeugte neuen Einblick zur galvanischen Abscheidung in 3D Formen. Auf diese These kann in Zukunft aufgebaut werden um die Möglichkeiten dieses Verfahrens zu optimieren und weiter zu entwickeln.

Structure of the thesis

Template-assisted electrodeposition (TAE) is an attractive method for electrochemical additive manufacturing (ECAM) of 3D metallic microstructures. The method used in this work, i.e. electrodeposition into two-photon lithography templates, although rarely reported in literature, has many advantageous qualities. Most notably, template design has almost no geometrical limitations and there are extensive libraries of electrodeposable materials. This work was performed to highlight the potential of this technique for various applications.

The thesis was structured by first providing an introduction to the general applications of additively manufactured metal components and their use as metamaterials and microrobots, additionally showing the motivation for studying template-assisted electrodeposition. Afterwards, the difficulties and challenges of the above-mentioned technique are stated. In the methods and material section, a description of the electrodeposition process and simulations is given, as well as a more in-depth discussion on material selection. This includes listing the constituents of the electrolyte and explaining their role.

Next, the results and discussion section is presented. These results were divided into three parts. The first focuses on single pore templates, i.e. templates that have one ongoing electrodeposition front and no conjoining parts. These types of templates were the first to be reported in literature. The second proceeds to explain more complex structure with multiple conjoining growth fronts, such as in the case of lattices and micro-shear samples. The examples and explanations presented in the first two subsections include nanocrystalline nickel electrodeposition, whereas the third and final part focuses on the electrodeposition of nickel-copper alloys.

Lastly, the results are followed by a conclusion and outlook section, summarizing the most important aspects of this thesis and presenting the next possible steps for the development and application of this technique.

Contents

Acknowledgements	i
Abstract	iii
Zusammenfassung	v
Structure of the thesis	vii
List of figures	x
List of tables	xii
Nomenclature	xv
1 Introduction	1
1.1 Architected materials	1
1.1.1 Applications of architected materials	2
1.2 Manufacturing	4
1.2.1 Two-photon Lithography (TPL)	6
1.2.2 Template-assisted electrodeposition (TAE)	6
1.2.3 Nanocrystalline materials	9
2 Statement of the problem	11
3 Methods and techniques	15
3.1 Electrodeposition	15
3.1.1 Nickel electrodeposition	21
3.2 Electrodeposition simulation	22
3.2.1 Finite element - simulation	24
3.3 Lithography and templates	27
3.4 Micromechanical characterisation	30
4 Single pore templates	31
4.1 Nanocrystalline micropillars	31
4.1.1 Introduction and aims	31
4.1.2 Methods	32
	ix

Contents

4.1.3	Results and discussion	33
4.1.4	Conclusion	35
4.2	Nanocrystalline nickel microsprings	36
4.2.1	Introduction and aims	36
4.2.2	Methods	37
4.2.3	Results and discussion	40
4.2.4	Conclusion	46
5	Complex templates	49
5.1	Nanocrystalline nickel microshear structures	49
5.1.1	Introduction and aims	49
5.1.2	Methods	50
5.1.3	Model architecture	52
5.1.4	Results and discussion	53
5.1.5	Conclusion	58
5.2	Nanocrystalline nickel microlattices	59
5.2.1	Introduction and aims	59
5.2.2	Methods	60
5.2.3	Results and discussion	60
5.2.4	Conclusion	63
6	Copper nickel electrodeposition	65
6.1	Nanocrystalline copper nickel deposition	65
6.1.1	Introduction and aims	65
6.1.2	Methods	67
6.1.3	Results and discussion	72
6.1.4	Conclusions	78
7	Conclusion and Outlook	79
	Bibliography	82
	Abstract	99
	Curriculum Vitae	109

List of Figures

1.1	Material properties of architected materials	2
1.2	Periodic table of electrodepositable elements	3
1.3	Resolution of additive manufacturing methods	5
1.4	Electrodeposited 3D structures in literature	8
2.1	Challenges in 3D electrodeposition	12
2.2	Chapters of this thesis	13
3.1	Electrodeposition schematic	16
3.2	Double layer schematic	17
3.3	Electrolyte flux	19
3.4	Meshing in the FEM simulation	26
3.5	TPL writing Configuration	28
3.6	TPL writing Modes	30
4.1	NC-nickel pillars: Electrodeposition simulation	34
4.2	NC-nickel pillars:SEM image of pillar arrays	34
4.3	NC-nickel pillars:TEM images of nc-nickel and mechanical testing response of the pillars	35
4.4	NC-nickel microsprings: Inversion deposition process	38
4.5	NC-nickel microsprings: Electrodeposition simulation boundary conditions	40
4.6	NC-nickel microsprings: Simulation of electrodeposition into pores with variable surface area	41
4.7	NC-nickel microsprings: Simulation of electrodeposition into pores with variable 3D shapes	42
4.8	NC-nickel microsprings: SEM-images	44
4.9	NC-nickel microsprings: Monotonic testing	45
4.10	NC-nickel microsprings: Cyclic loading of the nc-nickel microsprings	46
5.1	NC-nickel microshear specimen: Macroscopic 2D simulation of electrodeposition in the electrochemical cell	53
5.2	NC-nickel microshear specimen: Electrodeposition simulation verification experiments	54
5.3	NC-nickel microshear specimen: 3D design	54

List of Figures

5.4	NC-nickel microshear specimen: Simulation of nickel deposition into different templates	56
5.5	NC-nickel microshear specimen: Simulation of reverse pulse deposition into different templates	57
5.6	NC-nickel microshear specimen: SEM-images	58
5.7	NC-nickel microshear specimen: Local current density simulation results versus nickel microstructure	58
5.8	NC-nickel microlattices: SEM images	61
5.9	NC-nickel microlattices: Mechanical testing	62
5.10	NC-nickel microlattices: Deformation and energy absorption of microlattices .	63
5.11	NC-nickel microlattices: Ashby plot	64
6.1	Copper nickel: Electrodeposition simulation boundaries	73
6.2	Copper nickel: Linear sweep voltammetry and images of T-structures	74
6.3	Copper nickel: XRD of thin films	75
6.4	Copper nickel: Thin film cross-section	76
6.5	Copper nickel: T-component deposition	77
6.6	Copper nickel: Microgear	78
7.1	Highlights of the chapters	81
1	Appendix: Number of publications - AM versus EcAM	99
2	Appendix: XRD measurements of nc-nickel microsprings	101
3	Appendix: Nc-nickel microsprings: Pre and post compression	101
4	Appendix: Nickel sulfamate electrolyte CV	102
5	Appendix: Nickel sulfamate electrolyte Tafel plot	103
6	Appendix: Nickel sulfamate electrolyte chronoamperometry	104
7	Appendix: XRD of nc-nickel microshear specimen	105
8	Appendix: EDX of copper nickel thin films	105
9	Appendix: Boundary conditions of the micro-gear deposition simulation	106
10	Appendix: FE-meshing of the micro-gear deposition simulation	106
11	Appendix: FE-meshing of the T-components deposition simulation	107

List of Tables

4.1	NC-nickel microsprings: Calculated and simulated spring frequencies	46
6.1	Copper nickel: Electrodeposition simulation parameters	71
6.2	Copper nickel: Texture coefficients	74
1	Appendix: Electrodeposition Simulation parameters for nc-nickel microsprings	99
2	Appendix: Mechanical testing simulation parameter for the nc-nickel microsprings	100
3	Appendix: NC- nickel springs	100
4	Appendix: Electrolyte Constituents of copper nickel electrolyte	100
5	Appendix: EDX measurements of CuNi thin film cross-section	100

Nomenclature

EcAM - Electrochemical additive manufacturing

TAE - Template-assisted electrodeposition

TPL - Two-photon lithography

MM - Metamaterial

AM - Architected material

ELD - Electroless deposition

ALD - Atomic layer deposition

PVD - Physical vapor deposition

CVD - Chemical vapor deposition

nc - nanocrystalline

IHP - Inner Helmholtz plane

OHP - Outer Helmholtz plane

HER - Hydrogen evolution reaction

OCP - Open-circuit potential

W_a - Wagners number

k - Electrolyte conductivity

L - Characteristic length

η_{app} - Overpotential

P_l - Leveling parameter

i - Total current

i_{lim} - Limiting current

Nomenclature

i_l - Current density vector

i_{loc} - Local current density

i_0 - Exchange current density

a - Symmetry factor

η_{app} - Applied overpotential

η_{eq} - Equilibrium potential

N_M - Total flux

D_M - Diffusion coefficient

c_M - Concentration of species M

$R_{M,tot}$ - Total flux

z_M - Charge of species M

u_M - Induced flux

F - Faraday constant

t - Time

R - Gas constant

T - Temperature

σ_l - Electrolyte conductivity

φ_l - Electrode potential

Q_l - Sink

α_a - Charge transfer coefficient anode

α_c - Charge transfer coefficient cathode

ρ_M - Density of species M

ITO - Indium tin oxide

FTO - Fluorine tin oxide

BCC - body-centered cubic

1 Introduction

Declaration of contribution: Parts of this introduction are taken from a submitted book chapter "4.11 Composite Metamaterials: types and synthesis" which has been written by Patrik Schürch under supervision of Laetitia Philippe for the book *Encyclopedia of Materials: Composites* by Elsevier.

1.1 Architected materials

Metamaterials (MMs) or architected materials (AMs) have emerged as a new frontier of science involving physics, material science, engineering, and chemistry. These AMs have been described in a broad term as structures with an imposed geometry to fit an intended use. The properties of such 3D architected structures are a combination of the architecture, the size of features within the architecture, the microstructure and the inherent properties of the material. Introducing architecture can significantly alter some material properties and can even introduce the aforementioned exotic MM properties, such as negative refractive indices [1], negative thermal expansion [2], negative Poisson ratio [3, 4] and photonic bandgaps [5] amongst other properties. Nowadays architected structures are already incorporated or on the verge of incorporation for industrial applications in photovoltaics [6], microelectromechanical systems [7, 8], lightweight materials [9, 10, 11, 12], mechanics [13, 14, 15], energy storage [16, 17] and sensing devices [18]. Additionally, the scientific community has started to use complex microscale architectures as experimental setups in microfluidics [19] and biology. To fully harvest the potential of such architected structures, it is important to widen the library of materials that can be used and the size scale, while retaining complete control over the microstructure of the materials. In this manner, materials can be engineered for an intended purpose with full control over the material composition, microstructure, and geometry.

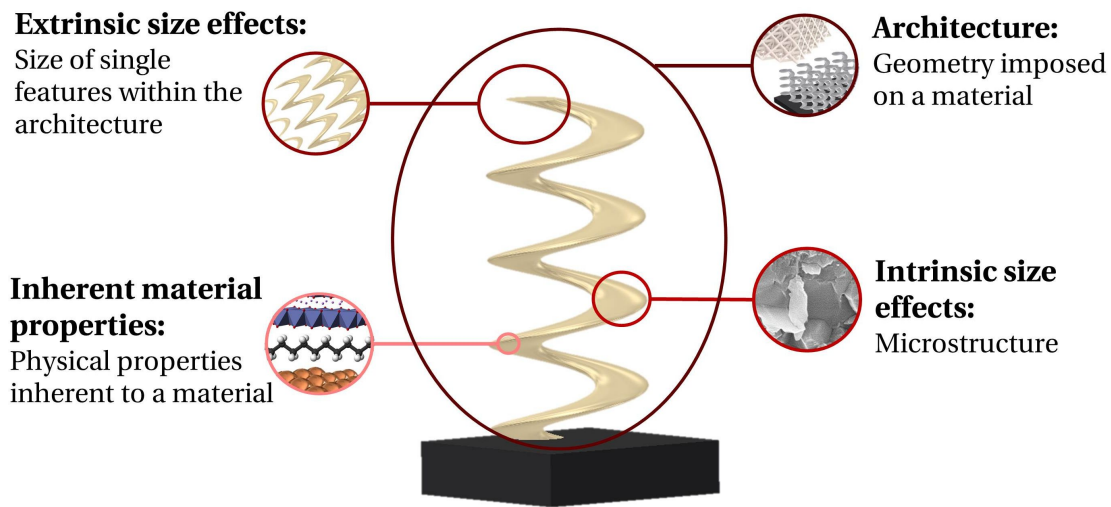


Figure 1.1 – A schematic of the contribution to the material properties of architected materials

1.1.1 Applications of architected materials

Mechanics

In mechanics, AMs have drawn attention due to their highly exciting and tunable properties. Negative and near-zero Poisson ratio materials are known as auxetic and anepirretic materials, respectively [3, 4, 20]. These materials exhibit compression upon loading, a highly interesting phenomenon leading to increased shock absorbance, indentation resistance, and shear resistance. Due to these properties, these materials are often used in protective gear but also proposed for medical devices such as stents, or other applications such as gaskets and air filters. While α -cristobalite Si is a natural occurring auxetic material, [21] most other reported auxetic materials get the auxetic property from the geometrical design.

Another focus of mechanical AMs, the possibility of lightweight and ultra/strong materials. Taking a look at the Ashby plot comparing strength versus density reffig: Ashby Plot, most materials follow the trend of strength through additional weight. Materials with high strength but lightweight aim to fill the voids in the diagram by maintaining the strength of the bulk materials and reducing the density significantly. Ashby introduced a set of rules on the load-bearing deformation depending on the architecture, determining which architecture would be ideally suited to carry a large load, depending on Maxwell's stability criterion. In general, in an open-cell foam structure, the compressive modulus scales with the density of the structure to the power of 3, due to the inefficiency of the system. In more aptly designed structures, see figure 3.1, the compressive modulus scales to the relative density squared. These materials are of special interest in high strength/low weight applications. Well-designed and connected

structures with more conjoined struts, the compressive modulus scales linear to density. As composite materials, such as nanoparticle or fiber-reinforced composites offer a high bulk strength, these composite are prime candidates for high strength/ lightweight materials, as the strength can be retained while the weight can be reduced through 3D structuring.

The image shows a standard periodic table of elements. Elements that are electrodeposited are highlighted in red. These include: Al, Si, P, S, Cl, Ar, Ga, Ge, As, Se, Br, Kr, Hf, Ta, W, Re, Os, Ir, Pt, Au, Hg, Tl, Pb, Bi, Po, At, Rn, and the lanthanide and actinide series (La, Ce, Pr, Nd, Pm, Sm, Eu, Gd, Tb, Dy, Ho, Er, Tm, Yb, Lu, Ac, Th, Pa, U, Np, Pu, Am, Cm, Bk, Cf, Es, Fm, Md, No, Lr).

Figure 1.2 – Periodic Table of Elements with elements that have been electrodeposited indicated

While both of auxetic and high strength/ lightweight phenomenon can be observed at the macroscale, microscale mechanical metamaterials have drawn significant interest as well. In the microscale, the mechanical properties of structures start to change. So-called intrinsic and extrinsic size effects, which are especially pronounced in metallic materials, have been shown in lattice structures for coated metallic or semiconductor microlattices as well.

For intrinsic size effects, the discussion here will be limited to the Hall-Petch strengthening. As shown in figure 1.2, the strength of a metal increases with smaller grains up to a certain point. This strengthening, first described by Hall and Petch is theorized to occur because the grain boundaries hinder dislocation motion through the metal and the smaller grains lead to smaller dislocation pile-ups.[111] These smaller pile-ups are the reason why more force is necessary to reach the amount of dislocations necessary to cause plastic deformation. Reducing the size of the grains further leads to an inverse Hall-Petch strengthening weakening or at least stop the increase in strength. This inverse behavior has been attributed to grain boundary slipping and grain boundary dislocation emission.

Extrinsic size effects can be introduced depending on the microstructure, while for single-crystalline materials, the smaller size scale of a pillar leads to higher strength due to the smaller amount of dislocations nucleation sites and faults. In nanocrystalline material, on the other hand, the extrinsic size effect has been proven to manifest oppositely, leading to a weakening of the specimen by reducing the size. In amorphous structures, the deformation occurs in so-called shear transformation zones. Smaller dimensions can hinder the formation of and

alignment of such zones leading to a change in deformation mechanisms from brittle to ductile. This has been reported by Greer et al for glass.[22] These size effects and the combination of those two, which is not always completely understood, highlight that materials engineering needs to take the microstructure and the grain size into account.

Microrobotics

Another, often discussed, application of 3D metallic materials are micro-robotic structures. Controllable motion is one of the primary goals of microrobots research. In aqueous media, the robots can be propelled either by magnetic fields or chemical reactions. Helix shape, mimicking the flagella of bacteria, are predominant through micro-robotics history, due to their shape-dependent movement, where the rotary magnetic field aligns the helix and the chiral motion propels the specimen forwards. With a magnetic field also oscillating fields and field gradients can be used to move a microrobot [23, 24] Chemically propelled microrobots usually are propelled onward by having a segmented body with an active and a non-active surface. Examples are microcones plated with Pt inside, which facilitates the decomposition of Hydrogen peroxide, forming gaseous in so-called bubble propulsion. Microrobots with targeted, controlled motion are often described as potential drug delivery systems. Therefore, biocompatibility is often a crucial part of these microrobots [25] In an ambient atmosphere, these microrobots are often referred to as walkers, that can be moved at will over a surface with a magnetic field. In both, aqueous and ambient environment the geometry is crucial and therefore also the mechanical stability of such robots is of interest.

Photonics

Photonics is an extended metamaterial research area. The first AMs with exotic optic properties were described by Veselago [26, 27] and subsequently produced in 1997 by Smith [28] These so-called split-ring resonators (SRR) have been the center of numerous applications for sensors, polarizers, and reflectors [29, 30, 31] These split ring resonators can be arranged in large arrays making up a 3D structure. The first 3D metamaterial produced with template-assisted electrodeposition was a helix array produced by Gansel et al from gold, which is described as a deformed SRR [32] These helix arrays function as polarizers for light. To do so, the helical shape needs to have a similar size as the light that is to be influenced. Other people focused on optical band gaps and created photonic crystals [33], where the repetitive structure produces an optical bandgap at the wavelength of the structural repetition. Other, often mentioned structures are inverse opals as can be seen in figure 1.4 or woodpile structures [34]

1.2 Manufacturing

Both subtractive and additive manufacturing methods have been used to create metamaterials. However, over the past decades, responsible handling of finite resources and more elaborate

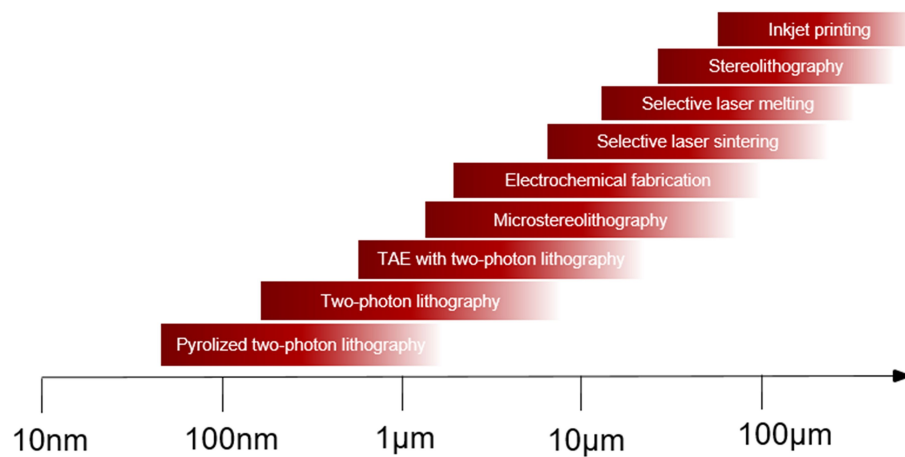


Figure 1.3 – Lowest average resolution (voxel or pixel dimensions) of different additive manufacturing techniques.

demands on 3D structuring, lead renewed efforts in additive manufacturing. Furthermore, a multitude of effects can only be reached in the micro- to nanoscale and therefore micromanufacturing is needed which can be difficult to achieve in subtractive manufacturing. However, the size scale of the chosen additive manufacturing method is crucial to create a metamaterial with the desired properties. While negative Poisson ratio, zero thermal expansion, mechanical nonlinearity, and programmable mechanical metamaterials are size-independent, other metamaterial applications depending on an artificial bandgap in optics and acoustics, the resonance frequency of split-ring resonators are size-dependent and therefore require manufacturing in the microscale. Furthermore, the use of said metamaterials in MEMS-devices and micro-robotics also require microscale manufacturing.

The resolution of different additive manufacturing methods are compared in figure 1.3. While all of the listed manufacturing methods can be used to MMs, each has a specific resolution and, therefore, a specific size range in which the structures can be produced. In 3D printing, the resolution is usually addressed as voxel size. The voxel describes the size of an addressable volume in 3D, analogous to the pixel in 2D. The voxel size is detrimental in which size scale the method is applicable and can produce a structure in a feasible amount of time. A small voxel allows for the creation of smaller more intricate structures whereas a larger voxel enables the creation of macroscale structures in reasonable time scales.

Material dependent aspects of the process must be taken into account as well. All the techniques listed in 1.3 can be used to produce a multitude of polymers, metal, alloys, and semiconductors depending on the metal itself, certain material limitations can occur.

1.2.1 Two-photon Lithography (TPL)

The TPL technique is an advanced type of stereolithography and is built upon the two-photon absorption and emission effect, first described by Nobel prize Laureate Maria Goeppert-Mayer [35]. The absorber molecule absorbs at a higher energy than the laser, so the chemical reaction is initiated only in the focal spot, where the possibility of multi-photon absorption is given. During two-photon absorption, a molecule simultaneously absorbs two photons that induce an electronic transition from the ground state to an excited state inaccessible by single-photon absorption. The two-photon absorption triggers the local chemical reaction in the photoresist. Moving the laser through the photoresist at will allows for freeform 3D shaping. The two-photon absorption retains the reaction localized to the focal point, increasing the resolution and allowing for true 3D printing, while there is still the possibility to write with a layer-by-layer approach.

Two categories of photoresist can be used. Negative-tone photoresists, such as SU-8, IP-photoresists (Nanoscribe GMBH), ORMOCORP and positive-tone photoresists such as the AZ series (Hoechst chemicals). In a negative-tone photoresist, the laser crosslinks the monomer in the resist, subsequent developing is used to remove the non-reacted photoresist. In positive-tone photoresists, the illumination decomposes a photoactive inhibitor compound and the subsequent development can dissolve the photoresist where the inhibitor molecule was decomposed. Other non-commercial photoresists have been reported. An interesting approach is to directly add metal-organic compounds into the resist, which agglomerate and create a metal/carbon framework after pyrolysis, as a way to directly write a composite MM [36]. Ceramic precursors can be used as well that turn into the ceramic after pyrolysis, which has been reported to have a resolution down to sub-100nm features. [37]

Multiple different ways can be used to produce MMs from stereo- and multi-photon lithography. The printed structure made out of photoresist can be functionalized with electroless deposition (ELD) [38], atomic Layer Deposition (ALD) [39, 40], chemical vapor deposition (CVD) [41] or physical vapor deposition (PVD) [42]. Afterward, the polymeric backbone can be removed by pyrolysis, leaving a 3D architected hollow AM. To create non-polymeric, non-hollow metamaterials, one of the most feasible processes that have been used so far in literature is template-assisted electrodeposition (TAE). A template is written in photoresist on a conductive substrate and, subsequently, filled with an electrodeposited material. After the template removal, a dense architecture is left, which then, in turn, can be further functionalized.

1.2.2 Template-assisted electrodeposition (TAE)

Template assisted electrodeposition offers a multitude of benefits. Electrodeposition of metals, films and 2D microcomponents are well-researched and offer a host of elements to deposit and alloys, as can be seen in figure 1.4. For the most part, electrodeposition takes place from aqueous solution, making it a cheap ambient pressure and temperature process. Originally,

the first publication on template-assisted electrodeposition or better known by its German abbreviation LIGA was done in 1982 by Becker to create microscale nozzles. The nozzles were made by plating nickel in a template made by x-ray lithography. Later, electron beam and UV-lithography and were used to create templates. X-ray lithography, electron-beam and UV/EUV Lithography allow the creation of 2D molds with high resolution.

The next step was the introduction of porous membranes as templates to deposit nanowires. Ion-track-etched porous templates [43, 44] as well as anodized alumina templates [45] were used to create nanowires with high aspect ratio. Metallic nanowires were produced from cobalt [46], nickel [46], gold [46], silver [46], copper [46], and alloys with diameters in the lower double-digit nanometer range, as well as semiconductor nanowires from Bismuth telluride [43, 45], ZnO [47] and other various materials. Segmented nanowire deposition was introduced to create even more elaborate nanowires, pulsed electrodeposition [48]

Creating 3D templates has proven more difficult. Layer-by-layer approaches of the aforementioned techniques, greyscale lithography, angled UV-lithography and angled ion track-etched membranes can create certain 3D patterns. However, due to their geometrical limitations, it's widely considered 2.5D. A kind of 3D templates were created by self-assembly of colloidal crystals [49, 50] Self-assembly of colloids creates opal templates which in turn can be used for electrodeposition. These colloidal templates can be made from a host of different spherical materials, such as Polymethylmethacrylate (PMMA), SiO₂ or Polystyrene (PS) [51] However, the colloids offer little geometrical freedom expect to change the size of the spheres and some limited deformation of the spheres by annealing.

True 3D freedom was given by stereo and two-photon lithography. With the photoresist being the same as used in regular UV-Lithography, the first results have been published in 2010 using two-photon lithography in combination with electrodeposition [52] Here, the photoresist can be patterned with almost total geometrical freedom. This method takes the electrodeposition of 3D structures from a set of given geometries to 3D additive manufacturing.

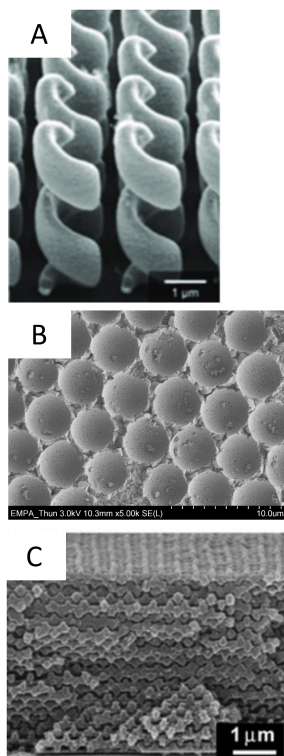
The advantage of template assisted electrodeposition over two-photon lithography plus subsequent coating is the mechanical and chemical stability of the final component. The photoresist core in the coated structures are mechanically weaker than a metal core structure. Thermal expansion and contraction also impact the thermal application range of these structures, as the photoresist yields a higher thermal expansion than the oxide and metal coatings. Degassing of the photoresist in a low-pressure environment also reduces the application range of these polymers. Lastly, the interface between photoresist and coating also introduces challenges in predicting the behavior of such AMs. In conclusion, fully metallic microarchitectures offer large benefits if they can be produced with the same accuracy and reliability as two-photon lithography pul subsequent coatings can reach. While as of yet, there is a limited amount of application. Due to the high produciton cost and limited upscalability, the most likely applications are in high-tech devices. Medical applications such as high precision needles and nozzles as well as microrobotic drug delivery with biocompatible metals are often mentioned.

Furthermore, complex 3D-parts for watches and other mechanical parts with demand for high accuracy are also fields with possible applications for such components. The largest application field of TAE in combination with TPL is in academia. The combination allows to create highly accurate, metallic 3D structures for microfluidic, biological, optical or micromechanical experiments manufactured to the researchers demand.

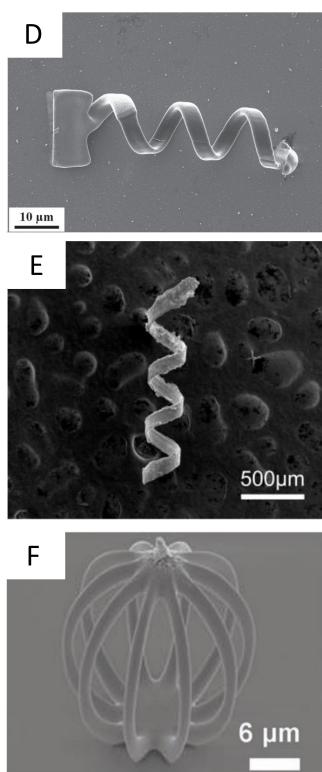
Therefore, this thesis aims to highlight the advantages of the technique and to show the problems and help create solutions to mitigate these drawbacks.

Electrodeposited architected structures

Optical:



Microrobots:



Mechanics:

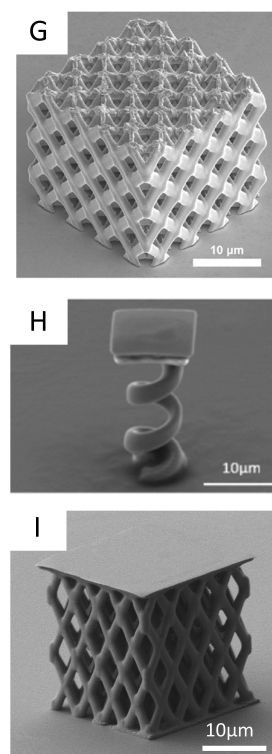


Figure 1.4 – Electrodeposited Structures: A) Gold spirals made by Gansel et al [32]. B) Zinc oxide inverse opal layer done as part of the work carried out during this thesis work. C) Inverse woodpile from CuO₂ by Park et al.[53] D) Nickel/PPy spiral by Zeeshan et al. [25] E) CoNi Spiral by Chatzipirpiridis et al.[54] F) Micro-roller made out of Iron by Alcântara et al.[55] G) Microlattices from quasi-single crystalline Copper by Gu et al.[56] H) Nickel micro-springs produced in this work.[57] I) Nickel microlattices produced in this work. All pictured are reprinted with permission.

1.2.3 Nanocrystalline materials

Nanocrystalline (nc) metals, with a grain size below 100nm[58], exhibit interesting properties, mechanically less ductile, increased hard due to Hall-Petch strengthening, excellent softmagnetic properties, lower thermal conductivity and higher specific heat [59] Due to this set of altered properties, these materials have various applications as hard coatings and magnetic coatings. The fabrication of nanocrystalline 3D components, unlike coatings, is limited to only a few methods. Additive manufacturing methods that include melting or sintering are likely to induce grain growth due to the process heat. Other common techniques for the production of nanocrystalline material include mechanical alloying, CVD and PVD, which lack the technology to accurately create freeform and most importantly, fully dense microscale 3D structures. Electrodeposition, however, can proceed within pre-designed templates, allowing to attain desired shapes, without needing to operate at elevated temperatures. These characteristics make electrodeposition the prime technology for creating nanocrystalline materials requiring specific geometries. Nanocrystalline nickel is especially prominent amongst the electrodeposited materials. High hardness [58], reflective surface [60] and improved corrosion resistance [61] have enabled nanocrystalline nickel to be used as protective coatings. Furthermore, nanocrystalline nickel has shown interesting catalytic properties as a possible other application. Finally, nickel can be deposited as an alloy together with Fe [62], Co [63], Cu [64, 65], C [66] and W[67] providing additional reasons for studying this material. Therefore, nc nickel is excellent material to use in this study of 3D TAE.

2 Statement of the problem

EcAM by TAE has rarely been reported in literature so far (Appendix figure 1). In this work we will use the previously described TPL to create templates for electrodeposition. Current research using TAE with TPL, using complex templates for electrodeposition focuses mainly on accomplishing the desired architecture with little to no regard for the electrodeposition aspects of the method [68, 56]. In this thesis, we carried out a holistic study encompassing all three major areas of TAE: the technical aspects, an in-depth electrochemical discussion, and mechanical testing as an investigational tool in addition to applications for the deposits.

Filling a complex template already poses significant technological challenges from the creation of the templates, wetting and removing the template after the deposition.

From an electrodeposition standpoint, the deposition has to yield the desired microstructure, have minor internal stress to avoid deformation of the free-standing structure and most importantly, the deposition needs to yield a good filling ratio. Whilst the architecture is of utmost importance, scarcely any work has been presented where complex structures have been deposited with the simultaneous study of the influence of the template on the electrodeposition. Bath compositions, pulsed or direct deposition, and the influence of deposition voltages all shape the microstructure of the deposited material. This interplay of electrodeposition parameters, template structure and microstructure has not been described. Therefore, it is of crucial importance to study this interaction. Electrodeposition into 3D templates is confronted by similar challenges as electrodeposition into 2D templates but introduces further aspects to consider. The combined aspects and challenges for electrodeposition into 2D and 3D templates are listed in figure 2.1.

The electrodeposition into the template can be influenced by a multitude of phenomena, as can be seen in the figure 2.1.

- The shape of the template influences the deposition significantly, as the active area can change with time.
- Corners can create trapped electrolyte and therefore stop the deposition locally.

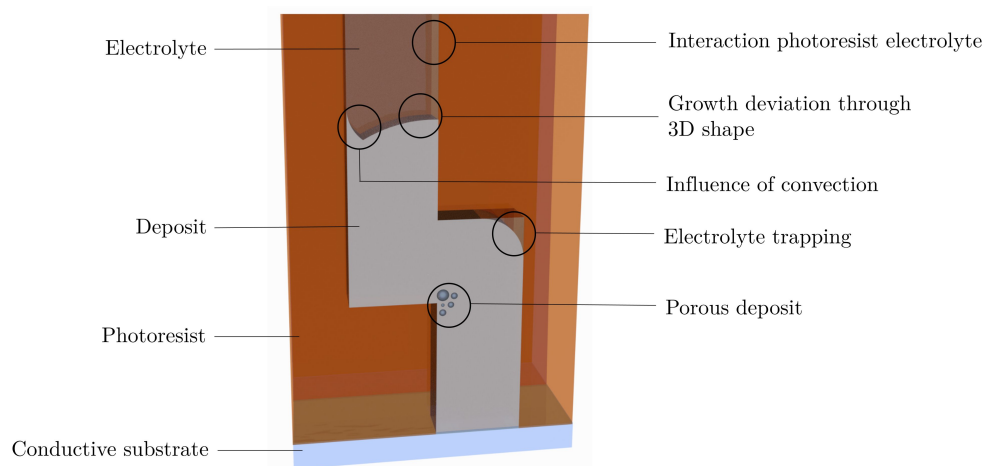


Figure 2.1 – Graphic listing specific challenges of electrodeposition into 3D templates. The schematic shows the conductive working electrode (dark red), the template (light red), the electrolyte (white) and the deposit and growth direction (gold).

- In a 2D template, deposition usually takes place normal to the substrate, even if the substrate has a complex shape. In the 3D template, the deposition is not necessarily normal to the substrate, especially as the deposition directions can change with time.
- Electrodeposition side-products like hydrogen gas can create bubbles in the template which could stop deposition entirely by blocking a pore or inhibit deposition locally on the growth front, creating porous deposits.
- The convection in the template is dependent on the geometry of the template and therefore influences mass transport.

From a mechanical standpoint, the previously mentioned technological as well as electrochemical challenges such as inaccuracy to the design due to poor resolution or low filling ratio as well as microstructure flaws can significantly alter the mechanical properties. Therefore, the mechanical investigation of the structure is not only to investigate the structures with regard to possible applications of TAE in MEMS, but also yields information of the homogeneity of the deposited structures and possible microstructure non-uniformity such as porosity. All aspects combined can yield a more in-depth view of the benefit and drawbacks of template-assisted electrodeposition.

In order to achieve this, goal the work was conducted in multiple parts as seen in figure 2.2.

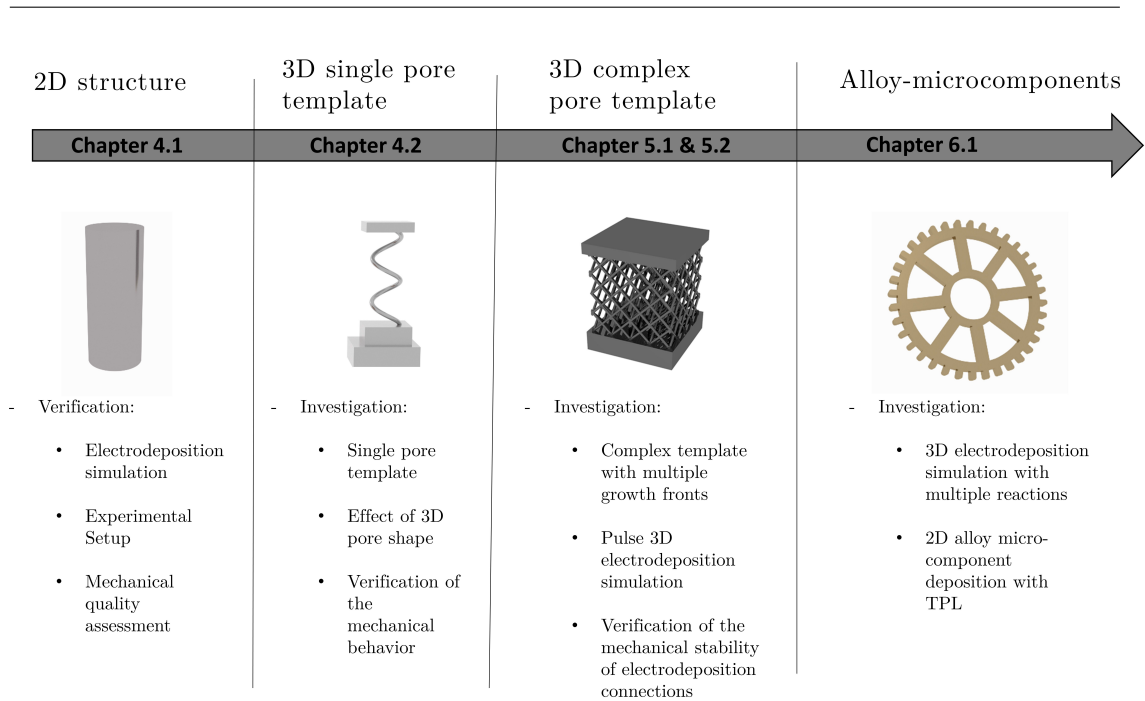


Figure 2.2 – A schematic showing the chapters of this thesis and the reasons for investigating these various structures.

3 Methods and techniques

In this section, an overview of the methods and techniques is given including background information. Template-assisted electrodeposition is a combination of lithography, electrodeposition, and in the case of this work mechanical testing. Due to the limitation of observing the electrodeposition in-situ, electrodeposition simulations provide information on the exact nature of the filling process in template-assisted electrodeposition. Therefore, the following chapter entails a basic discussion of electrodeposition, a mathematical description of electrodeposition, a description of two-photon lithography, and a short description of the mechanical testing.

3.1 Electrodeposition

Electrodeposition is a technique mainly used to coat thin metal films on conductive substrates. The setup for electrodeposition usually contains three electrodes: a working, a counter, and a reference electrode. In this setup, the current flows between the counter and working electrode while the potential is measured between the working and reference electrode. The electrolyte contains ions of the material to be deposited. At equilibrium, the system is at the open circuit potential. By applying a potential or a current, the system can be forced away from the equilibria, to deposit the metal. The potential of the working electrode changes the Fermi level of the electrons in the electrode, therefore the electrons react with the absorbed ions to reduce or to oxidize an absorbing species. In the case of metal electrodeposition, usually, the metal atoms are present in aqueous solution as cations and are reduced at the working electrode.



The metal can be deposited from the solution, once the potential is shifted enough to transfer electrons from the electrode to the cation absorbed on the surface. The deposition starts

initially with the formation of nuclei on the substrate and enters a steady growth state eventually. During the deposition an electrochemical double layer forms. As can be seen in figure 3.1, there is no current flowing at equilibrium and once a deposition potential is applied the current drops during nucleation and enters a quasi-steady state during deposition.

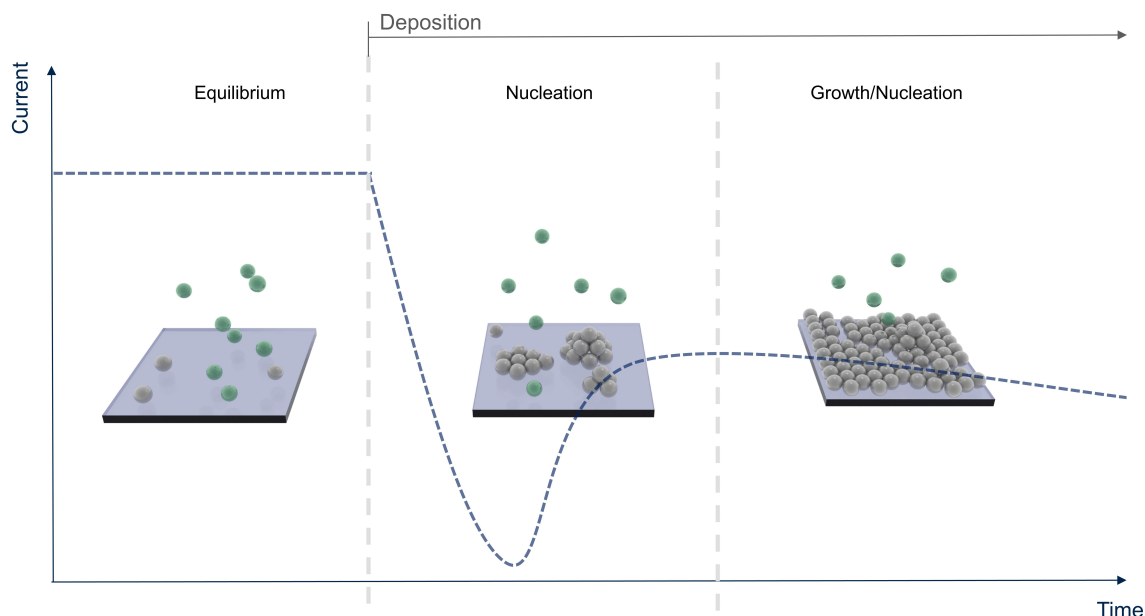


Figure 3.1 – A schematic of the electrodeposition process with time, starting at equilibrium at the left, a nucleation phase, and a steady growth/nucleation at the right

The double-layer at the electrode consists of the inner Helmholtz plane at the electrode, the outer Helmholtz plane follows after consisting of cations to compensate the charge of the electrode. This is followed by a diffusion layer and the bulk electrolyte. This model of the double layer is called the Gouy-Chapman-Stern model and delivers a sufficiently accurate description of the electrode/electrolyte interface in electrodeposition. The model consists out of an inner Helmholtz plane (IHP), an outer Helmholtz plane (OHP) a diffusion layer and the bulk electrolyte. As can be seen here, the potential in the electrochemical cell drops sharply from the applied potential to equilibrium close to the electrode.

The ion flux in the electrolyte is subject to three different forms of movement. The convection of the electrolyte, the migration in the electric field and the diffusion. A mathematical description of this behavior can be found in equation 3.7. A closer look at the potential distribution in the cell shows that the potential deviation from the equilibrium is localized close to the electrodes in the double layer, while the largest part of electrolyte remains at or close to equilibrium.

The current distribution in an electrochemical experiment can be described as a combination of three different current distributions: Primary, secondary and tertiary. The primary current distribution is given by the ohmic resistance in the bath due to electrode resistance and electrolyte conductivity. Secondary current distribution takes into account the kinet-

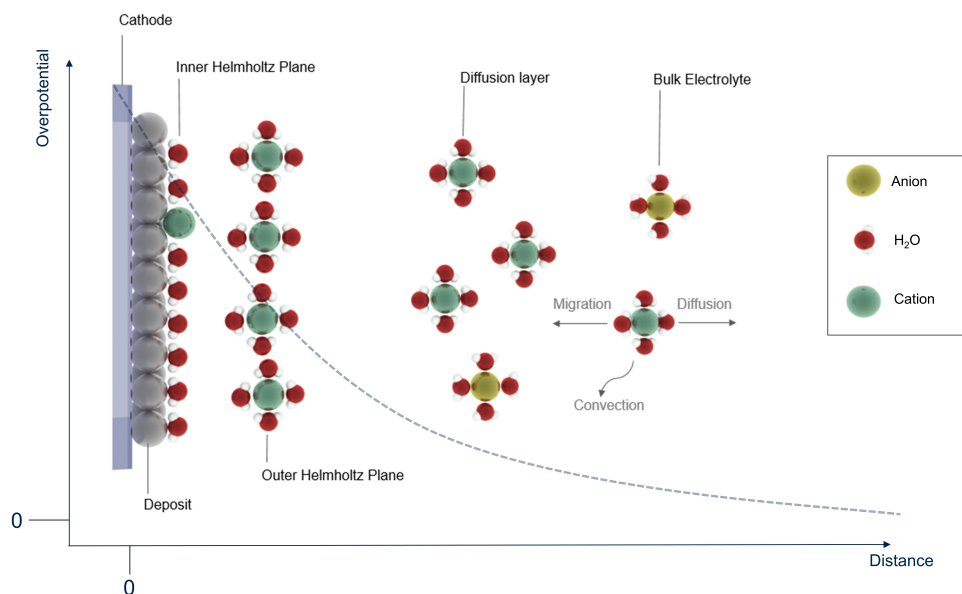


Figure 3.2 – A visualization of the double layer at a cathode in the electrochemical cell, depicting the deposit, the IHP, OHP, diffusion layer and the bulk electrolyte. The arrows are not indicative of the movement and merely represent the different contributions to the movement of the ions.

ics of the reactions taking at the electrodes. The tertiary current distribution describes the concentration-dependent contribution to the total current.

Influence of electrolyte constituents

The electrolyte composition is crucial to the electrodeposition. The electrolyte media determines the potential window that can be applied within which the media itself is not deteriorated. For aqueous media, this potential window, about 1.23V, determines which metals can be deposited, i.e. Ni, Fe, Cu amongst others. Elements such as Al, Ti, and Si can not be deposited from aqueous solutions, as the potential needed to be applied lays significantly outside of stability window of aqueous solutions. The stability window of water can be improved and shifted with additives to a limited extent. The aqueous media can be changed to ionic liquids to deposit materials that otherwise would not be possible. They are not as frequently used however, due to their higher cost, reduced conductivity, and difficult handling.

The overall amount of ions in the electrolyte determines the conductivity of the electrolyte, so supporting electrolytes can be added to increase the conductivity. Ideally, a supporting electrolyte increases the number of charge carriers within the electrolyte without interfering in the deposition itself. Therefore, supporting electrolytes are often acids or bases that add H^+ or OH^- and a cation or anion that is already in the electrolyte from the salt compound used for

Chapter 3. Methods and techniques

the active species, such as K^+ and Na^+ or SO_4^- or Cl^- . Limited conductivity leads to a primary contribution distribution regime.

Both the conductivity and the amount of active species are detrimental to the so-called throwing power of an electrolyte. The throwing power is a way to describe the ability of an electrodeposition system to create uniform thin films on uneven substrates. This property of an electrodeposition system is often indicated by the Wagner number.[126]

$$W_a = \frac{k}{L} \left(\frac{\partial \eta_{app}}{\partial i} \right) \quad (3.2)$$

The dimensionless Wagner number was introduced to describe the ability of homogenous electrodeposition on large 3D parts. K describes the electrolyte conductivity, L is the characteristic length scale, in most cases the electrode size and η_{app} is the applied overpotential. The higher the Wagner number the lower is the geometrical influence of the surface morphology. The Wagner number compares the resistance associated to the surface reaction to the ohmic resistance of the electrolyte. The drawback of this approach is that it is not ideal as at the small scale the ohmic resistance tends to be extremely small. To describe the leveling power at the microscale, Landau[123] introduce a leveling parameter, akin to the Wagner number:

$$P_l = \frac{ni(1 - \frac{i}{i_{lim}})}{ai} \quad (3.3)$$

Here, the leveling parameter P_l is given as a function the charge number of transferred electrons n , the current i , the limiting current i_{lim} , and a , the charge transfer coefficient. The leveling parameter compares the resistance of the surface reaction to the mass transport resistance, instead of the ohmic resistance. For both parameters, a higher value indicates a more kinetically dominated deposition taking place whereas a lower number indicates mass transport or ohmic resistance limited deposition.

Therefore, the electrodeposition of homogenous films is often achieved with a large number of active ions, to have a low ohmic resistance and high limiting current, therefore a dominant secondary current distribution. The active species is the species of ions that is to be deposited. The amount of active species determines the deposition speed as well as in which regime the electrodeposition takes place. The higher the amount of active species the more likely it is that the reaction is mainly kinetically limited. If the concentration of active species is low, the more likely it is to reach a pure mass transfer regime. Kinetically limited systems are preferable for industrial plating as the mass transfer and convection around a part to the plate can be neglected. For 3D-structuring, a high leveling power is favorable as well.

Furthermore, having a high concentration of active species in cathodic deposition leads to a high number of cations close to the electrode surface shielding the electric field partially and therefore reducing migration. Additionally, a high active species concentration also reduces the size of the depletion zone close to the electrode, which minimizes the cations movement as well by reducing the diffusive pressure towards the electrode. Therefore it can be said that higher ionic strength is leading to less pronounced flux in the template. This can be seen in figure 3.3. This simulation, built upon the simulation later introduced in chapter 4.2 and 5.1, is to help explain the choice of high concentration electrolyte. The simulations where a flux is introduced from left to right via influx on the left and outgoing flux on the right shows overall higher flux than compared to a simulation where no guided flux is introduced. This is especially pronounced when combined with the lower ionic strength of the electrolyte.

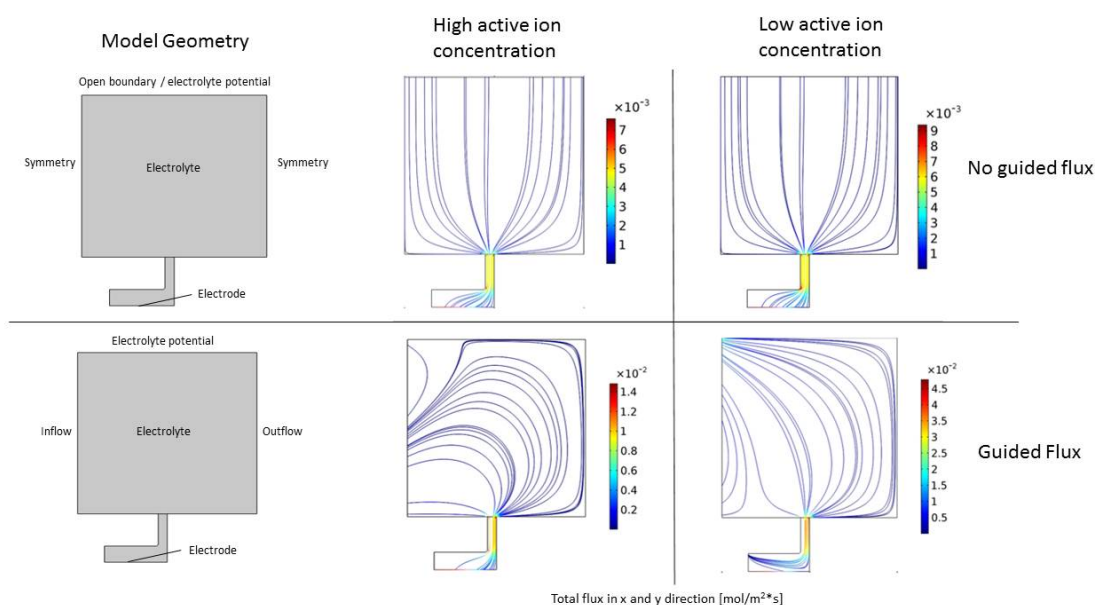


Figure 3.3 – Simulation based on the work in chapter 4.2[57] of guided and non-guided flux with high and low concentration. High ion concentration: 1.5mol/l, Low concentration: 0.05mol/l

The additives can influence the leveling significantly, an explanation of the influence of the additives can be found in 'section 3.1.1' *Nickel electrodeposition*. Additives can be added to influence the deposits microstructure and to shift the deposition potential of the species. The deposition potential is usually moved further from deposition potential as the additive molecules adsorb on the electrode surface and therefore hinder the deposition. The additives in this work, with the exception of the sodium citrate in chapter 6, are used to influence deposit grain size and not to shift the deposition.

Influence of the electrodeposition parameters

Electrodeposition can be carried out in potentiostatic and galvanostatic mode. In galvanostatic mode, a current is applied between the working and counter electrode. This is the predominant model used in industry, due to the possibility of using a two-electrode setup without a reference electrode. In potentiostatic mode, a potential is applied to the working electrode. During thin film deposition and 2D template filling, galvanostatic mode is often used. In 3D templates, the surface area of the growth front can change significantly with time. Therefore, if a current is applied, the deposition potential changes significantly once the active plating area changes, which also may change the microstructure of the deposit. Whereas, if an applied potential is applied, the total amount of current changes but the deposition potential stays the same.

Pulsed electrodeposition can be used. Introducing pulsed electrodeposition with an off-time allows the system after each deposition pulse to regenerate and replenish the ion concentration close to the electrode.[119] Microstructural changes can occur due to the pulsing as well as a reduction of internal stress can be achieved this way. The latter point can be important for 3D template filling to avoid deformation of the deposited part.

Reversed pulse deposition can be used to directly interfere with the morphology of the deposit. A reversed pulse can be introduced to strip the most protruding features on the deposit. The reverse pulse significantly slows down the deposition rate, as it is not only an off-time but actively strips parts of the deposit during the reverse pulse. Especially for low throwing and low leveling power electrolyte, this can be a helpful tool to increase homogeneity in the deposit. Furthermore it can be used as a means to help fill difficult templates such as 90° corners as can be seen in chapter *Complex Templates*.

Influence of environmental parameters

Convection is often used in electrochemical systems. The reason to use convection is to homogenize the electrolyte. In electrolytes with low concentration of active species, convection is used to increase mass transfer to the electrode, so that diffusion and migration are not solely making up the entire mass transport. To describe the convection in the electrochemical system, the Schmidt [69] and Reynolds [70] number are often used. Both are dimensionless descriptive numbers. The Reynolds number, Re describes the flow of a fluid.

$$Re = \frac{uL}{\nu} \quad (3.4)$$

u is the imposed flux, L is the characteristic length and ν is viscosity. L is usually describing the inner diameter of a tube in the simplest case. In 3D templates, it would be equivalent to an average diameter. A low Reynolds number generally indicates laminar flow and high Reynolds

number suggests turbulent flow. This can be used as an indicator of which flow is present in the template. It should be mentioned that the Reynolds number does not factor in surface roughness for instance which can be significant in templates as small as the ones used in this work. The Schmidt number, Sc , on the other hand, can be used to establish a ratio between the kinetic viscosity and mass diffusion. The Schmidt number for mass transfer is akin to the Prandtl-Number for heat diffusion in fluids.

$$Sc = \frac{\nu}{\rho D} \quad (3.5)$$

ν is the kinetical viscosity of the fluidity and ρ the density and D the mass diffusivity. The Schmidt number can be used to estimate the thickness of the boundary layer in a fluid system. The boundary layer is a term used to explain the presence of a layer of molecules or atoms that are not freely floating within a liquid but attached or influenced by the presence of a wall. In general, these numbers can be useful as indicators. However, considering template filling, convection within a template is complex, as it is dependent on the geometry of the template. Therefore convection is not considered in the latter described simulations.

While pressure is usually a neglectable property, the temperature is an important factor in electrodeposition. In the most common case, aqueous medium, the useful range is between 0-100°C. There is also a necessity to ensure the stability of the chemical compounds in the electrolyte. The temperature influences the mobility of the ions, see equation 3.8, and more importantly, the kinetics of the reactions see equation 3.14. Furthermore, the temperature also changes the density which in turn changes the viscosity terms used in equations, 3.5 and 3.4.

3.1.1 Nickel electrodeposition

Nickel is among the most prominent materials to be electrodeposited. Nickel is used widely as a hard coating to improve the hardness and wear resistance of metal parts [58] Furthermore, it can be alloyed with various elements such as Iron,[71] cobalt[63], and copper[72, 64]. Nickel can be electrodeposited from different electrolytes. The Watt's bath is the most prominent solution containing nickel sulfate as the major constituent [73] nickel sulfates the main source of nickel, nickel chloride to facilitate nickel corrosion [61], for the use of a soluble counter electrode and boric acid to reduce hydrogen evolution[74] In this work, the nickel electrolytes used were nickel sulfamate electrolytes. Nickel sulfamate is the main constituent and nickel chloride is added for the same reason as in the Watt's bath. Nickel deposits from sulfamate baths exhibit lower internal stress, [75] a fact crucial to electrodeposition of 3D-structures. Additives are usually added to control the grain size. Sulfur and phosphorous containing additives are especially well suited to induce smaller grains in the deposit. In this cases, sulfur and phosphorous are introduced as impurities in the deposit. Due to the high grain boundary

segregation that these impurities exhibit in nickel, the grain boundary is pinned and the growth of new grains is highly favored.[76] Surfactants or wetting agents are important to decrease the surface tension of the and improve the wetting of the templates.

Hydrogen evolution reaction (HER)

HER is one of the most crucial aspects to be taken into account.[75] Hydrogen evolution is present at the cathode if the deposition potential is sufficiently negative. Hydrogen evolution not only diminishes the faradaic efficiency of the electrodeposition process, which is a significant parameter for industrial applications, it usually also increases the internal stress in the deposit. Various methods can be implemented to reduce the amount of HER in the process. The pH can be increased to reduce the number of protons able to take part in the reaction. The deposition potential can be shifted closer to the equilibrium. Another often applied method is adding constituents to the electrolyte that either, widen the electrochemical stability window of water or that block the most protruding parts of the surface, favoring homogenous growth, reducing the possibility of high local overpotentials.[75]

pH-Buffers decrease the gradient of protons at the cathode surface, there the local pH at the electrode decreases, reducing the amount of HER. Levelers reduce the surface roughness of a deposit by reducing the grain size, thereby also reducing the risk of very high local current densities, which in turn, can reduce the amount of HER.[75] Surfactants decrease the size of hydrogen bubbles, allowing for swift removal of the produced hydrogen from the electrode, reducing the amount of pitting. Furthermore, they facilitate electrolyte infiltration into a patterned substrate and are therefore crucial to template-assisted electrodeposition.

3.2 Electrodeposition simulation

Herein, the phenomenological description of the previous section is addressed in numerical terms with the equations used to model the electrodeposition process. The equations can be found in the COMSOL electrodeposition manual. At open circuit potential (OCP) the system is an electrochemical equilibria. The potential at the electrode outside of the equilibrium, overpotential η , can be calculated as follows:

$$\eta = \eta_{eq} + \eta_{app} \quad (3.6)$$

with η_{eq} as the equilibrium potential and η_{app} the applied potential. Once a potential is applied, the flux of the metal ions N_M the movement of the ions, depicted in figure 3.2, can be

described by the Nernst-Planck equation.

$$N_M = -D_M \nabla c_M - z_M u_M F c_M \nabla \phi_1 + c_M u \quad (3.7)$$

wherein D_M is the diffusion coefficient, z_M is the charge, u_M is the mobility and c_M as the concentration of metal ions M . F denotes the Faraday constant and ϕ_1 the electrolyte potential and u as the convection factor. The mobility of the ions, u_M , can be derived by the Nernst-Einstein relation

$$u_m = \frac{D_M}{RT} \quad (3.8)$$

Once the flux of the ions is addressed, all the mass in the system can be accounted for by a mass balance equation:

$$R_{M,tot} = \frac{\partial c_M}{t} + \nabla N_M \quad (3.9)$$

with $R_{M,tot}$ as the total amount of Metal atoms, c_M as the metal concentration, t the time and N_M as the flux of Ni introduced or removed of the system by deposition, dissolution or electrolyte flux.

As the system enters a steady deposition regime, the local current density vector i_l , can be calculate,

$$\nabla i_l = \sigma_1 \nabla \phi_1 \quad (3.10)$$

by multiplying the electrolyte conductivity σ_1 by the electrolyte potential. This is a simplification as the electrolytes used in this thesis are including supporting electrolytes, see section *Nickel electrodeposition*, so the majority of charge carriers are not involved in the electrochemical reaction and therefore stable. If this is not the case, a more accurate description can be seen in equation 3.11.

$$\nabla i_l = -F \Sigma (-D_M \nabla c_M - z_M u_M F c_i \nabla \phi_1) + Q_l \quad (3.11)$$

Chapter 3. Methods and techniques

with the local current density vector, i_l as the sum of the charged particle flux multiplied by the Faraday constant and a contribution of a current source or sink Q_l .

The movement of the ions is accounted for and the electrolyte potential conductivity and local current density vectors defined, the local current i_{loc} on the electrode can be described by the cathodic and anodic Tafel law,

$$i_{loc} = i_0 * 10^{\frac{\eta}{\alpha_a}} \quad (3.12)$$

$$i_{loc} = i_0 * 10^{\frac{\eta}{\alpha_c}} \quad (3.13)$$

as a function of the anodic and cathodic reaction and the exchange current density, i_0 . The exchange current density is the amount of current generated at equilibrium, see figure 3.1. Because the total amount of current is zero, it can not be measured but is usually determined by Tafel analysis. The anodic and cathodic charge transfer coefficient, α_a and α_c , describing the kinetics of the respective reactions. This can be used if only one electrode and its reactions is of interest and for low overpotentials. Otherwise, the Butler-Volmer equation, 3.14 is a more accurate description:

$$i_{loc} = i_0 \left(\exp\left(\frac{\alpha_a F \eta}{RT}\right) - \exp\left(-\frac{\alpha_c F \eta}{RT}\right) \right) \quad (3.14)$$

With a local current and reaction rate established, the growth rate of the electrode, v , can be derived by

$$v = \sum_M \frac{R_m M_M}{\rho_M} \quad (3.15)$$

calculating the volume change of the electrode as a summation of the reaction rate, R_m , multiplied by the mass of the metal, M_M divided by the density of the deposited material, ρ_M .

3.2.1 Finite element - simulation

With a mathematical description of the electrodeposition, it is possible to implement a finite element simulation. Electrodeposition simulation was used frequently to help estimate the growth in a template, determine the importance of spacing and arrangement of features on a

sample, and quantifying the influence of electrodeposition parameters on template filling. All this work was carried out for mesoscale and microscale 2D microcomponents.[99, 120, 92, 93, 94]

To implement the above-mentioned equations, we used COMSOL 5.1 with the COMSOL electrodeposition module to create time-dependent finite element simulations. Finite element simulation allows us to create numerical approximations to partial differential equations by using a finite amount of elements and appropriate boundary conditions. The geometry is divided into these elements which are ideally geometrically simple. In this work, 2D simulations were carried out with a triangular meshing and 3D simulations with tetrahedral meshing. This way, the single elements are assembled into a global matrix which in turn builds up the global equation system.

Creating a correct mesh of geometry is crucial. The geometry must be meshed small enough to be accurate and large enough to ensure it is still calculable within an appropriate time. The global matrix, A_x , consists out of $N_x * N_x$ values are given by the number of elements, N , and the number of variables to solve, x . Therefore, the number of elements as well as the number of variables to solve increase the calculation effort significantly. Each element, therefore, has an index, A_x , for instance, has global nodes connecting with other elements and local nodes that describe each corner of the element. Through the principle of superposition, each elements local node corresponds to a global node which in turn corresponds to the neighboring elements local nodes.

After the mesh and global matrix is assembled and the boundary conditions set, a solution can be calculated. In this work, the Comsol variation of a newton solver was used, where an approximation of the nonlinear equations is made an iterated until the residual is small or the successive solution between iteration is below a preset threshold. In this work, time-dependent simulations with initialization were made. Time-dependent solutions are crucial for template-assisted electrodeposition. As with ongoing-time the geometry of the electrode changes. The time-dependent calculation, in this case, starts by a calculation of the initial state via the Galerkin method[77] and from there derives the change in the system with time.

Due to the deposition with time, the mesh gets deformed over time. It is, therefore, crucial to monitor the quality of the mesh. The mesh quality can be described in various ways, such as skewness, maximum angles, as a ratio of volume versus circumferences and others. Once an insufficient mesh quality occurs, the simulation has to be remeshed. Due to the nature of electrodeposition, very small features in the templates can be left unfilled, which the simulation can not remesh if the mesh size is set larger than the dimension of those unfilled features. Therefore, the simulation may have to be stopped, the geometry repaired and remeshed. This tedious part of the work is the most technologically limiting factor in electrodeposition simulation of complex structures.

More exact details on the finite element simulations and meshing can be found in the extensive COMSOL simulation documentation or in the book *"Modeling and Dimensioning of Structures"*:

A Practical Approach" by Gay and Gambelin.[77, 78]

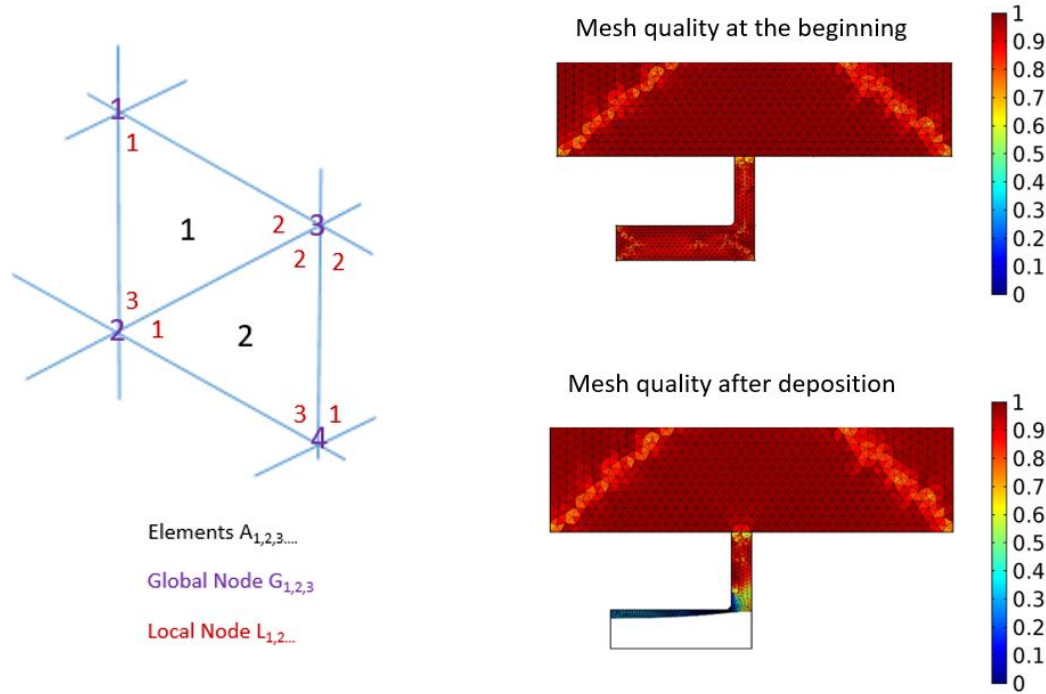


Figure 3.4 – Finite element visualization and mesh quality before and after deposition.

Evaluation of the simulation

As mentioned above, an appropriate meshing is crucial to successful finite element simulation. As a means to ensure the meshing is not influencing the result of the simulation, mesh convergence studies were carried out at the beginning of each simulation. An upper and a lower threshold for mesh size were defined in the COMSOL software, depending on the geometry at hand. As a rule, the upper threshold for the mesh size was set to yield a reasonable amount of elements within the smallest feature of the design. The lower threshold was set roughly one to two orders of magnitude smaller, e.g. an upper threshold of $5\ \mu\text{m}$ and a lower threshold $500\ \text{nm}$. From there, the simulation was initialized and let run for the first couple of seconds with smaller mesh sizes. The initial values for the current density were compared and deemed sufficient when the values stabilized despite the change in mesh size. At this point, the influence of the mesh is smaller than the values set for absolute and relative tolerance of the COMSOL solver. The absolute and relative tolerance were set at 0.05 and 0.005 initially and reduced if possible where the simulation was able to yield a result at 25 iterations per step. The benefit of this procedure is that the meshing does not influence the initial result of the simulation. The drawback of the time-dependent mesh change is that the deformation with ongoing time, depending on the shape of the pores, creates meshes of different quality. Therefore, the more complex the deformation of the mesh and the worse the quality, the

larger the possible error due to the meshing. It is therefore important to keep in mind that comparisons between structures have to be made with certain care and limited to compare similar structures.

3.3 Lithography and templates

Two-photon lithography is a 3D-photopolymerization technique, illuminating the pattern at twice the wavelength of the photoresist absorption. Due to the effect described by Nobel prize laureate Maria Goeppert [35], two photons can be absorbed simultaneously if the intensity is high enough and initiates the reaction in the photoresist. Deriving an equation equivalent to Lambert-Beers single photon absorption law, the following equation can be created to yield $\frac{\partial I}{\partial Z}$, the adsorption density in a sample with thickness Z .

$$\frac{\partial I}{\partial Z} = BI^2 \quad (3.16)$$

With B being the two-photon absorption coefficient, I the Intensity. Due to the scaling of the intensity, two-photon adsorption is spatially confined to the focal point of the laser while the rest of the photoresist does not interact with the laser beam. This effect enables 3D microfabrication by guiding the laser through the photoresist. The voxel is given by the size of the focal point and photon flux therein.

TPL is therefore used for microfabrication. Due to chemical interaction combined with the two-photon absorption, a resolution below 200 nm has been reported in XY-directions. Due to the elongated shape of the focal point, the resolution in the Z-direction is lower and usually omitted. Whereas for two-photon optical microscopy, the Abbe limit has been overcome in a significant manner, the diffraction limit in two-photon lithography has only been beaten by a few nanometers.[79]

With the resolution well in the sub-micron scale, Greer et al [36, 80] and Wegener et al [81, 9, 2, 82] amongst others have shown to be able to create micro- and mesoscale structures with almost complete freedom.

Photoresist

The choice of photoresist is crucial. The photoresist can be split into two different kinds, positive tone photoresist and negative tone photoresist. In the former, the development removes the illuminated photoresist, cross-linking the non-illuminated parts and in the latter, the illumination crosslinks the photoresist, so the development removes the non-illuminated parts. In this thesis, negative tone photoresist used are commercial products from Nanoscribe GmbH called IP-S and IP-Dip and the positive tone photoresist is AZ9260, from Hoechst Chemicals, that will no longer be manufactured as of the writing of this thesis. However,

Chapter 3. Methods and techniques

similar resist can be purchased from the AZ-photoresist series. Both types of photoresists have their advantages and drawbacks.

The negative-tone photoresist is used in multitudes of studies and also the previously mentioned submicron resolution was reported with negative type photoresist. Negative type photoresist crosslinks into PMMA, epoxy-based or acrylate-based polymers, which are very chemically resistant.[83] The procedure to remove these photoresists can be found in chapter 5.1 as a mixture of O₂ and CF₄ plasma. The etch rate is heavily dependent on the volume of the chamber, the power of the plasma and the amount and ratio of the gases introduced. The chemical stability of photoresist against common organic solvents makes it a good choice for templates for electrodeposition from ionic liquids as well as in low pH and high pH environments. Due to the aggressive removal process, this photoresist is not ideal for the creation of structures made from easily oxidized material.

Positive-tone photoresist needs to be spin-coated for a dense layer to manifest, which is subsequently patterned. The positive photoresist is usually used in some form of lift-off process or as a template for electrodeposition.[84, 57] Due to its nature to remove the illuminated parts, the photoresist is ideally suited for templating, as it increases the writing speed and removes the time-extensive design of a template. It is less chemical resistant than the aforementioned negative type photoresists which is ideal for subsequent removal after the deposition step. The soft nature of positive-tone photoresist also offers the possibility of a soft bake in order to have the photoresist reflowing, rounding out the contours. However, due to the fragile nature, it is not suited for certain electrolytes and environments. The developers for positive-tone photoresist of AZ 9200 series are alkaline substances, removing the photoresist. Therefore, electrolyte with a high pH can not be used as the electrolyte eventually strips the photoresist. At lower pH, significant concentrations of heavily oxidizing acids such as nitric and sulfuric acid attack the photoresist as well. Phosphoric and hydrochloric acid attack the photoresist less detrimentally. However, as most of these acids are often used as supporting electrolytes, the photoresist also shows there some additional limitations.

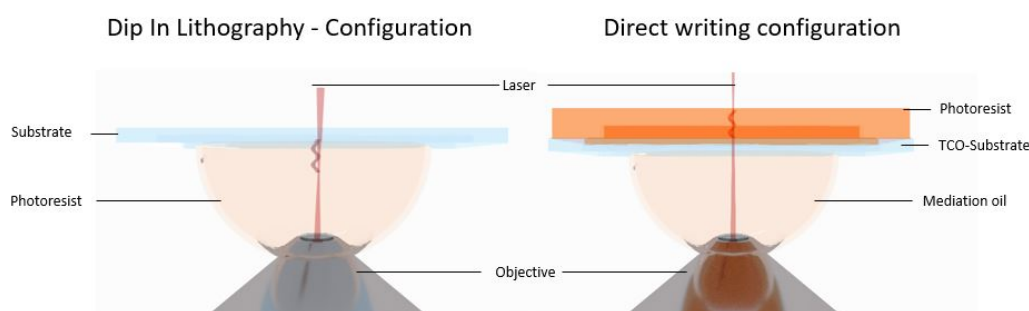


Figure 3.5 – The two configurations: Dip-in lithography configuration and direct writing configuration.

Two-photon lithography writing

Nanoscribe writing can be done in two different configurations, see figure 3.5. The laser can be focused through a refractive index matched oil and substrate into a photoresist. This method is used with spin-coated photoresist or non-commercial photoresists. The advantage is that spin-coated and soft bake photoresist can be patterned with high resolution and that the lense, can not be contaminated. Special care has to be taken into account when determining the interface. Thin layers of photoresist ($<20 \mu\text{m}$) will result in a mixture of the photoresist/air and photoresist/substrate interfaces, producing challenges for accurate writing. The disadvantage is that it can not be used with nontransparent substrates and that the maximal structure height is limited. The limit can be calculated as the focal length of the objective minus the thickness of the transparent substrate. In the configuration used in chapter 4.1, 4.2, and 5.2, this limitation in height is roughly $170 \mu\text{m}$. The other configuration uses liquid photoresist and the lense is directly moved into the photoresist. The minimal amount of interfaces for the laser to cross (see figure 3.5) combined with the refractive index matching of the resist to the objective allows for maximal resolution. The interface can be found accurately and the structure height is limited by the maximal retraction of the objective, in the case of this work, roughly $<1\text{cm}$. Furthermore, a nonconductive substrate such as silicon and silicon nitride can be used. The disadvantage is, that this configuration can only be used for liquid photoresists. The writing itself can be done in two different modes, see figure 3.6. Either the stage can be moved with the piezoactuators, allowing to move all three axes simultaneously, allowing for true 3D printing. The focal point of the laser stays fixed. As input, the matrix with the movement of the stage needs to be prepared. This mode can be used accurately but slowly. Faster writing speeds can be achieved by using a galvo mirror system. There, the X and Y-axis are scanned with the laser beam while the stage or the objective is retracted in the Z-axis. This layer-by-layer method allows to fabricate mesoscale structures with a scan speed up to centimeters per minute. Complete CAD files can be sliced vertically (hatching) and horizontally (slicing) and then be printed. The slicing and the hatching need to overlap to ensure the mechanical integrity of the print in the case of negative-tone photoresist. The overlap needs to be presented as well when working with positive-tone photoresist to avoid undissolved and detached parts of photoresist. The surface of the prints can be improved by using the laser to contour around the print after each layer is printed.

$$D = \tau * Laser_{\text{Power}} \quad (3.17)$$

The illumination dose, D , of the system is given by the time, τ , the laser resides within a volume and the laser power, $Laser_{\text{Power}}$. Therefore, the writing speed and laser power usually are optimized by a dose test. The dose has to reach the threshold to initiate a two-photon absorption. However, the dose has to stay low enough to avoid evaporating the photoresist partially. Due to the overlap in galvoscan writing, the energy delivered to a certain volume

might not be completely dissipated before the next layer gets scanned, therefore influencing the cross-linking reaction. This residual energy can lead to a higher amount of crosslinking in a small structure.

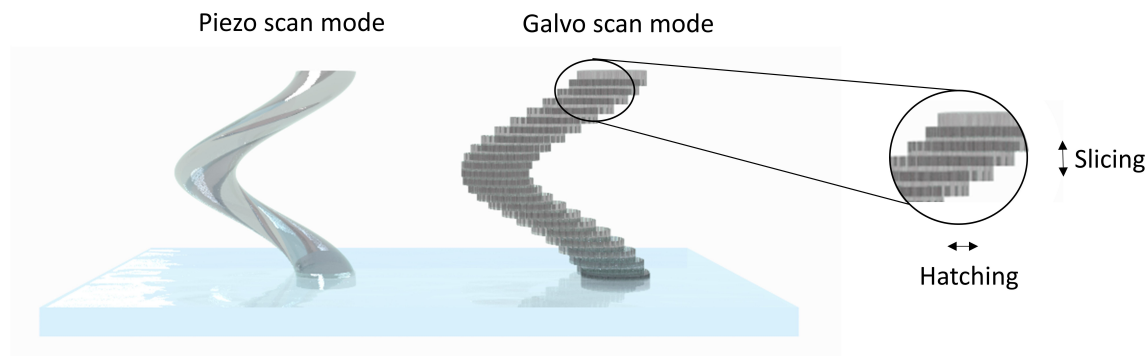


Figure 3.6 – Piezo- and Galvoscan mode. Piezo scan mode moves the substrate in all three axes simultaneously while galvoscan mode uses mirrors to deflect the beam and write in a layer-by-layer approach.

3.4 Micromechanical characterisation

Mechanical testing was introduced with the rise of MEMS materials, where a proper characterization became necessary[85] With it came the possibility of starting to test materials and study failure and deformation mechanisms into more detail. The advent of nanostructures such as graphene, nanotubes, and nanowires created an additional need for micromechanical testing. In this work, micromechanical testing was used as a means to characterize the mechanical response of the systems, considering that MEMS application would most likely be dependent on the mechanical properties of the structures. Therefore the mechanical structure, which allows us to determine if the structures behave as expected. Therefore the mechanical response can also be seen as quality control of the structures without performing time-consuming FIB cross-sections and/or tomography experiments, to detect porosity or large grain size deviations. The structures produced in this work can be investigated by compression testing. Testing in compression is the most frequently used test as the mechanical setup as well as the alignment is less complex than in tensile testing.[86]

NC and ultra-fine grained Nickel are interesting materials to study as they are often used due to their mechanical properties, for instance, hardness. Furthermore, while not being discussed in detail in this thesis, nanocrystalline nickel offers interesting mechanical phenomena to study. Such as Hall-Petch strengthening[87, 88], grain boundary shear and slip and a rather pronounced strain-rate insensibility until the strain induces grain growth[88], to name a few areas of study.

4 Single pore templates

4.1 Nanocrystalline micropillars

Declaration of contribution

In this work, Laszlo Pethö produced the ITO covered glass slides which were used as substrates. Patrik Schürch produced the CAD files, the templates, the electrodeposition simulation and electrodeposition of the samples, while Rajaprakesh Rachandramoorthy carried out the mechanical testing together with Jakob Schwiedrzik. The TEM images and TKD were taken by Thomas Edwards. Johann Michler and Laetitia Philippe supervised the work.

4.1.1 Introduction and aims

In this section, simple 2D templates and the influence of different features of such simple templates are discussed. One of the simplest mold designs is a 2D round pore. While most pore templates, such as anodized alumina and ion-track etched templates are often used to create nanowires, for mechanical testing such nanowires are rarely tested. The manipulation of these wires and the testing in compression or tension has rarely been attempted. The most common way to micromechanically test materials is via pillar compression.[89, 90, 91] The aspect ratio of these pillars should be kept below 3, so as to avoid buckling of the pillar. The majority of available literature on micropillar compression can be found using FIB-milled pillars. The milling of pillars via FIB is usually slow and difficult, due to the tendency for tapering and redeposition. Furthermore, when gallium ions are used in the beam, the infiltration of gallium ions into the material has shown to significantly influence mechanical test results. [89] Therefore, for some metals, it is crucial to create pillars without ion-infiltration to test the material without significant structural alterations.

A proven but rarely reported method for fabricating micropillars is to electrodeposit into a template. If the pillars are electrodeposited, the ion-implantation problem is avoided. In electrodeposition terms, pillar deposition is interesting, as it is the closest template shape

to the extensively studied damascene and through-hole via plating processes. Additionally, the through-hole via plating is exceptionally well studied at the micrometer scale. Griffiths et al focused on trench deposition and modeled the process to describe the electrode position taking place.[92, 93, 94] With most studies focusing on through-hole via plating and avoiding super-fill in damascene plating, the most substantial difference comes when using an inert resist.[95, 96] Having an inert resist on a conductive substrate avoids the super-fill phenomenon and leads to one-directional growth. Moreover, the possibility of modeling is substantially simplified, as the mesh becomes more uniformly distorted. Nevertheless, most literature covers electrodeposition in negative SU-8 templates with a gold-covered silicon wafer.[97] The common manufacturing technique is to over-deposit above the template edge and mechanically remove the overgrowth. This process can be used to create micro-components and was used during this thesis work to create microtensile test grippers.[86] To create pillars, this is not only difficult due to the potential risk of changing the deposit's mechanical properties during mechanical preparation, but there is also a risk of interface layer weakening between the metal pillar and substrate. In this work, a simple, yet effective method for avoiding/removing these technical difficulties is shown. The photoresist template is written on an FTO-substrate and subsequently electrodeposited in. The pillars are filled and a large overgrowth is deposited. This is followed by attaching the overgrowth to a holder. Subsequent sonication in acetone removes the photoresist and the FTO-layer, thusly creating a non-damaged pillar array. A version of this process can be seen in the following chapter 4.2 and in the publication of that work.[57] Furthermore, the microstructure and mechanical testing data are presented. Additionally, some basic electrodeposition simulations are explained with this simple design. This chapter is intended for providing a basis for the subsequent chapters.

4.1.2 Methods

The electrodeposition simulation was based on the simulation explained in chapter 5.1. The simulation was used to explain certain aspects of the geometrical placement of the structures and the importance of array symmetry, as all the structures in subsequent chapters were produced in large arrays. FTO coated microscope cover glasses were used and spin-coated with AZ9260 photoresist. The FTO slides were pretreated with oxygen plasma and a 5min dehydration bake at 160°C. The spin coat was performed at 500 rpm for 10 s and 1800 rpm for 60 s with a ramp of 250 rpm/s. The photoresist was soft baked at 110°C for 85 s. Subsequently, the samples patterned with a Nanoscribe Professional GT in direct writing configuration, see figure 3.5. The height of the pillars is given by the spin-coated thickness which is roughly 9 μm . The interface finding of the device is not able to recognize such thin layers aptly, as described by Alcântara et al.[55] Therefore, the CAD files, the pillars were elongated to ensure the pore would penetrate the entire thickness of the photoresist layer. The photoresist was illuminated at a laser power 16% of 50 mW with a scan speed of 5000 $\mu\text{m s}^{-1}$. The cylindrical shape that was illuminated was sliced into layers of 200 nm with hatching between the laser lines of 200 nm as well. After illumination, the photoresist was immediately developed for 10

min in AK400 developer solution diluted with water in a ratio 1:5 and washed in water for an additional 10 min. The specimens were stored in the cleanroom area at 25°C and a relative humidity of 50% until electrodeposition the subsequent day. Next, electrodeposition was carried out using a three-electrode setup with a soluble nickel counter electrode, an Ag/AgCl reference electrode in 3M KCl solution and the ITO coating of the glass slide became the working electrode. The chemicals $\text{Ni}(\text{SO}_3\text{NH}_2)_2$ (98%), NiCl_2 (99%), H_3BO_3 (99%), $\text{C}_7\text{H}_5\text{NO}_3\text{S}$ (99%), and $\text{CH}_3(\text{CH}_2)_{11}\text{Na}$ (99%) were purchased from SIGMA Aldrich and used without further refinement. The electrodeposition was carried out on Methrom PGstat20 at 50°C and at -1.2V vs Ag/AgCl. The deposition duration was set at 60min to ensure not only a filling but a significant overgrowth is grown. The overgrowth was glued to a sample holder with Araldite 2000s epoxy glue and dried overnight. Subsequently, the sample was put in acetone and sonicated for 5s, until the substrate was detached and the photoresist dissolved, leaving a pristine nickel sample glued to a copper SEM sample holder. The mechanical testing was carried out with an ALEMNIS AG standard assembly setup with an ALEMNIS smart tip indentation tip in displacement control.

4.1.3 Results and discussion

Influence of the pore shape, aspect ratio, and pore spacing

From a mechanical testing stand-point, circular pillars are the easiest to use, due to the symmetry of the design. However other shapes are also possible, e.g. square-base pillars have been reported in literature. From an electrochemical stand-point, the influence of the ordering of the pores on the neighboring pores is more detrimental, as can be seen in figure 4.1. The discrepancy in current density within pores is directly related to the size scale. On a centimeter-scale, the variations occurring during deposition are influenced by the ohmic resistance and can reach high values. However, with the decrease in size, the homogeneity of the deposition increases until nanoscale is reached. At the nanoscale, diffusion limitations occur and may cause highly inhomogeneous deposition, such as deposition of tubes.[98]

The ratio between active surface area and an inert surface is the most influential aspect. A model to calculate local current density based on an average active surface area per pixel was created by Drese et al.[99] The model divides the 2D templates into pixels and calculates a local current density for each pixel based on the active surface area. This works exceptionally well for large wafers with non-repetitive non-symmetrical patterns. In the case of this work, for simple pores, 3D FEM electrodeposition models can be used to explain and quantify the influence of the patterning. The simplest approximation to the FEM simulation is to draw a Voronoi cells around the pores. The higher the area of the cell the higher the current density in the pore. This is in agreement with FEM simulations and shows that if the pores are equidistant, the deposition is very homogenous from the start, whereas nonrandom arrays immediately influence the current density in the pores. Simulations for a nickel sulfamate electrolyte show that the influence of the spacing is small and can be further reduced by symmetrical arrays.

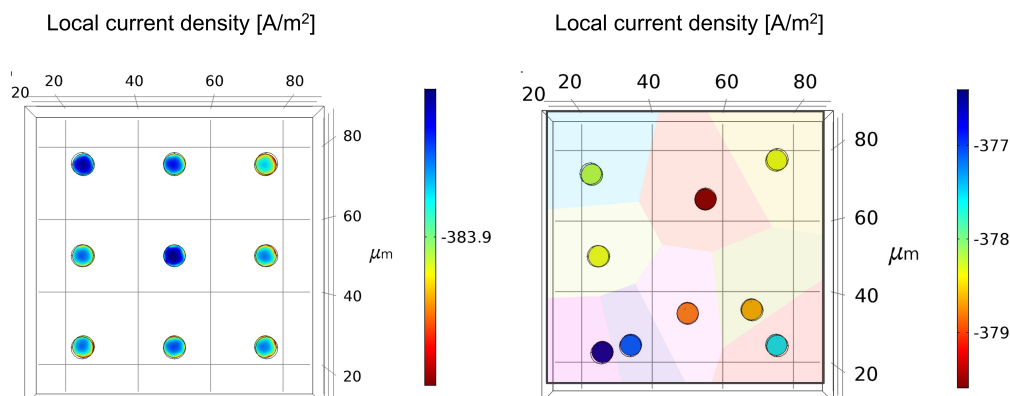


Figure 4.1 – Local current density simulation in [mA/cm^2] for a symmetrical and a random pore array after 20 s of deposition. In the random pore array, the voronoi cells belonging to the pore are indicated in different colors

This allows depositing structure arrays similar to pillars with a spacing ideal for mechanical testing equipment, rather than having to optimize the spacing for electrodeposition, as shown in the following chapters of the thesis. Furthermore, homogenous deposition additionally ensures a homogenous microstructure within the pillars. An important point of this basic study is that the wetting of templates needs to be as good as possible, as random pores filled with air can cause an inhomogeneous deposition as shown in the random array in figure 4.1.

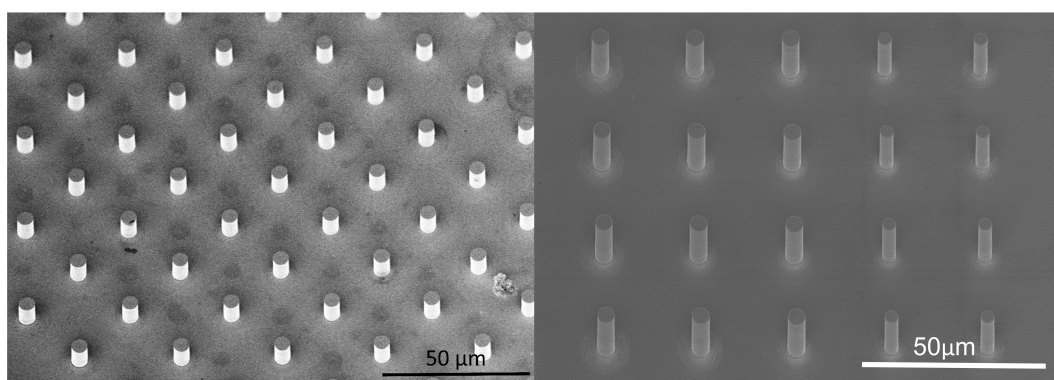


Figure 4.2 – Manufactured nc nickel pillars with inverse manufacturing method of different aspect ratio pillars, with the pillars on the right having an aspect ratio of 1:1.5 and on the right of 1:3.

Produced pillar arrays and microstructure analysis

Pillars were deposited using the inverse method and their microstructures were investigated via TEM of FIB-cut lamellas. The pillars seem to have a nanocrystalline top with finer grains, where initial nucleation took place. This is followed by a nanocrystalline microstructure with elongated grains in the growth direction normal to the 110 plane. According to the TKD data gathered from the bulk of the pillar, the average grain size is approx. 30 nm in XY-directions and up to 100 nm in the Z-direction. Furthermore, the pillars appear to exhibit twinned grains, which has also been reported in the literature.[100] The growth of these twins is most likely linked to 2D nucleation of elongated grains in the (110) direction.[100] Most importantly, the pillars show no sign of porosity. The overgrowth exhibited minor unevenness in the places between the pillars, see figure 4.3.

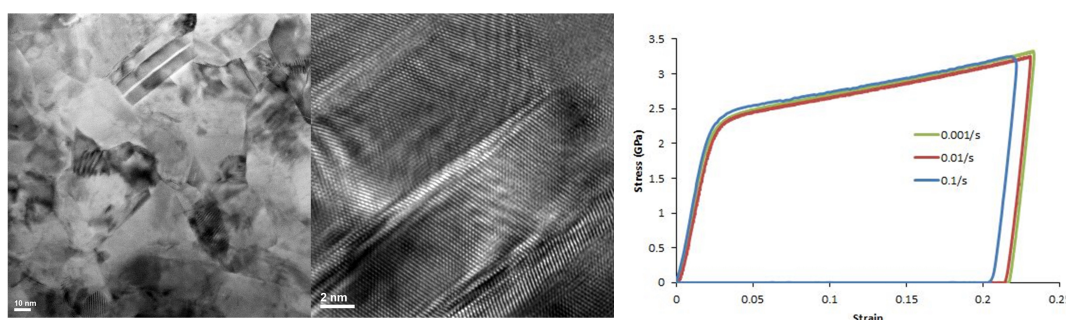


Figure 4.3 – TEM investigation of fib-cut lamella of nc-nickel pillars on the left and middle, and a mechanical testing response, stress versus strain, to different strain rates on the right.

Mechanical Testing

Mechanical testing was performed to investigate the quality and hardness of the nickel pillars. As expected, the pristine electrodeposited pillars displayed higher hardness than FIB milled pillars, namely 2.35 GPa yield strength compared to FIB milled pillars by Mohanty et al [56], which showed a considerably lower yield point, even though being electrodeposited from a similar sulfamate electrolyte. Furthermore, the mechanical response shows significantly less variation in the pristine pillars, than the pillars used in the work of Mohanty et al.[90] The pillars showed no significant strain-rate dependency, with a strain parameter M of 0.00033. Moreover, the mechanical response indicates similar grain size and amount of twinning within the different pillars, as deviations in grain size and twinning would either increase or decrease the mechanical hardness, due to Hall-Petch and deformation twinning phenomena.[101]

4.1.4 Conclusion

Pillars fabricated via TAE exhibit good design accuracy. The geometry of the pillars is taper-free and the top of the pillars is almost perfectly flat. The accuracy of the geometry as well as the deposition of an overgrowth that turns into the pillar substrate, yielding pure nickel samples,

which is ideal for mechanical testing. The deposition is homogenous throughout the array, showing that the method is ideal for batch production. The achieved microstructure was comparable to literature, [102, 90, 100] suggesting that nickel sulfamate electrolytes may be used to produce high-quality 2D structures. The simulation indicates that the creation of arrays does not significantly influence the growth and can be used in the following chapters. Mechanical testing revealed that the Young's modulus for these pillars is in good agreement with literature [90], i.e. 173 GPa. The unprecedented consistency of the attained values from pillar compression tests demonstrate that TAE is a reliable additive manufacturing technique, with the nickel sulfamate electrolyte being a suitable electrolyte for the fabrication of 3D structures.

4.2 Nanocrystalline nickel microsprings

Declaration of contribution

In this work, Laszlo Pethö produced the ITO covered glass slides which were used as substrates. Patrik Schürch produced the CAD files, the lithography templates and the electrodeposition of the samples, while Rajaprakesh Rachandramoorthy carried out the mechanical testing. Johann Michler and Laetitia Philippe supervised the work.

This work has already been published in Schürch, P.; Ramachandramoorthy, R.; Pethö, L.; Michler, J.; Philippe, L., *Applied Materials Today* 2019, 100472.

4.2.1 Introduction and aims

Microsprings, also referred to as microcoils and microhelices, are some of the most prominent architectures among 3D structures designs. They have a multitude of possible applications, e.g. MEMS packaging [102], high frequency antennas [103, 104], pressure sensors [105], electrochemical pH sensors [106], chemical sensors [107] and microactuators [8], due to their attractive mechanical properties including superelasticity [108, 109], ultralow stiffness [110] and high elastic energy storage [108]. Other unique applications for such microsprings are microrobots [25, 27] and photonic wave-guides [84]. The simple design and plethora of possible applications have contributed to the continuously increasing interest of microsprings in a wide research community. In the past, a variety of manufacturing methods have been used to tune the mechanical properties of the microsprings, such as varying the geometry and material. Furthermore, a variety of different mechanical testing methods has been used to characterize these microsprings.[105, 110, 23, 111] Precise compression testing has not yet been reported in literature at the microscale, due to the limitations of the various different fabrication processes, such as alignment and adhesion issues. The fabrication process employed in this work allows for complete design freedom regarding the minor/major diameter and the pitch of the spring while providing a substrate and a flat top layer from the same material. The top layer enables precise micromechanical compression testing, providing cru-

cial insight for applications, such as shock mitigation and impact absorption. An interesting, yet previously unexplored material for the fabrication of microsprings is nanocrystalline (nc) nickel, which exhibits extraordinary mechanical properties, e.g. high hardness [112, 91], high yield [91, 113, 114] and fracture strength [111, 114], as well as excellent wear resistance [58]. Furthermore, nanocrystalline nickel offers interesting chemical properties, like high corrosion resistance [115] and good catalyst properties, especially in binary [116, 117] and tertiary alloys [118]. Beyond creating microsprings, these aforementioned properties highlight the promise of nc-nickel for the fabrication of complex 3D metal micro-architectures for various applications. In this work, a combinatorial approach of electrodeposition and two-photon lithography [84, 57, 25, 119] was used to create 3D micro-architectures. The localization of the chemical reaction in the focal point of the laser in two-photon lithography allows for the creation of 3D templates with submicron accuracy and almost no geometrical restrictions, while electrodeposition offers a high amount of control over the deposits' microstructure, composition and internal stress. However, to fully combine the advantages of both processes, the influence of template on electrodeposition needs to be understood, especially those with significant confined spaces. Several previous experimental and theoretical works have been conducted on 2D systems to address the different challenges of TAE, such as convection in narrow trenches [120], template filling ratios [96], influence of additives on trench filling [121, 122, 95] and macroscale feature density [99, 123, 124, 125, 126]. Based on prior studies, this work includes a 3D electrodeposition finite element (FE) simulation to determine the effect of a 3D template on electrodeposition. Simulating and controlling the electrodeposition process is a key tool to understand the influence of the template. Here, we present a holistic study from the electrodeposition of geometrically highly precise nanocrystalline nickel microsprings to micromechanical characterization by means of compression testing. We provide novel insight into the influence of template on electrodeposition, as well as possibilities and necessities when electrodepositing into a confined 3D microscale template. We demonstrate the creation of fully metallic, nanocrystalline nickel microsprings and microspring arrays. We provide extensive microcompression test data to show the ability of the springs to sustain repeatable loads. Further research using this fabrication method and the properties of such 3D micro-architectures has the potential to facilitate the fabrication of architected materials with specifically tailored mechanical properties.

4.2.2 Methods

A Nanoscribe Professional GT was used to create templates for the microsprings. The structure was written with a 63x magnification objective through Zeiss immersion oil (Nanoscribe, Germany) through a 120 μm thick ITO-coated glass slide into AZ9260 (Microchemicals, Germany) positive-tone photoresist. The glass slide was first cleaned for 5 minutes in a 100 W O₂-plasma, followed by a dehydration bake of 15 minutes at 160°C. The photoresist was then spin-coated onto the ITO slide with a Sawatec SM-150. A first spin coat step was done at 2400 rpm for 60 seconds followed by a soft bake of 4 minutes at 110°C. To achieve the desired thickness, a second spin coat was performed at 2100 rpm for 60 seconds and 8 minutes of soft bake

at 110°C. Using Nanoscribe Software 'Describe', the 3D CAD design of the microsprings was sliced vertically, hatched laterally and was exposed with a laser power of 11 mW and a laser speed of 9000 μms^{-1} . Subsequently, the specimen was developed in 1:4 AK400 Developer (Microchemicals, Germany) / H_2O for 45 minutes and cleaned in distilled water for 15 minutes. Next, electrodeposition was carried out using a three-electrode setup with a soluble nickel counter electrode, an Ag/AgCl reference electrode in 3 M KCL solution and the ITO coating of the glass slide became the working electrode. The electrolyte was composed of 1.19 M nickel sulfamate, 0.3 M nickel chloride, 0.75 M boric acid 0.19 M saccharine and 0.04 mM sodium dodecyl sulfate. The chemicals $\text{Ni}(\text{SO}_3\text{NH}_2)_2$ (98%), NiCl_2 (99%), H_3BO_3 (99%), $\text{C}_7\text{H}_5\text{NO}_3\text{S}$ (99%), and $\text{CH}_3(\text{CH}_2)_{11}\text{Na}$ (99%) were purchased from SIGMA Aldrich and used without further refinement. The electrodeposition setup was controlled by a Metrohm PGStat202 and deposition was carried out in potentiostatic mode at 60°C without agitation and a voltage of -1.2 V vs Ag/AgCl. Deposition time was 60 minutes to ensure a large overgrowth was produced. The sample was subsequently removed from the electrochemical cell and a typical aluminum SEM stub was glued onto the overgrowth with Huntsman Araldite two-component epoxy-glue. The thickness of the overgrowth, which provides the metal substrate to the microsprings, is crucial for the inversion process. The photoresist was then removed via sonication in acetone, which also detaches the ITO coated glass substrate, leaving behind the SEM stub with the metal microsprings, as summarized in figure 4.4. The samples were further cleaned in acetone for 5 minutes, followed by 5 minutes in isopropanol.

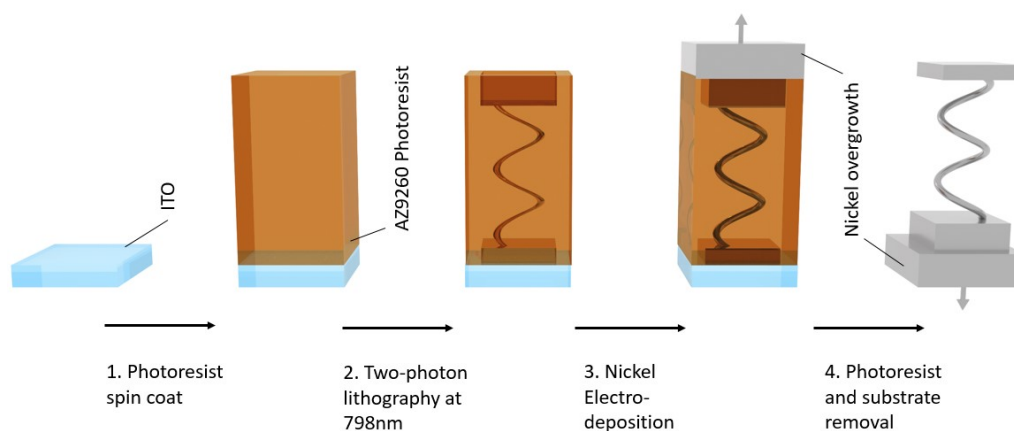


Figure 4.4 – Inversion process to create nc-nickel microsprings. 1) AZ9260 is spin-coated onto the ITO coated glass substrate, 2) the pattern is illuminated by two-photon lithography to create the template, 3) nickel electrodeposition is carried out and an overgrowth is created, 4) the overgrowth is glued to an SEM stub, the photoresist is removed and the ITO-glass substrate is detached.

Mechanical testing

The nanocrystalline nickel microsprings were mechanically tested in compression using an in situ micromechanical tester from Alemnis AG inside an SEM. The monotonic loading

tests were conducted under displacement control at a speed of $0.12 \mu\text{ms}^{-1}$. Subsequently, two different cyclic loading tests, namely with increasing displacement and constant mean displacement, were also conducted under displacement control with an oscillation frequency of 0.5 Hz. A detailed description of the experimental setup and methodology is provided elsewhere.[89]

FEM Simulation

Electrochemical simulation

A time dependent tertiary current-based 3D finite element electrodeposition simulation was conducted using COMSOL Multiphysics 5.3 software with the electrodeposition module. The set of equations used for these simulations is based on our prior work [57, 56], determining the ion flux based on the Nernst-Planck equation, a mass and current balance equation, the electrode growth velocity equation based on the local current, and the Nernst-Einstein relation to yield the ion mobility. The Butler-Volmer equation used in this work was adapted to be concentration dependent:

$$i_{loc} = i_0 C_r e^{\frac{\alpha_a F \theta}{RT}} - e^{\frac{\alpha_c F \theta}{RT}} \quad (4.1)$$

where: i_{loc} - the local current density, which is calculated with i_0 - the exchange current density, C_r and C_o - the concentration of the reducing and oxidizing species, respectively, and α_c and α_a - the exchange transfer coefficient of the cathodic and anodic transfer coefficient, respectively. The chemical reaction considered in this simulation is the deposition of nickel. The simulation does not include additives or non-electroactive constituents. The multiscale model approach of our previous work [57, 56] was used to account for the macroscale cell geometry while predicting microscale growth. Boundary conditions used for the simulation can be seen in figure 4.5a. The 3D template of interest is connected to a block of bulk electrolyte. An open boundary is placed around the block of bulk electrolyte to ensure electrolyte replenishment. The growing electrode surface is located at the bottom of the template. The use of a sacrificial auxiliary working electrode around the sample enables the assumption that the electrolyte potential at a given height above the sample is fixed. The meshing of the electrochemical model was divided into two domains with the bulk electrolyte meshed coarsely, while the template pore was meshed finely.

Mechanical Simulation

A linear elastic mechanical simulation of the microsprings was carried out with the structural mechanics module in the COMSOL Multiphysics software. An eigenfrequency analysis was conducted on the different microspring designs including a substrate from the same material,

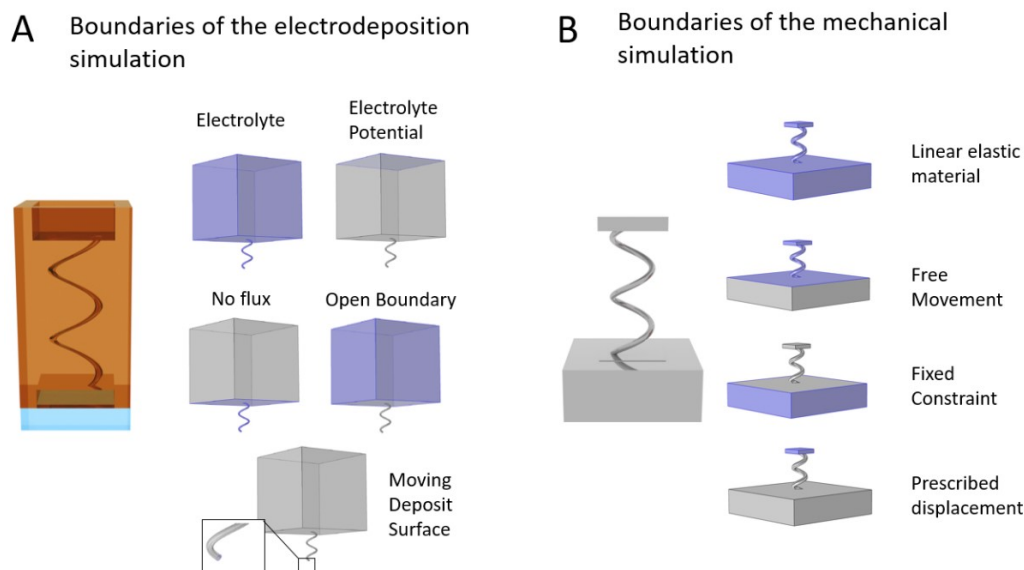


Figure 4.5 – A) Microscopic electrodeposition model boundary definitions and B) mechanical model boundary definitions.

the spring/spring arrays and a top plate from the same material. Dimensions were measured from SEM micrographs for each of the three experimentally tested spring types and recreated in the COMSOL software. In the experimental case, the microsprings are located on top of the overgrowth of the nanocrystalline nickel. Therefore, in simulations, the springs with the top plate were also placed on a block of substrate material with fixed constraints. The movement of the top plate was constrained by predictive boundaries, to restrict its movement in the X and Y direction, which in turn avoids the bi- and tri-axial eigenfrequency modes. The density and Poisson's ratio of nanocrystalline nickel, $\nu = 0.31$, was taken from previous studies in literature [113]. The Young's modulus used in the simulations was 173 GPa determined prior by micropillar compression of pillars produced with the same process. The pillars were produced this way to avoid the influence of FIB-induced damage on the measured modulus. The Young's modulus values are in agreement with values previously reported in literature [113]. The input values and the input dimensions for the simulation can be found in the appendix (Appendix table 2 and table 3).

4.2.3 Results and discussion

Electrodeposition

Top-layer Deposition

The top plate in the microsprings is essential for self-alignment with the diamond flat-punch used during the mechanical tests. However, the introduction of a bottleneck in the template, as can be seen in figure 4.6a, is unique to the spring design in this work. To understand

the influence of this bottleneck, a large void was left at the substrate in the electrochemical simulations. As there is a conductive substrate at the bottom of the void, it is possible to induce growth across its entire area. The simulation shows a largely homogenous electrodeposition, albeit lower current density in the large void compared to the current density in the pore, as shown in figure 4.6. However, with continuing growth of the metal the deposition gets concentrated right below the pore opening, which increases the current density significantly during the deposition into the pore.

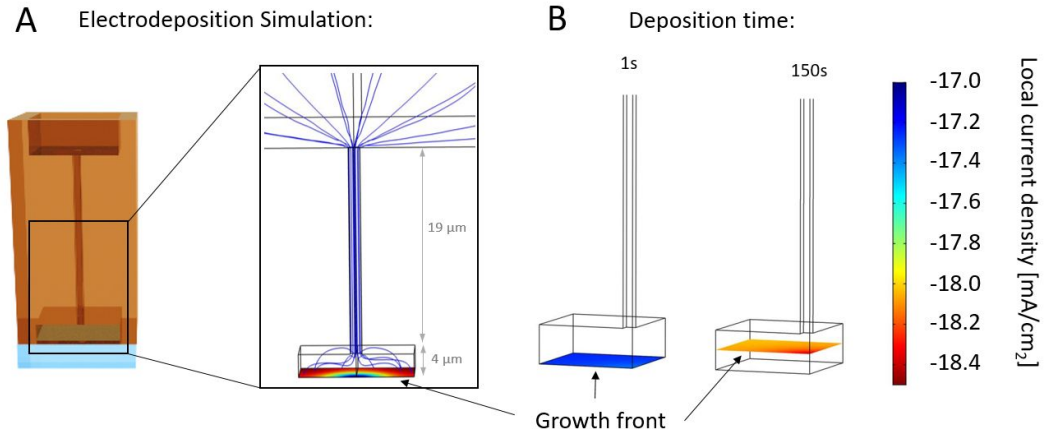


Figure 4.6 – A) Microscale electrodeposition model geometry for a void below a pore with the growth front colored and the current density vectors in blue. B) Deposition progress and local current density after 1s and 150s of deposition.

In a macroscopic scale setup, the Wagner number is often used to describe the uniformity of a deposit on an electrode obtained by dividing the activation resistance of the surface reaction by the ohmic resistance [16]. As the electrolyte has high conductivity and the template geometry is in the microscale, unfortunately, this approach cannot be used. In microscopic scale, Landau et al used a similar approach to calculate the leveling parameter L , by dividing the activation resistance by the mass transfer resistance, as shown in the equation below [123]]:

$$L = \frac{R_\alpha}{R_c} = \frac{ni_{lim}(1 - \frac{i}{i_{lim}})}{\frac{\alpha}{i}} \quad (4.2)$$

where: n - number of transferred electrons, i_{lim} - limiting current density, i - local current density and α - charge transfer coefficient. Using a value from literature [75] for the limiting current density, 2000 Am^{-2} , and the rest of the values from the electrochemical simulation (see Appendix, table 1) yields a leveling parameter significantly exceeding 1. Therefore, the low current density in the void below the pore considerably increases the uniformity of the plating. The simulated homogenous growth rate and the leveling parameter suggest that at this stage, growth is neither mass transfer nor ohmic resistance controlled. The filling of a large

perpendicular void below a pore is possible directly at the conductive substrate, due to a low current density and high electrochemically active species concentration. It should be noted that a lower current density is known to produce up to 3 times larger grains in nanocrystalline nickel deposition [127].

Deposition into a singular pore

The most prominent spring design is the classical helical spring, however, a multitude of linear and nonlinear springs exist. Therefore, the influence of the pore shape was studied. First, deposition into a simple straight pore was modeled for comparison with other shapes, as can be seen in figure 4.7. The deposition starts and reaches a quasi-stable average current density with a slight increase, as the pore gets shorter during ongoing deposition. This phenomenon has been identified previously, as the increase in contribution of 3D diffusion at the mound of the pore compared to the contribution of 2D diffusion along the pore during continuous deposition.[98, 128] The simulation automatically accounts for the difference in concentration, due to the earlier mentioned concentration dependent kinetics in equation 1. The current density is significantly higher in the pore than in the void below, causing the leveling parameter to be significantly lower yet still above 1, suggesting there is uniform growth within the pore as well. The higher, quasi-stable current density allows the assumption of uniform grain size distribution in the pore and that they are significantly smaller than the grains within the deposited void below the pore, which eventually form the top plate of the microsprings.[127]

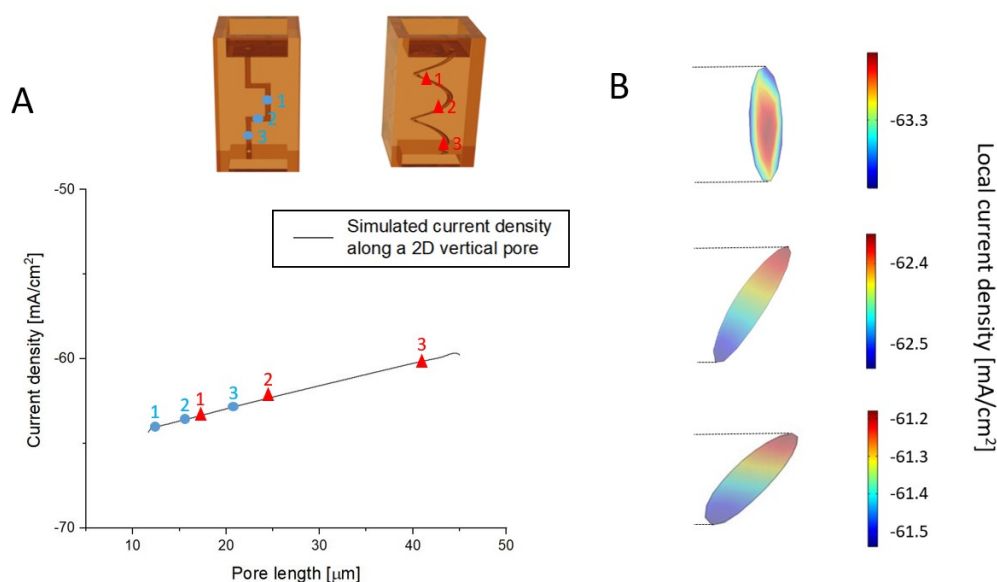


Figure 4.7 – A) Current densities simulation result in mA/cm² versus pore length: 2D pillar pore (dark gray), selected spots during growth of a 3D pore with rectangular turns (blue) and selected spots during growth of a helical shaped pore. B) Current density of growth fronts at a calculated pore length of 30µm with different inclination at 0°, 45° and 60°

As seen in figure 4.7, a comparison of simulated current densities in differently shaped pores with the same diameter shows no particular influence of the pore geometry. The 3D shape of the pore increases the pore length, therefore influencing the current density in the same manner as the depth influences the current density in a 2D vertical pore. This opens up interesting possibilities of creating non-helical or non-linear springs or more complex structures with a combination of different 3D-shaped pores with a similar actual pore length. A minor deviation from the average current density in the 3D template can be caused when the shape of the pore forces the growth front to be non-perpendicular to the pore, as shown in figure 4.7. The more inclined the growth front, the higher the non-uniformity of the growth rate. Furthermore, a drop in current density is observed with increasing inclination caused by the increase in surface area of the growth front in the pore. The deviation from the mean average current density is, however, negligible in the microspring geometry. Different designs of microsprings were deposited simultaneously on a single substrate, as shown in figure 4.8. Single springs with a pitch of two were successfully created, as well as arrays of four springs with pitch of one and two. The substrate was successfully detached and the microsprings with flat square top plates were obtained. Each spiral has an x-y dimension of 10 μm by 10 μm and a 2 μm thick top plate. The minor/major diameter, pitch and height of the microspring samples were determined via SEM micrographs prior to performing mechanical tests. These dimensions were accurately reproduced in the model used for mechanical simulations. The samples showed that the minor diameter of the deposited springs differed from the intended value of one micrometer, due to the photoresist's high sensitivity to the laser's power and scanning speed. The top-layer exhibits small deviations in thickness of $\pm 200\text{ nm}$, due to photoresist rehydration and accuracy limit of the interface determination in the two-photon lithography. The high filling ratio shown by the simulation proves that the limiting factor in geometrical accuracy is the accuracy of the template. Subsequently, Scherrer analysis of the 111 and 100 peak in the XRD data (Appendix figure 2) determined a grain size of 21 nm ($\pm 4\text{ nm}$) for the electrodeposited nanocrystalline nickel.

Mechanical properties

Monotonic loading tests were performed on the different springs to investigate the typical compressive behavior, as shown in figure 4.8. It can be seen that depending on the pitch and the number of springs in an array, both the elastic modulus and yield can be tailored. As expected, the larger the pitch and the number of springs in an array, the higher the mechanical properties. Subsequently, cyclic loading tests were also performed on the three samples, as shown in figure 4.9. Cyclic loading was achieved by performing repeated load, unload and reload cycles with increasing mean displacement. The retraction during the unloading cycle was restricted to make sure that the indenter did not lose contact with the spring.

All the samples show an initial toe region during the first loading, which can be attributed to the alignment of the flat punch to the metal top plate. Afterwards all samples exhibit an elastic regime, where the unloading slope and the reloading slope of the next cycle match. Past

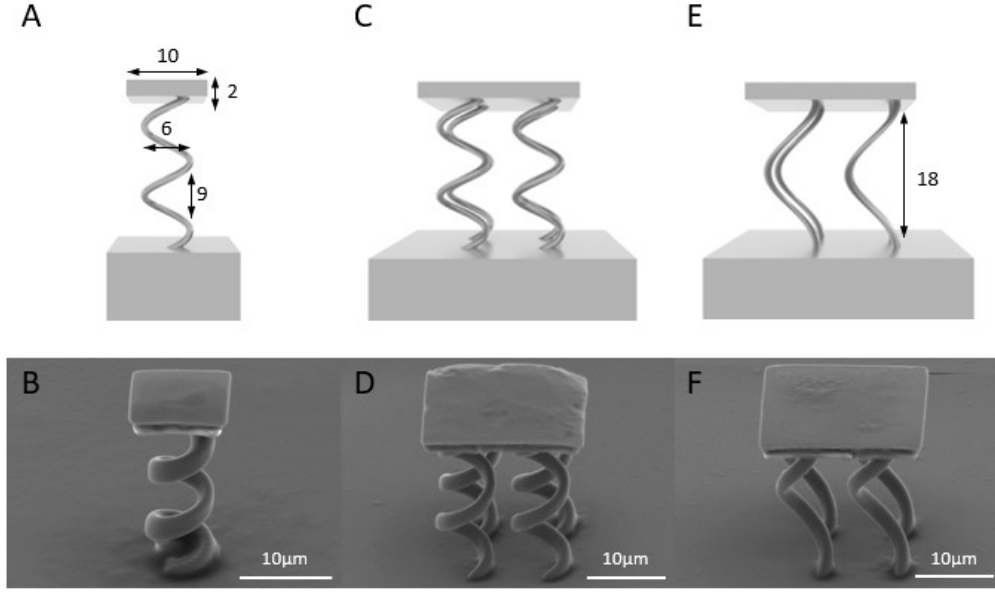


Figure 4.8 – Different microspring designs (A, C, E) with appropriate dimensions indicated in microns and SEM micrographs (B, D, F) of the deposited structures at 45° tilt.

the elastic regime, all samples diverge strictly from the elastic behavior and enter the plastic regime. With each additional cycle and increasing displacement, the hysteresis of the unload-reload cycle increases. These changes are due to permanent plastic deformation within the microspring. This was corroborated visually by the decreased height of the microspring after the mechanical testing (see Appendix Figure 3).

From the mechanical data, spring constants were extracted (see Table 4.1) from the unloading slopes in the elastic region. The full metal nc-nickel microspring arrays show a significantly higher spring constant as compared to a single microspring. Setting our results against those in literature, smaller cobalt coted silicon springs (350 nm minor and major diameter, 4.5 μm high with a pitch of 1 μm) were tested by Singh et al [23] with an conductive AFM probe to yield an spring constant of 10-32 Nm⁻¹.

Mechanical simulations of the microsprings were conducted to estimate the natural frequency in Z- direction. The yielded simulation values were compared to the theoretically (figure 4.1 calculated ones using the mass on a spring formula, as shown below in equation:

$$f_0 = \frac{1}{(2 * \pi)} \sqrt{\frac{D}{m}} \quad (4.3)$$

where: f_0 - natural eigenfrequency, D - spring constant extracted from the slope of the unloading cycles in the elastic regime from experiment, and m - mass of the microspring calculated

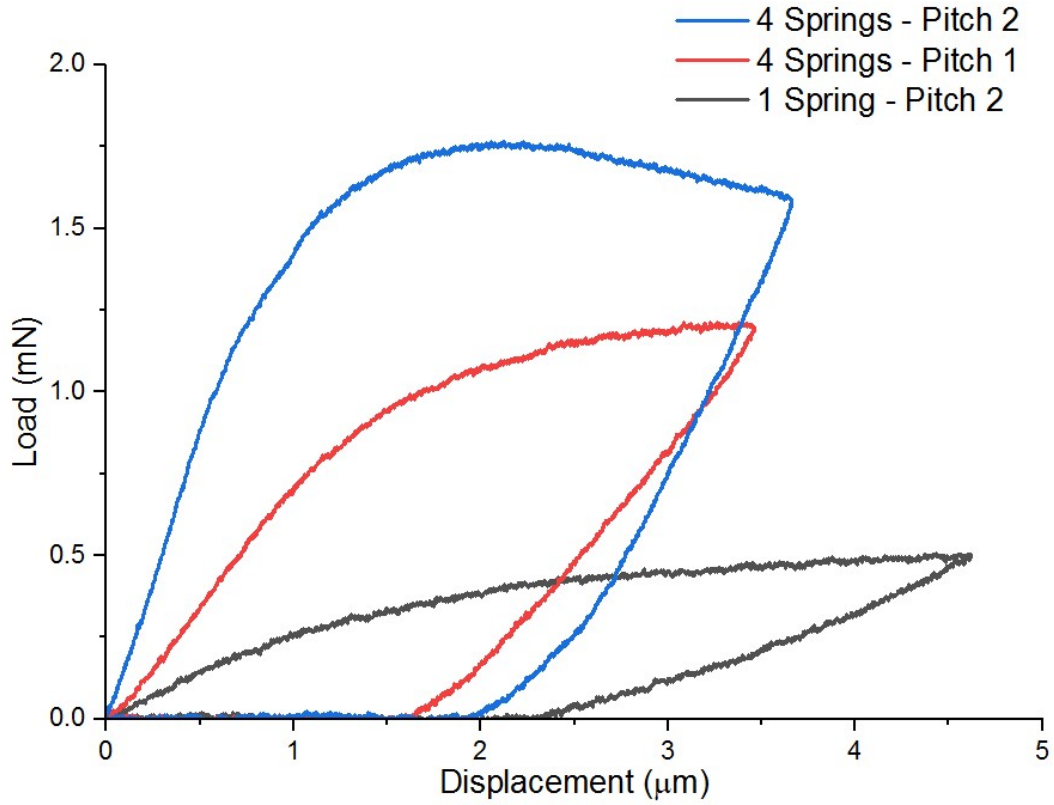


Figure 4.9 – Monotonic spiral loading curves for 1 single spring with pitch 2 (black), 4 springs with pitch 1 (red) and 4 springs with pitch 2 (blue).

based on the volume estimated from the dimensions measured using the SEM images and the density of nickel, 8908 kgm^{-3} .

The eigenfrequency of the microsprings calculated from the simulation and the theoretical/-experimental values agree well with each other. The single spring system yields the lowest frequency compared to the spring arrays, proving that the geometry of the spiral, the number of springs and the thickness of the top plate can be used as variables to tune the natural frequency and other mechanical properties as required for varied applications.

A creep stability test was performed on a single spring with pitch two, with a mean displacement of $3 \mu\text{m}$, followed by 50 cyclic oscillations with amplitude of $1.5 \mu\text{m}$ at a frequency of 0.5 Hz. As seen in figure 4.10, nanocrystalline microsprings exhibit a typical stress-relaxation behavior seen by the decrease in mean load over time from 0.3 mN to 0.2 mN, before load stabilization. Extensive literature exists on the creep and stress-relaxation properties of nanocrystalline nickel micropillars.[56, 129, 130] Typically, the stress relaxation behavior can be attributed to deformation mechanisms, like dislocation-grain boundary interactions, grain boundary diffusion, and grain boundary sliding.

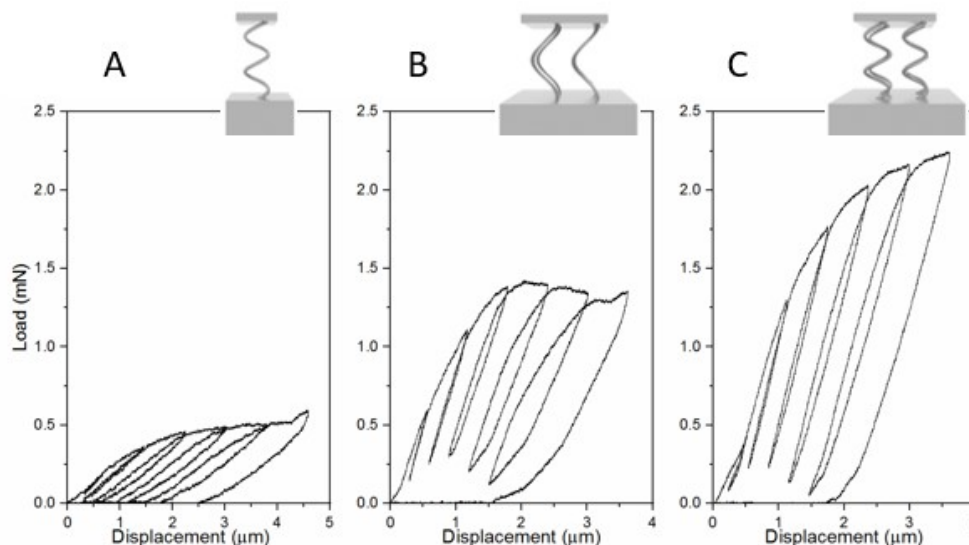


Figure 4.10 – Experimentally determined cyclic load-displacement curves at increasing mean displacements of A) a single microspring with pitch 2 B) a 4-microspring array with pitch 1 and C) a 4-microspring array with pitch 2.

Table 4.1 – FEM simulated versus spring frequency calculated from mechanical testing

Simulated eigenfrequency [MHz]	Calculated spring constant [Nm ⁻¹]	Calculated eigenfrequency [MHz]
1.94	287	2.03
2.53	1800	2.49
2.39	1473	2.25

4.2.4 Conclusion

In summary, our work highlights that nanocrystalline nickel 3D micro-architectures can be accurately designed and produced by a combination of electrodeposition and two-photon lithography. The electrodeposition simulation shows that the 3D shape of a pore merely acts as artificial increase in aspect ratio by prolonging the actual length of a pore. Furthermore, the simulation shows that high filling ratios can be achieved in large voids on the substrate interface, due to high active species concentrations and high conductivity of the electrolyte. The microcompression tests show that the microsprings exhibit elastic deformation at small displacements and enter a plastic regime at larger displacements. Cyclability testing proves that the springs are able to sustain repeated loads, however, minor stress relaxation can occur during the tests. Finally, the mechanical properties determined from our experiments show

excellent agreement with the mechanical simulations. The experimental parts combined with the simulations prove that in the future, the feasibility of electrodeposition into a template can be accurately determined and the mechanical properties of full metal 3D micro-architectures can be tailored to fit the intended applications.

5 Complex templates

5.1 Nanocrystalline nickel microshear structures

Declaration of contribution

Patrik Schürch produced the CAD-files, the templates, electrodeposited and removed the photoresist, as well as provided the SEM-images, the simulation, and the electrochemical analysis. Laszlo Pethö was supervising for the cleanroom procedure as well as suggesting the photoresist removal technique. Jakob Schwiedrzik designed the mechanical testing structure and provided support for the FEM-Simulation. Johann Michler and Laetitia Philippe supervised the work and provided the facilities to carry the work out.

This work has been published as: Schürch, P.; Petho, L.; Schwiedrzik, J.; Michler, J.; Philippe, L., *Advanced Materials Technologies* 2018, 3 (12), 8. This chapter uses figures of this work with the permission of John Wiley and Sons.

5.1.1 Introduction and aims

Electrodeposition into templates faces a plethora of challenges as previously mentioned in chapter 2. Homogenous, cavity-free deposits with a high filling ratio of the template require homogenous deposition conditions, which can be complex to monitor. In 2D LIGA, a majority of challenges were addressed and simulated. Griffiths et al [92, 131, 94] pioneered LIGA simulation and focused on transport limitations occurring in templates. Nilson et al [132] added a detailed description of natural convection in templates and Chen et al [120] optimized moving boundaries in FEM simulation for electrodeposition. Tsai et al [133] discussed ion concentration gradients in high aspect ratio with a tertiary current distribution model. Pulsed electrodeposition, a frequently used technique to improve the homogeneity of the deposits, was used and modeled by Yeh et al [134] Similar to the 2D LIGA process, 3D LIGA was used to create structures neglecting to study and describe the electrodeposition into the templates. In addition to the already existing difficulties, 3D deposition offers multiple additional challenges. Large changes of the active area in vertical direction, bottleneck features within the templates,

lateral diffusion and migration of the electrolyte constituents have to be considered [135] Furthermore, 3D templates can shield and deflect electrolyte current density vectors inducing changes in local current density. To understand the aforementioned challenges, this work exploits 3D nanocrystalline nickel electrodeposition simulation built upon the previously mentioned 2D electrodeposition simulation studies. The simulation is verified by nickel electrodeposition from a nickel sulfamate electrolyte [136, 75, 81] into 3D micro printed electrode arrays. Nickel is a suitable material for electrodeposition as it is thoroughly researched as well as simulated. Nickel sulfamate electrolytes produce low internal stress deposits, crucial for 3D microstructures. Nickel sulfamate can also be used for pulsed electrodeposition, involving long, low current pulses, another technique instrumental to ensure good filling ratio.[136] To display the potential of the process, we present a new variant of a 3D LIGA process using negative-tone photoresist for the creation of electrodeposition templates and the subsequent stripping of the tone resist. Negative-tone photoresist exhibit very high chemical resistance compared to positive tone resist used mainly so far.[97, 32] Negative tone resist offers higher resolution enabling the creation of better-defined templates and increases the possible height of the templates.20 Furthermore, negative-tone resists offer higher chemical resistance and widen the range of possible electrolytes to include sulphuric and nitric acid-based liquids and organic solvents compared to the most common positive tone photoresist used with two-photon lithography. We aim to explore the feasibility to electrodeposit a large number of architected structures such as microlattices [38, 36, 11, 9, 10], MEMS-components [137] and microfluidic structures [138, 7, 139]. At the same time, we want to investigate to assess the mechanical properties of the deposited material. For this reason, we decided to study a complex structure and the influence of the template in this work. The structure allows direct mechanical testing after deposition. Finally, bridge-like nanocrystalline nickel microstructures were electrodeposited for future mechanical testing and are used in this study to discuss electrodeposition parameters and template design. The design is similar to specimens created with focused ion beam (FIB) milling from copper by Pfetzing-Micklich et al.[140] From an electrodeposition viewpoint, the geometry was chosen due to the following challenges it exhibited: lateral diffusion and growth, as well as lateral and horizontal bottleneck features in the template.

5.1.2 Methods

Two-photon lithography

Templates were created using a Nanoscribe Photonic Professional GT system in dip-in lithography configuration with a 25x magnification objective. The ITO covered glass substrates were cleaned for 5 min in 200 W oxygen plasma prior to the lithography process. The laser beam was moved with a speed of 10000 $\mu\text{m/s}$ and a laser intensity of 9 mW/cm^2 . IP-S photoresist (Nanoscribe GMBH, Germany) was used. The samples were developed in 1-methoxy-2-propanol acetate (99.4%) for 15 minutes followed by cleaning step in propan-2-ol (99.8%) for additional 15 minutes. Both chemicals were supplied by Sigma-Aldrich. The templates were

descummed with 30 s of 100 W oxygen plasma treatment, prior to the electrodeposition, to facilitate electrolyte infiltration.

Nickel electrodeposition

Nickel was deposited from nickel sulfamate electrolyte containing: 1.19 M nickel sulfamate, 0.3 M nickel chloride, 0.75 M boric acid, 0.19 M saccharine and 0.04 mM sodium dodecyl sulfate. The chemicals, $\text{Ni}(\text{SO}_3\text{NH}_2)_2$ (98%), NiCl_2 (99%), H_3BO_3 (99%), $\text{C}_7\text{H}_5\text{NO}_3\text{S}$ (99%), and $\text{CH}_3(\text{CH}_2)_{11}\text{SO}_4\text{Na}$ (99%), were purchased from SIGMA Aldrich and used without further refinement. Deionized water (18.2 M Ω) was used to dissolve the electrolyte constituents. The deposition was carried in a three electrode setup with an ITO-covered glass substrate as working electrode, a nickel counter electrode and an Ag/AgCl reference electrode. A Methrom PG-Stat202 was used and deposition was made in potentiostatic mode at 60 °C without agitation. The electrolyte infiltration was assured by drop-casting a droplet of deionized water onto the substrate and placing it in a desiccator for 5 minutes. Direct deposition was carried out was carried out at -1.2 V vs Ag/AgCl. Reverse pulse deposition was performed at -1.2 V vs Ag/AgCl during on-time and 0.25 V during the reverse pulse with an on-time of 450 ms and a duty cycle of 0.9. XRD was carried out in Bragg-Brentano configuration, the XRD graph can be found in the appendix (Appendix figure 7).

Removal of the photoresist

The photoresist was removed in MUEGGE Plasma R3T system. The stripping was carried out at 900 W in a 450 mTorr gaseous environment consisting of 1200 ppm O_2 , 15 ppm CF_4 and 5 ppm N_2 . The removal was done at 60°C. The samples were subjected to the plasma for a total duration of 2 h with periodical intermissions to observe the photoresist removal rate.

Model parameter acquisition

Cyclic voltammetry was performed in order to determine the deposition potential and the reverse pulse potential (Appendix figure 4). The reduction of Ni_{2+} to Ni_0 takes place from -0.6 V to -1.4 V vs Ag/AgCl. A deposition potential of -1.2 V vs Ag/AgCl was chosen, due to the high deposition speed at this potential. The oxidation of the deposit occurs from potentials higher than -0.3 V. The reverse pulse potential was fixed at 0.25 V, well within the range of oxidation. The equilibrium potential of the system was determined to be -0.5 V vs Ag/AgCl. Linear sweep voltammetry was carried out at 0.05 V/s and Tafel analysis was used to investigate the kinetics of the system (Appendix figure 5). A 300 s long deposition at -1.2 V vs Ag/AgCl was carried out prior to the experiment to create sufficient deposit to ensure no mass limitation in the anodic part of the sweep. The exchange current density was determined to be 110 A/m². The charge transfer coefficient, α_c and α_a , were determined to be 0.5. These values are in agreement with literature.[136] A 120 s direct deposition on a pure ITO surface was carried out (Appendix

figure 6). The diffusion coefficient was calculated according to Heinze [141] The diffusion coefficient is $1.5 \times 10^{-9} \text{ m}^2/\text{s}$. This is in agreement with literature values.[142] The conductivity was measured with a Methrom 914 pH/conductometer and was determined to be 4.6 S/m .

5.1.3 Model architecture

COMSOL Multiphysics version 5.3 was used in combination with COMSOL's electrodeposition software to implement equation 3.2-3.11 into a 3D numerical framework. As the equations indicate, a tertiary current distribution model approach was chosen. Tertiary current distribution accounts for the influence of changes in concentration of the electrolyte constituents within the template, as was investigated by Tsai et al. [133] Only the Ni^{2+} -ions were incorporated in the model. The rest of the electrolyte constituents are neglected, and only their contribution to the electrolyte conductivity are accounted for. This greatly reduces the necessary calculation power and time. The simulation uses COMSOL's supporting electrolyte option, assuming the bulk of charge carrying species is non-electroactive and exceeds the concentration of the electroactive species. This is assumed to be true due to the large amount of boric acid, chloride and sulfamate related species present in the electrolyte. A two-scale simulation was built. A macroscopic simulation was implemented to monitor the electrolyte potential as well as the nickel concentration in the entire electrochemical cell. This data was used to determine boundary conditions and input parameters for the microscopic simulation.

Boundary Conditions

The working electrode potential is defined as a constant value of -1.2 V vs Ag/AgCl in direct deposition mode. The electrode potential in pulsed deposition is defined as a square shaped wave, where the deposition potential is defined as -1.2 V vs Ag/AgCl. and the reverse pulse is at 0.25 V vs Ag/AgCl. The counter electrode potential in the macroscopic model is set to -0.5 V vs Ag/AgCl. The area of the counter electrode is 50 times larger than the area of the working electrode. Therefore, it is assumed that the counter electrode does not undergo a significant change in potential during deposition. The electrolyte potential in the microscopic model is defined as a constant value close to the electrode potential. The electrolyte potential is taken from the macroscopic model for the direct deposition. For the pulse deposition, an average electrolyte potential is derived from the macroscopic model. Open boundaries are defined for the microscopic model, reflecting boundaries open to the bulk electrolyte. The concentration is defined on these boundaries as the initial nickel ion concentration. Furthermore, a symmetry boundary is used in the microscopic simulation. The geometrical description of the boundaries can be found in the following figures for the different geometries (figure 5.1a, 5.2a and 5.4a). All the input parameters can be found in the appendix (Appendix table 1).

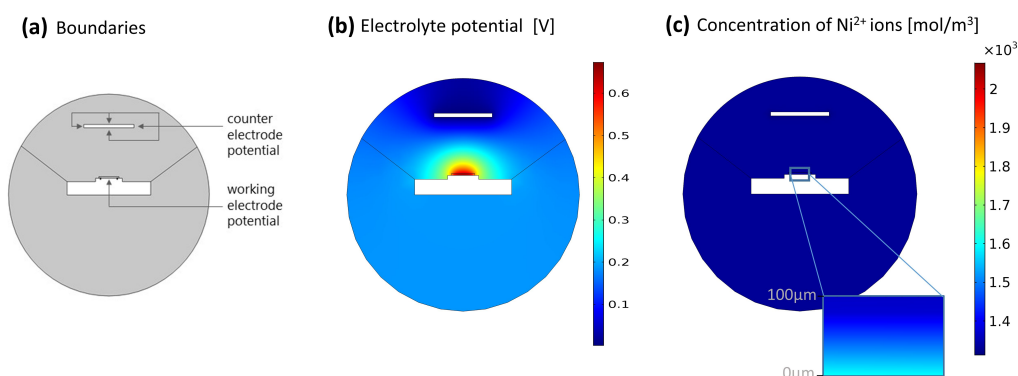


Figure 5.1 – Macroscopic 2D model of the electrochemical cell supplying boundary conditions to the microscopic model. a) model boundaries definitions, b) electrolyte potential and c) concentration of Ni^{2+} -ions in the cell.

5.1.4 Results and discussion

Verification of the simulation

The macroscopic model of the cell was used to simulate and export boundary conditions to the microscale model. The macroscopic model (figure 5.1a) supplies that the electrolyte potential deviates from the equilibrium close to the working electrode (figure 5.1b). Furthermore, the electrolyte potential deviation from equilibrium reaches far within the electrolyte due to the high conductivity of the electrolyte. The solution shows an increase in Ni^{2+} concentration close to the working electrode elevating the concentration to 1.5M Ni^{2+} close to the working electrode (figure 5.1c). In order to verify the simulation, arrays of 2D microelectrodes (figure 5.2) were produced. The template was purposely kept simple, leaving a square shaped electrode surface to examine 2D deposition. A 500s direct deposition at -1.2 V vs Ag/AgCl was simulated as well as experimentally performed in order to verify the deposition speed in the model (figure 5.2b). The SEM image of the deposit shows good agreement of the deposition speed, as well as the general shape of the deposit. The simulation shows a slight increase in deposition speed closer to the edges of the template, which were too small to verify experimentally. A 200 s pulsed electrodeposition carried out to verify the simulation deposition speed (figure 5.2c). Experimental comparison shows agreement between the simulation and the experiment. The growth rate were determined to be 3 $\mu\text{m}/\text{min}$ in direct deposition and 2.3 $\mu\text{m}/\text{min}$ in the pulsed electrodeposition in both experimental work and the simulation. More complex geometries can be too time consuming and difficult to model the deposition in its entirety, so that only periods of interest may be simulated. Therefore, the verification with microelectrode arrays offered a fast way to verify the accuracy of the model with simple templates. Furthermore, the use of 3D microprinted electrode arrays highlights the possibilities of creating custom electrode geometries with two- photon lithography, which offers possibilities for electrochemical analysis.

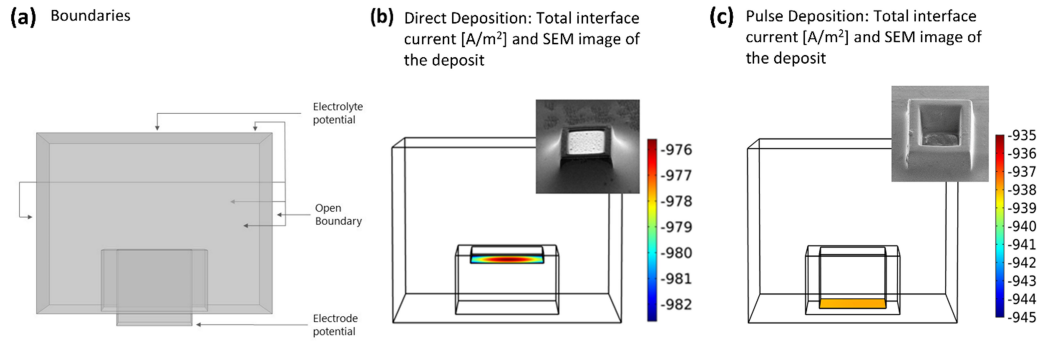


Figure 5.2 – 3D model verification experiments. A) Boundary conditions of the verification simulation experiment. B) 500s direct deposition at -1.2V vs Ag/AgCl: simulation and experiment in comparison. C) 200s reverse pulse deposition at -1.2V vs Ag/AgCl and 0.2V Ag/AgCl respectively, with a duty cycle of 0.9 and an on-time of 450ms. SEM-images taken at 50° angle.

Creation of an electrodeposited bridge-like structure

A bridge-like microstructure was electrodeposited. The structure consists of three cuboids connected with two smaller interconnects (5.3). The intended mechanical test is similar to a copper structure used by Pfetzing-Micklich [140]. The design faces many of the previously mentioned challenges to electrodeposit into 3D templates such as a large change in area with increasing deposition height, horizontal diffusion and migration in the template, and lateral bottleneck features. Furthermore, this structure allows us to design different templates and compare the electrodeposition by changes to the templates.

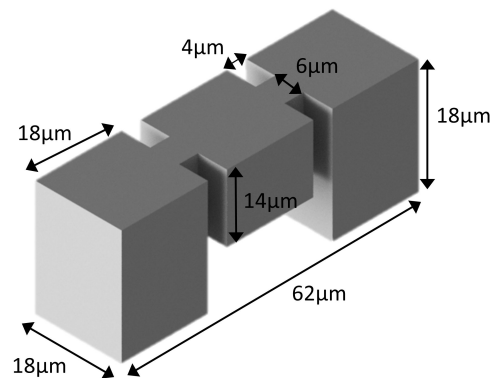


Figure 5.3 – Microshear test specimen design

Design of the template and electrodeposition of a bridge-like microcomponent

Two possible template designs (figure 5.4a and 5.4b) were investigated with the simulation and experimentally. Only periods of interest were simulated, due to restraints on time and calculating power. Furthermore, only half of the deposition was simulated by using the symmetry in the center through the center cube (figure 5.4). A completely open design (figure 5.4b) and a design with the top closed except above the middle cube (5.4a) were investigated. Due to the increased possibilities and accuracy of the negative resist process, it is possible to introduce small closing layers on top of the template, avoiding large-scale overgrowth. The shield on top of the outer cuboids forces electrolyte current distribution vectors through the narrow gap for the interconnects. The open template features a more homogenous electrolyte current density vectors. This causes the deposition in the side cuboids to be more homogenous for the open template than the shielded one (figure 5.4c and 5.4d). According to the simulation, the shielded template lowers the deposition rates in the initial stages of the deposition. The average current in the outer cuboids is 12% smaller in the shielded sample. During ongoing deposition, the total current disparity between the open template and shielded template increases (figure 5.5a and 5.5b). The homogeneity of the deposition in the outer cuboids decreases with ongoing deposition in both templates (figure 5.4c and 5.4d). The deposition in the open template continues to grow vertically in the outer cuboids and starts lateral growth into the center cuboid. The current density is increased in the outer cuboids compared to the center (figure 5.4d). The deposition reaches the top of the template with no fully conjoined connection in the center cube. The shielded sample on the other hand, prevents overgrowth at the sides and forces electrodeposition within the middle of the structure (figure 5.4c). The electrodeposition slows down towards the outer sides and increases deposition towards the center of the template. The deposits finally disconnects electrolyte on top of the outer cuboids from the bulk electrolyte. This effectively stops deposition in the outer cuboids prematurely. The simulation shows that the nickel concentration within the template exceeds the electrolyte nickel concentration within both templates. This indicates that deposition takes place under kinetic limitations.

Pulsed electrodeposition can be introduced, to overcome the issue of non-filled center or side cuboids. The introduction of an off pulse is not sufficient, as the deposition is not mass transfer limited in both cases. The introduction of a reverse pulse is beneficial. Dissolving preferentially deposited material is a feasible way to reach higher filling rates. The growth of the side cuboids is favoured slightly in the open template with a current density of averaging 103% (Figure Figure 5.5b) compared to the center. The dissolution of the deposit during the reverse pulse favours the outer cuboids as well, on average by 106% (Figure Figure 5.5d). In conclusion, anodic pulses could increase the filling rate within the open template. The growth in the shielded template is favoured in the center cube. The current density is less evenly distributed in the shielded template compared to the open template. On average, the current density in the outer cuboids amounts only to 81% compared to the center (Figure Figure 5.5a). The reverse pulse shows current density distribution akin to the cathodic pulse with increased inhomogeneity. The current density in the outer cuboids averages 72% of the current density

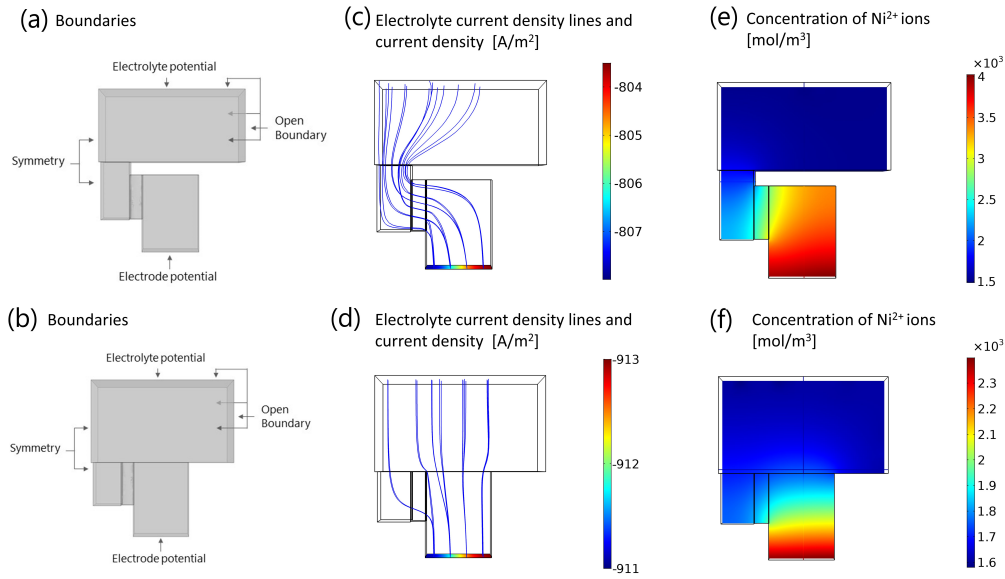


Figure 5.4 – a) Simulation boundaries of microscopic 3D simulation of the shielded template. b) Simulation boundaries of microscopic 3D simulation of the open template. c) Electrolyte current density vectors and current density distribution in the shielded template during the initial stage of the deposition. d) Electrolyte current density vectors and current density distribution in the open template during the initial stage of the deposition. e) Ni²⁺ concentration in the electrolyte during the initial stages of the deposition in the shielded template. f) Ni²⁺ concentration in the electrolyte during the initial stages of the deposition in the open templates

compared to the center cuboid (Figure 5.5c). This effectively stalls the growth in the center and increases the filling rate in the outer cuboids before closing the template off. Overall, the simulated current density of the reverse pulses are larger than the cathodic pulse, indicating high duty cycles already influence the deposition. Both template could be used to deposit structures. Finally, the shielded template was chosen to avoid the amount of FIB-milling necessary to prepare the sample for mechanical testing. Early work in this project using open template in positive tone AZ9260 resist showed large homogenous overgrowth on the entire sample. Due to the height constraints with positive resist, the sample was also smaller than originally intended.

Deposition was carried out in reverse pulse deposition mode with an on-time of 450 ms and a duty cycle of 90%. The deposits shown in figure 5.6 show well-defined structures, with a patterned surface caused by the templates surfaces roughness. The bases are widened, most likely due to forcing out of the air during low-pressure electrolyte infiltration, detaching the templates slightly from the substrate, opening space for the electrolyte to enter. The top of the outer cuboids were not completely filled as described previously. These cavities show that 2 μm high space was not electrodeposited. The connections between the cuboids show therefore an upward inclination to the center. Otherwise, the bridge-like structure exhibits

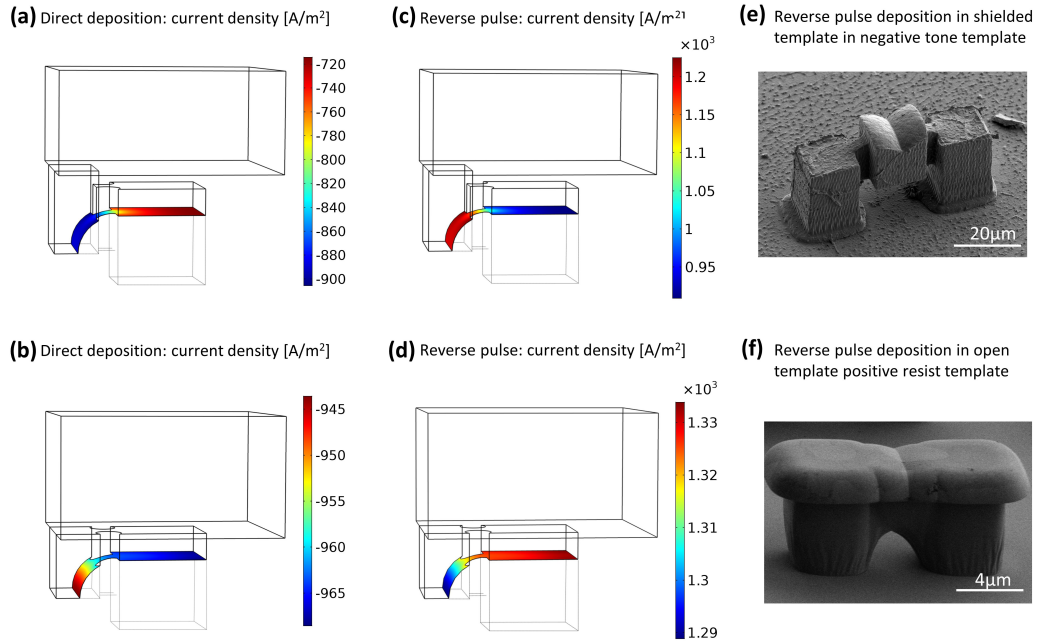


Figure 5.5 – a) Current density distribution during direct deposition at -1.2 V Ag/AgCl in the shielded template. b) Current density distribution during direct deposition at -1.2 V versus Ag/AgCl in the open template. c) Current density distribution during a reverse pulse at 0.25 V versus Ag/AgCl in the shielded template. d) Current density distribution during a reverse pulse at 0.25 V versus Ag/AgCl in the open template. e) SEM image of a structure deposited in the shielded template using reverse pulse deposition with a duty cycle of 0.9 and an on-time of 450 ms. f) SEM image of structure deposited in a smaller scale, open template made with AZ9260 positive photoresist.

sharp angles, dimensions close to the intended design except for the top. Furthermore, the structures are reproducible and homogenous within the array. It is therefore reasonable to conclude that the filling of angles of 90° or less is difficult to achieve.

Microstructure

A cross-section was cut with FIB and a secondary electron image was acquired, with electrons generated by the ion beam. The resulting contrast shows the granular structure within the deposited bridge. The deposit exhibits no porosity. As expected, nickel grains are elongated in the growth direction. Initial growth produces a fine-grained structure with a gradual enlargement of the grain size in height. Radial growth begins at the intersection with the horizontal part of the bridge toward the bridge center. Both growth fronts meet in the middle of the template. Gradually, the radial growth in the center cube converts to a purely vertical growth. The crystal size enlarges with increasing height in the outer cubes and decreases towards the mid-section of the bridge (figure 5.7b). Rashidi et al have shown that current

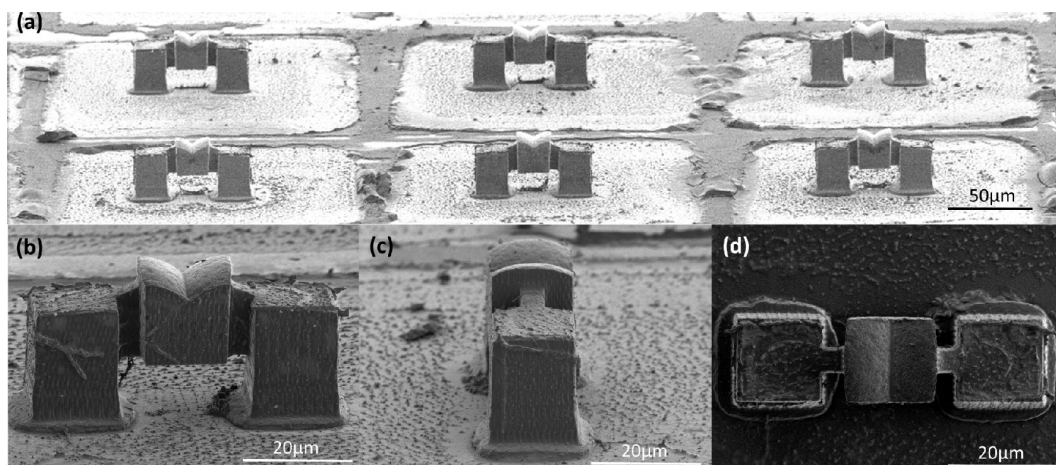


Figure 5.6 – SEM images of deposited structures after resist removal: a) Overview of an array of structures, b) front view at 71°, c) side view at 71°, and d) top view.

density decrease can lead to an increase in grain size.[142] The current density decreases in the outer cuboids during the deposition with increasing height from 800 A/m² to 720 A/m², the center cuboid deposit at an average current density of 900 A/m² (figure 5.5b). This correlates roughly to the visible changes in grain size (Figure 5.7b). Despite this correlation, it should be noted that also other aspects such as local saccharine content also influence the grain size in the deposit.[76]

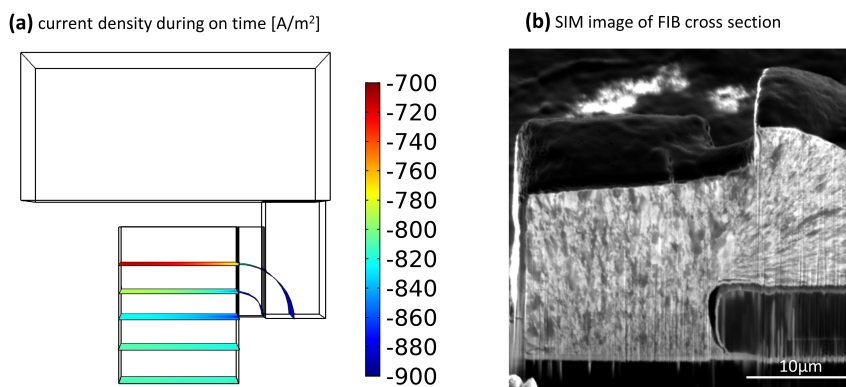


Figure 5.7 – a) Local current density at different stages of the deposition. b) Secondary electron image generated with FIB after the cutting of the cross-section, revealing the microstructure within the deposited microcomponent.

5.1.5 Conclusion

In summary, a 3D electrodeposition simulation of nickel sulfamate was created and verified. The simulation was used to investigate electrodeposition behaviour and changes in

said process with different template designs. Two designs were investigated, and the current density at different stages of the deposition was simulated. The introduction of horizontal photoresist showed major influence on the local current density distribution as well as the average current density. Due to the simulation, reverse pulse electrodeposition was used to increase the filling ratio. Structures for micromechanical testing were produced, exhibiting the desired shape and dimensions with well-defined angles. A FIB cross-section revealed a cavity-free deposit. SIM imaging of the cross-section revealed inhomogeneous grain size distribution within the structure correlating to the simulations current density. Our research shows that the combination of two-photon lithography in negative tone photoresist and electrodeposition can be used to create intricate and accurate 3D microarchitectures. We display that 3D electrodeposition simulation is a viable tool to optimize the template design and the electrodeposition conditions prior to the experimental work. Furthermore, the simulation proved advantageous to examine the influence of reverse pulses during deposition in complex templates. This opens the possibility in future to tailor pulses to the progress of the deposition within the template. Moreover, the influence of the template on the microstructure can be predicted with the simulation prior to the experiment, adding a further option in design space to template assisted electrodeposition architectures. In future, micromechanical testing of the samples will be performed.

5.2 Nanocrystalline nickel microlattices

Declaration of contribution

Patrik Schürch has created the 3D drawings, the templates and carried out the electrodeposition, while Rajaprakash Ramachandramoorthy did the mechanical investigation and assisted with the mechanical discussion. Johann Michler and Laetitia Philippe supervised the work.

5.2.1 Introduction and aims

Microlattices have recently garnered significant scientific attention [143] The combination of design, size scale, and materials allows us to create lightweight, high-strength structures with good energy absorbance. Ashby and Deshpande [144, 145, 146, 143, 147] described the design of so-called, cellular materials designs can be analyzed by maxwell stability criteria, m [143]

$$m = b - 3j + 6 \quad (5.1)$$

b is the number of struts and j is the number of frictionless joints. If m is less than zero, the structure is bending-dominated, if m is equal to zero, the structure can be described as self stressed and if m equals more than zero, the structure is stretching dominated. In general, it has been proven that stretching dominated structures outperform the bending dominated

designs. Further improvement can be made by replacing struts through sheet-like walls. While the design is of utmost importance, and often underappreciated fact is the quality of the microlattice material and the choice thereof, as well as the size scale. The material lays the foundation of the hardness and mechanical response that can be obtained. Metals and ceramics are dense but offer high strength while polymers and polymeric composites are relatively light but exhibit limited strength. Furthermore, the microstructure of the material can have an intrinsic effect on the mechanical properties. The feature resolution is crucial to the density and strut size that can be achieved in a lattice. To be able to profit from an extrinsic size effect, as it has been shown in pillars, where smaller is stronger, the resolution must be high enough to reach such a feature scale. The last, but crucial factor in lattice manufacture is the accuracy to the design and the quality of the material. To summarize, the ideal lattice combines the best quality material with an optimized microstructure to an optimized design with the optimum strut size.

In literature, a variety of microlattices can be found. Polymeric microlattice with oxide and metal coatings have shown the importance of design.[38, 148] Although able to boast a high strength at low density, the material shows poor energy absorbance. The energy absorbance can be assessed by the amount of stress able to retain after the yield point, until densification sets in, see figure 5.8. Lattices from metallic materials, such as lattices from Gu et al [56], have higher yield strength and better energy absorbance but at the cost of a higher density.

5.2.2 Methods

The inverse deposition method was used as previously described in chapter 4.2. The spin coat conditions were changed to yield a $38\mu\text{m}$ layer. After oxygen plasma cleaning and a dehydration bake, a two-step spin coat was performed, spin coating at 300 rpm for 5 s followed by a 1000 rpm spin coating for 60 s. This first step was followed by 60 s of waiting, a 60 s bake by 90°C and a 140 s bake at 110°C . The spin coat step was repeated and after 1 min of waiting baked at 90°C for 60 s and 240s at 110°C . After the illumination of the previously design structure, the photoresist was developed immediately after for 60 min in AK400/Water in a ratio of 1:5. The electrodeposition took place at the same parameters as previously described in chapter 4.2, but deposition time was increased to two hours. The mechanical testing of the structures was carried out with a standard assembly setup from ALEMNIS AG for micromechanical in situ testing. The setup was mounted into a TESCAN Lyra3 SEM. The compression tests were carried out under displacement control at different strain rates of 0.1, 0.01 to 0.001 per s.

5.2.3 Results and discussion

Nickel microlattices were produced with different angled design, the structures feature the previously explained top layer which allowed to place the illuminated structure into the film. The lattices produced showed limited height cells, due to the spin coat thickness. Furthermore,

no vertical struts could be electrodeposited, a body-centered cubic (BCC) structure was chosen. The samples showed that the structures could be produced at different angles without significant voids and a lack of filling. Due to the definition of lattices, these kinds of structures are not lattices, as the number of repetitive layers is not sufficient. These kinds of structures could, however, be excellent host structures for chemically active surfaces such as catalysts for instance.

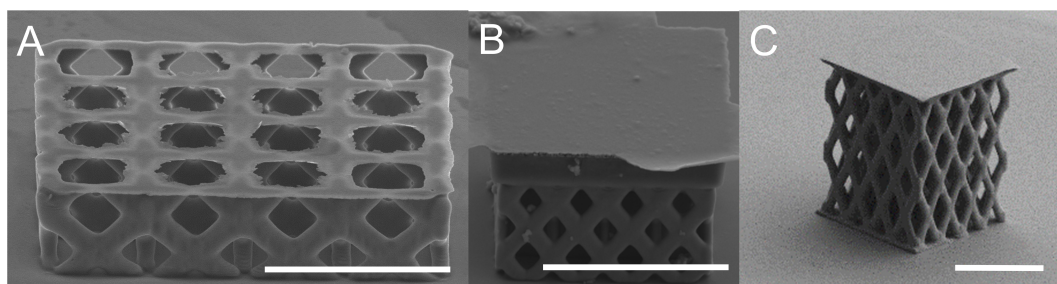


Figure 5.8 – Microlattices produced in this work: A) microlattices without any top layer B) microlattices including the top-layer C) True microlattice. Size indicator showing 25 μm

The next generation of structures that has been produced in this work was to investigate the mechanical behavior of such structure, therefore adding a top plate as has proven useful in chapter 5.2. A significant challenge is to produce lattices with a non-flawed microstructure. The previous structures were deformed into the plastic regime but the interest was in the elastic regime. Microlattices are usually deformed to failure. In this, initial test set, smaller layered structures proved to deform due to the ductility of the metal. After a stable recipe was developed for 38 μm thick photoresist layer, higher more layered structures were produced. While the original CAD files have a density of 7.3% of material compared to the entire volume, due to elongation of the lasers' focal point, the struts deviate and have an ellipsoidal shape with a diameter of 1.0 μm lateral and 1.8 μm vertically. From this follows that the relative density increases to 13.7%. This is, however, based upon the CAD file and to account for enlarging joints due to curvature between the struts a value of density of 15% will be assumed in further calculations.

The structures showed significant underplating at the top of the layers, otherwise, the lattices show a reasonable layering. The 45° degree angle structures were used for mechanical testing at different strain rates. The samples show an elastic deformation at the beginning. Remarkably, both lattices shown in figure 5.9a, show similar mechanical failure, in the middle of the lattice, though they were tested at different strain rates between 0.001 pe s and 0.1 per s . The lattice breaks mostly in a similar fashion as predicted by a simulation of a BCC structure simulated by Smith et al [149], see figure 5.10. The onset of breaking joints is visible in figure 5.9a, the failure occurs at the onset of the struts where the stress-concentration according to Smith et al is highest. This accordance with simulations as well as the remarkable strength for a lattice with a stability criterion of $M=-13$, suggest that the structure is comprised of nanocrystalline nickel without any significant porosity or grain size deviation. The lattices reported by Gu et al [56]

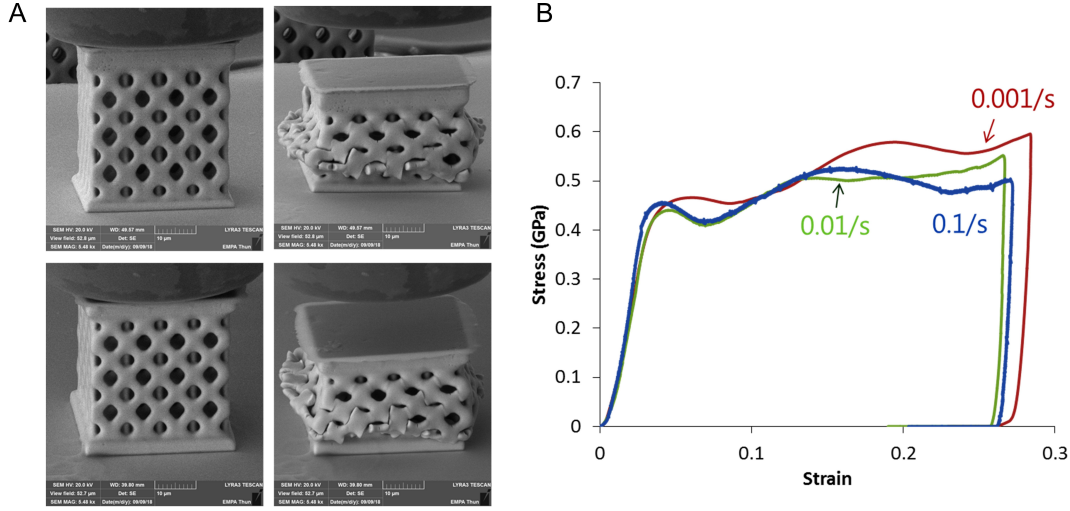


Figure 5.9 – Microlattices compression test: A) microlattice prior to test on the left and post compression on the right. B) Stress-Strain curve of three different microlattices tested at three different strain rates

are softer, even with their significantly more stable octet design. This is due to the significantly softer nature of single quasi-single crystalline copper compared to nanocrystalline nickel. Furthermore, considering equivalent stress simulations suggest that the lattices produced by Gu et al show some breakage along grain boundaries, while the single crystal beams stay intact. In the case of the nanocrystalline nickel lattices, the grain boundaries within the structure are so numerous, that they do not influence the failure occurrence. At the same time, the amount of grains and thickness of the struts, however also diminishes any extrinsic size effect. The metallic lattices produced showed excellent energy absorption properties. The lattices do not show a stress drop, but a steady stress level. The point of densification and the stress increase was not reached in the experiments presented here, due to the inherent maximum load limit on the load cell used for testing. However, as the densification stress is related to the density:[150]

$$\epsilon_D = 1.0 - 1.4\left(\frac{\rho}{\rho_s}\right) \quad (5.2)$$

with ϵ_D the densification strain and ρ the density of the lattices and ρ_s the density of the solid, the assumption that the densification strain would occur roughly 80% is most likely an overestimation, yet values up to 50% of strain could be reasonable. Whereas for instance the lattices put forward in copper would, according to calculations, densify already significantly earlier, at around 30%. These results suggest that the lattices presented here are amongst the most energy absorbent lattices in literature as the initial high yield strength and the high densification strain would allow for high energy absorbance. Although the yield stress could

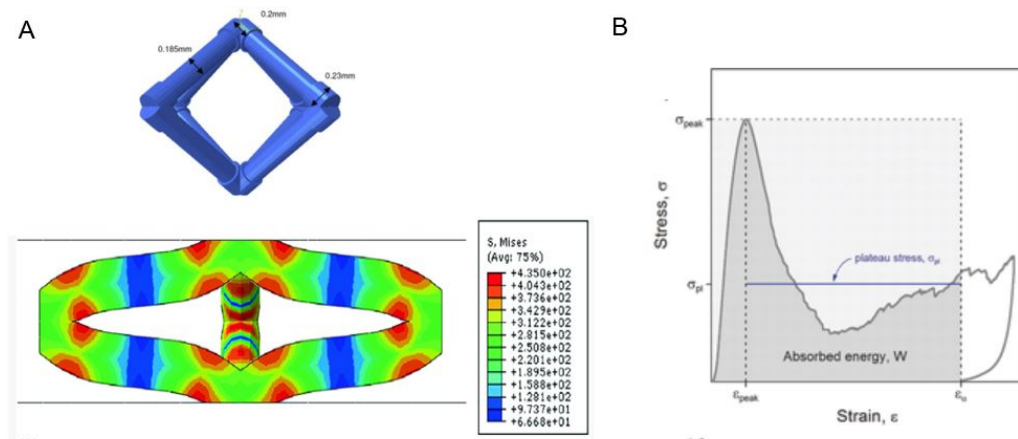


Figure 5.10 – A) Smith et al’s simulation of deformation of a BBC unit cell. Top; Unit cell, Bottom: Simulation of van Mises stress at 50% deformation[149] B) Energy absorbance of a microlattice, showing the yield point ϵ_{peak} , the constant stress level or plateau σ_{pl} and ϵ_a , as the value set as densification threshold.[38]

be enhanced through the design, octet structures would also reduce the onset of densification significantly.

In the Ashby plot in figure 5.11 the mechanical strength of the deposits is shown versus the density. Due to the architecture, the weight can be significantly reduced while a portion of the strength is retained. Compared to most other lattices in literature, fully metallic lattices are stronger, yet substantially denser. Amongst the metal lattices, the nickel lattices in this work show a high yield point at 429 MPa while also boasting a low relative density of 0.15. The metal lattices by Gu et al yielded at 330 MPa with a higher relative density of >0.7 . This comparison highlights that the choice of material is crucial for the strength and that nanocrystalline material is less impacted by the grain boundaries created by the fusion of two electrodeposition growth fronts.

5.2.4 Conclusion

The produced lattices showed excellent strength. No preferential failure in fused electrodeposition boundaries can be seen. Furthermore, the yield strength of the microlattice shown was remarkably high for lattices this size. As a conclusion, more lattices will need to be produced to recreate the test and create a larger amount of data. Initial results are extremely promising, considering the template design does not include horizontal struts and has a low stability criterion, yet shows performances comparable to other metallic octet lattices.

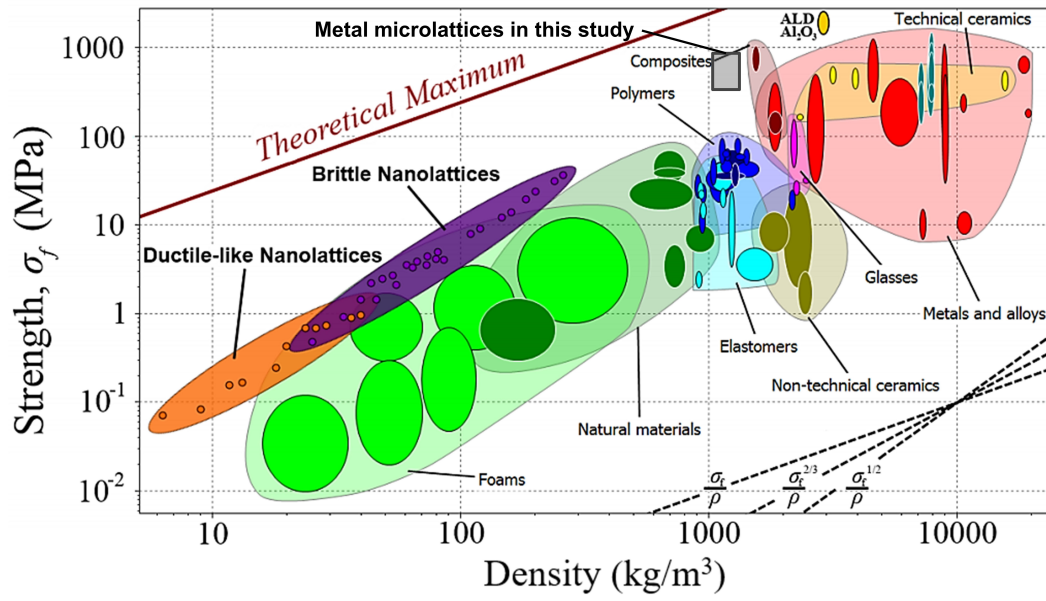


Figure 5.11 – Ashby plot showing strength versus density of various materials and microlattices, including the lattices from this work, in comparison.

6 Copper nickel electrodeposition

6.1 Nanocrystalline copper nickel deposition

Declaration of contribution

Cristina Manzano electrodeposited and polished the T-components and did the XRD and XRF analysis. Patrik Schürch provided the electrochemical simulation and the electrochemical analysis for it. Furthermore, he provided the 3D drawings of the t-component and the gear template, produced the gear template and the photoresist removal. Gerhard Bürki provided assistance with the SEM imaging and EDX. Johann Michler and Laetitia Philippe supervised the work.

This work has been published as "C. V. Manzano, P. Schürch, L. Petho, G. Burki, J. Michler, and L. Philippe, "High aspect ratio nanocrystalline CuNi t-structures and micro-gears: Synthesis, numerical modeling and characterization," *Journal of the Electrochemical Society*, vol. 166, no. 10, pp. E310–E316, 2019." This chapter includes figures of the aforementioned publication with permission from The Electrochemical Society.

6.1.1 Introduction and aims

In recent years, MEMS (micro-electro-mechanical-system) devices have received substantial attention for their different properties and possibilities, e.g. small volume, lightweight components in mechanical, electronic and magnetic devices, vital for industrial applications, such as telecommunication, aerospace, biomedicine, automobile, etc. LIGA (German acronym for Lithography, Electroplating and Moulding) is one of the foremost techniques [97] to obtain MEMS metallic alloys. It is a microfabrication process, in which structural material is electrodeposited with high-aspect ratios inside moulds. This allows obtaining thick samples, normally not possible to produce via electrodeposition on flat substrates, as well as free-standing structures. However, it is only possible to apply this technique to certain materials, such as Ni, [151] Cu [152] and Au [153]. Electrodeposition is an excellent growth method, which can be used at room temperature, provides fast deposition rates, is inexpensive and is

easily transferred to industry. Moreover, it allows for perfect control over the thickness and stoichiometry of various materials.

One of the most studied metals used to obtain high aspect-ratio materials, characterized by good mechanical and magnetic properties, is nickel. Normally, Ni is alloyed with other metals, such as W, [154] Fe, [155] Co, [63] Cu, [156] P, [157] etc., to tune its properties. The process becomes increasingly more complex when applying it to alloys. CuNi alloys have attracted a lot of interest, as they possess excellent tuneable mechanical and magnetic properties, as well as high corrosion resistance, superior to many other alloys. Cu and Cu-rich alloys are a popular choice in many metallurgical and technological applications, due to their high electrical and thermal conductivities, which favors their use in microelectronic devices and integrated circuits. Additionally, they are softer and more ductile than many comparable alloys. In contrast, Ni-rich CuNi alloys are mostly used as ferromagnetic materials.[156] For this reason, studying the fabrication and properties of NiCu alloys with different nickel and copper ratios is particularly interesting. The Constantan ($\text{Cu}_{55}\text{Ni}_{45}$) alloy is non-magnetic and exhibits good mechanical properties.[158] These properties make copper-nickel alloys exceptionally good candidates for MEMS applications, such as resistive [159] and thermoelectric devices, [160] magnetic sensors, actuators, non-magnetic gaps in recording write heads, conductor wires, etc.

CuNi are normal co-deposition type alloys, [161] which can be electrodeposited using different electrolytes, one of the most common being citrate solutions. Complexing agents, such as citrate, decrease the reduction potential gap between two metal reactions (Cu and Ni), allowing to obtain a wide range of different Cu and Ni alloy concentrations. Moreover, the citrate solution allows reaching high current efficiencies for different compositions and acts as a brightening agent.[162] As reported in literature, the mechanical properties of CuNi alloys can be improved by producing nanocrystalline materials, rather than fine-grained.[163] The ability to control the grain size and composition of these alloys allows tuning both chemical and physical properties and, in turn, studying different alloy applications.

Few studies on CuNi electrodeposition simulation models are found in literature. In 1988, Ying et al.[161, 164] proposed a mathematical model estimating the mass transfer and kinetic parameters for CuNi alloys using a citrate-based solution. In 2005, Rode et al.[165] obtained current efficiencies for various Ni concentrations at different pH, also using citrate solutions. All models developed until now are 1D. As the development of electrodeposition has expanded to 2D and 3D materials, it is necessary to extend these models also to 3D. A similar 3D simulation for nanocrystalline nickel electrodeposition was previously developed in our group to control deposition into complex 3D templates. Expanding on this work, the more complex CuNi electrochemical system was simulated using a similar multiscale approach and mathematical framework.[156]

In literature, different studies on obtaining electrodeposited fine-grained CuNi films [72, 166] and nanocrystalline CuNi films [64] are described, where CuNi nanopillars have already been

manufactured using electron beam lithography.[167] Mechanical and magnetic properties of electrodeposited CuNi films on various substrates [150, 162, 167] and thermoelectric properties of electrodeposited CuNi films on Si [168] have been investigated.

Although this process is an attractive method, there are many challenges that must be addressed. The main issues involve establishing the compatibility between the electrodeposition electrolyte and lithography photoresist and finding a substitute for the Ni sulfamate bath, normally used for Ni micro-components for avoiding stresses in the deposit (possible Cu precipitation). Other challenges concern obtaining high aspect ratio without internal stresses, good filling inside the moulds, current density homogeneity in the desired geometry, area and during long deposition times, and avoiding hydrogen evolution that could cause delamination and/or cracks. To face these challenges, pulsed electrodeposition has to be used and correct pulse plating parameters have to be determined. Until now, the NiCu micro-components (MEMS) fabrication was not investigated, due to the complexity of combining lithography and electrodeposition. Additionally, there are no previous studies on developing 3D models for describing these kinds of CuNi microarchitectures.

This work is focused on investigating the electrodeposition parameters for obtaining nanocrystalline copper nickel alloys using UV-LIGA while controlling the composition and thickness (between 12–35 μm), using citrate solution. Based on these experiments, a 3D model was developed using COMSOL. The experimental and simulation results were compared to determine the accuracy of the 3D model with respect to composition, thickness and growth rate. This study opens a new perspective on the electrodeposition of new architectures, applicable to a wide range of areas, such as MEMS, NEMS, thermoelectric devices, magnetic, actuators, non-magnetic gap in recording write heads, conductor wires, sensors, etc. in order to improve their properties.

6.1.2 Methods

Fabrication of LIGA templates by UV-Lithography and two-photon lithography

The fabrication of LIGA templates via UV-Lithography was performed using <100> orientation single crystal Si wafers. Alliance-Concept DP 650 DC magnetron sputtering was used to deposit 5 nm of Cr and 100 nm of Au, to enable electrodeposition inside the moulds. High viscosity SU-8 (GM 1075, Gersteltec Sarl) was spin coated and the desired pattern was exposed using a Karl Suss MA6 contact aligner with a 365 nm exposure light source and the polymer was irradiated with a 8 mW/cm² intensity. Next, post-exposure bake was performed, followed by immersion in PGMEA (99.5%, Sigma Aldrich) to dissolve the unexposed SU-8, after which hard bake was applied to further enhance cross-linking.

A © Nanoscribe GMBH Professional GT was used to create templates for the micro-gears. The structure was created using a 25x magnification objective in a IP-S photoresist on to a Solaronix TCO10-10 substrate. Using the Nanoscribe Software “Describe”, the 3D-design was

sliced and hatched and only the contour and support structure was illuminated at 15mW with a laser speed of 10000 $\mu\text{m/s}$. Subsequently, the specimen was developed in PGMEA for 20 minutes and cleaned in 2-propanol (98%, Sigma-Aldrich) for 15 minutes. The structure was then illuminated again under a UV light source for 10 minutes to polymerize the photoresist trapped between the contour and support.

Electrodeposition of CuNi T-structures and micro-gear

CuNi T-structures and micro-gears were electrodeposited in a three electrode vertical electrochemical cell, where the working electrode was the UV-Liga mould, the counter electrode was a Pt mesh and the reference electrode was Ag/AgCl. The electrodeposition process was carried out by means of a potentiostat-galvanostat (Eco Chemie, Model AUT302N), and an electrochemical cell with a double-jacket cell to control the electrodeposition temperature. The working temperature was $45 \pm 1^\circ\text{C}$. The electrolyte used to perform the electrodeposition was an aqueous solution containing 0.3 M $\text{NiSO}_4 \cdot 6\text{H}_2\text{O}$ (98%, Sigma Aldrich), 0.08 $\text{CuSO}_4 \cdot 5\text{H}_2\text{O}$ (99%, Sigma Aldrich), 0.2 M $\text{C}_6\text{H}_5\text{Na}_3\text{O}_7 \cdot 2\text{H}_2\text{O}$ (99%, Sigma Aldrich), 0.7 mM $\text{C}_{12}\text{H}_{25}\text{NaO}_4\text{S}$ (97%, Fluka), 10.9 mM $\text{C}_7\text{H}_5\text{NO}_3\text{S}$ (99%, Fluka). Sodium citrate ($\text{C}_6\text{H}_5\text{Na}_3\text{O}_7 \cdot 2\text{H}_2\text{O}$) was used as the complexing agent, saccharine ($\text{C}_7\text{H}_5\text{NO}_3\text{S}$) as the refinement agent, to decrease the grain size of the alloy, and sodium dodecylsulfate ($\text{C}_{12}\text{H}_{25}\text{NaO}_4\text{S}$), abbreviated SDS, as the wetting agent.[163] The pH of the solution was 6 to avoid the precipitation of copper during electrodeposition.[72]

One of the largest CuNi MEMS production challenges is to control the internal stress within the T-structure and micro-gear. The internal stress can be controlled by adjusting the electrodeposition temperature, saccharine concentration and by using pulsed electrodeposition. A current thief and pulsed galvanostatic deposition were utilized to obtain parallel current lines on the deposit. The use of a current thief also provides perfect control over the thickness and composition inside all the T-structures and micro-gears.

Pulsed galvanostatic deposition was carried out between a certain current density and zero current density. Different electrodeposition parameters (ton, toff, temperature, additives) were studied to control deposit internal stresses. Three temperatures were used to control the internal stress of the deposits (40, 45 and 50°C). The most common additive used to obtain nanostructured deposited is saccharine. The addition of saccharine to the electrolyte reduces the crystallite size, improving the deposits' mechanical properties. Moreover, it affects the internal stress of the deposits during electrodeposition inside UV-LIGA moulds. Three saccharine concentrations were studied (0.2, 1 and 2 g/L), during which no alloy composition changes occurred. Different T-structures were electrodeposited by applying different current densities, i.e. -35 mA/cm^2 , -60 mA/cm^2 and -90 mA/cm^2 for the duration of 15 h, 12 h and 2 h, respectively.

After the electrodeposition of the CuNi T-structures, the films were polished to obtain a mirror surface using 1200 and 2500 papers, and different sized alumina powders (6 μm , 1 μm , 0.3 μm

and 0.05 μm) from Buehler. Additionally, 0.04 μm SiO_2 was used to avoid copper oxidation after polishing. In order to obtain free standing T-structures, the Si, Cr and Au substrates were removed using 2 M KOH (85%, Sigma Aldrich) at 50°C overnight, 0.25 M KMnO_4 (99%, Sigma Aldrich) and 0.5 M NaOH (97%, Fluka) at room temperature for a few seconds and Au etchant (Sigma Aldrich, Ni compatible) for a few seconds, respectively.

The deposition of CuNi into the two-photon lithography templates was performed. The templates were treated prior to electrodeposition with 100W oxygen plasma for 1 minute. A 10mm² sized area was used as current thief on the ITO, the photoresist was removed after the deposition in a MUEGGE R3T in a 450 W plasma at 60°C with 450 mTorr pressure and 925 sccm O_2 , 120sccm CF_4 and 50 sccm N_2 . After the plasma process, the sample was pressed onto a carbon tape and the freestanding micro-gear was obtained.

Structural, compositional and morphological characterization of CuNi T-structures and micro-gear

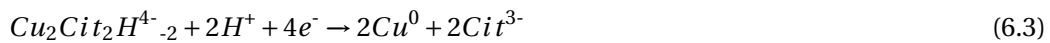
Structural characterization of the nanocrystalline CuNi was carried out using high resolution X-ray diffraction (XRD). The measurements were performed using a Bruker D8 Discovery diffractometer system in the Bragg-Brentano configuration with $\text{CuK}\alpha$ radiation. T-structure and micro-gear chemical composition analysis was performed using an X-ray fluorescence (XRF) system from Fisherscope X-ray XDV. Cross-section morphological characterization of T-structures and micro-gear was carried out via a Lyra dual-beam SEM-FIB (scanning electron microscopy-focused ion beam) instrument (TESCAN) with 30 kV accelerating voltage. Energy-dispersive X-ray spectroscopy (EDX) was used to study composition uniformity along the cross-section of the T-structures and micro-gears (TESCAN, 30 kV accelerating voltage).

3D nickel-copper simulation

A tertiary current distribution 3D finite element model of nickel-copper pulse deposition was created with COMSOL Multiphysics and the COMSOL electrodeposition module.

The simulation includes only electroactive species, additives and supporting electrolyte are incorporated by including the electrolyte conductivity, which was measured with a conductometer. Due to the importance of pulse electrodeposition in CuNi preparation, the simulation includes pulse plating. The pulse parameters used for deposition simulation are the parameters determined to yield CuNi films with minimized internal stress. They can be found in the following section.

A simplified set of chemical equations was created using the following four reactions:



In the simulation it is assumed that nickel can be deposited from complexed $NiCit^-$ and Ni^{2+} ions, whereas copper can only be deposited from the copper citrate dimer complex. The hydrogen evolution reaction (HER) is included as a parasitic reaction without the addition of the H^+ concentration. This allows for calculations with large applied current density boundary conditions on the working electrode.

The amount of electroactive constituents that are being included in the simulation, $Cu_2Cit_2H^{4-}_{-2}$, $NiCit^-$ and Ni^{2+} , were determined analogous to Ying et al.[161] The calculated electrolyte composition can be found in the appendix (Appendix table 4. The prevalent copper species at pH = 6, is a twice deprotonated copper citrate dimer complex, $Cu_2Cit_2H^{4-}_{-2}$, as reported by Rode et al.[16] Non-complexed and copper citrate monomer complexes are less prevalent and, therefore, excluded. Mixed metal complexes, most notably $CuNiCit_2H^{4-}_{-2}$, are, according to Rode et al.[65], not present at pH = 6 and can also be neglected. The nickel ions are present in the solution partially complexed to $NiCit^-$ and as free Ni^{2+} -ions, in a ratio of 2:3. Both contribute to the total amount of nickel being deposited and, hence, are accounted for in the simulation.

Baths containing the calculated amount of each species were produced using the above-mentioned chemicals. These were used to determine the diffusion coefficients with a rotating disc electrode setup and subsequent Koutecky-Levis plot analysis for each respective solution. Exchange current densities, as well as the respective Tafel slopes were obtained for each reaction. These parameters were subsequently used as simulation starting points and were adjusted to account for possible interferences. The deposition parameters can be found in Table 6.2.

This mathematical framework was used already to a previous study by our group concerning nanocrystalline pulsed nickel electrodeposition simulation.[169] The boundary and domain

6.1. Nanocrystalline copper nickel deposition

Table 6.1 – Parameters for the CuNi simulation

Parameter	Symbol	Units	Value
Initial concentration $\text{Cu}_2\text{Cit}_2\text{H}_2^{4-}$	cCopperCitrate	mol/m^3	36
Initial concentration NiCit^-	cNickelCitrate	mol/m^3	120
Initial concentration Ni^{2+}	cNickel	mol/m^3	180
Temperature	T	K	318.15
Relative system equilibrium vs Ag/AgCl	Eeq	V	-0.003
Charge $\text{Cu}_2\text{Cit}_2\text{H}_2^{4-}$	zCopperCitrate	[1]	-4
Charge NiCit^-	zNickelCitrate	[1]	-1
Charge Ni^{2+}	zNickel	[1]	2
Diffusion Coefficient $\text{Cu}_2\text{Cit}_2\text{H}_2^{4-}$	DCopperCitrate	m^2/s	$4.2 \cdot 10^{-12}$
Diffusion Coefficient NiCit^-	DNickelCitrate	m^2/s	$2.1 \cdot 10^{-9}$
Diffusion Coefficient Ni^{2+}	DNickel	m^2/s	$2.0 \cdot 10^{-9}$
Exchange current density Copper deposition	I_0 , CopperCitrate	A/m^2	0.0275
Exchange current density Nickel deposition form NiCit^-	I_0 , NickelCitrate	A/m^2	0.015
Exchange current density Nickel Depistion from Ni^{2+}	I_0 , Nickel	A/m^2	1.6
Exchange current density Hydrogen evolution reaction	I_0 , HER	A/m^2	2
Tafel slope Copper deposition	ACopperCitrate	mV	-105
Tafel slope Nickel deposition form NiCit^-	ANickelCitrate	mV	-53
Tafel slope Nickel deposition from Ni^{2+}	ANickel	mV	-52
Tafel Slope Hydrogen evolution reaction	AHER	mV	-118
Density Nickel	ρ_{Ni}	kg/m^3	8910
Density Copper	ρ_{Cu}	kg/m^3	8920
Molar mass Nickel	MNi	Kg/mol	0.058
Molar mass Copper	MCu	Kg/mol	0.063
Electrolyte Potential at 35 mA/cm^2	$\Phi_{\text{l,bnd}}$	V	-1.09
Electrolyte Potential at 60 mA/cm^2	$\Phi_{\text{l,bnd}}$	V	-1.4
Electrolyte Potential at 90 mA/cm^2	$\Phi_{\text{l,bnd}}$	V	-1.9

conditions for the simulation are given for the T-components here and for the micro-gear in the appendix (Appendix figure 9).

The patterned surface is the working electrode onto which the alloy is deposited. This is opposed by a set electrolyte potential. The entire volume of the simulation is used to represent the electrolyte and every boundary except the working electrode is used as an open boundary through which the electrolyte is replenished.

The model was built in a two-scale approach, with a macroscopic 2D simulation of the electrochemical cell supplying electrolyte potential to the microscale 3D simulation. This approach is analogous to a previous study conducted by our group concerning nanocrystalline pulsed nickel electrodeposition simulation.[169] It allows having a microscale simulation to take in account the shape of the lithography template on the working electrode while simultaneously considering the influence of the electrochemical cell geometry on the deposition.

6.1.3 Results and discussion

Electrodeposition of CuNi T-structures

Linear voltammetry was performed between the OCP (open circuit potential) and -2 V vs. Ag/AgCl to obtain CuNi T-structures with different Ni-Cu compositions (see figure 6.2). It can be seen that Cu deposition starts close to OCP and Ni deposition occurs at approx. -0.46 V and -1.18 V, respectively. CuNi alloys can be produced within this reduction potential range. Optical images of T-structures inside the moulds and a single T-structure can be seen on figures 6.1b and 6.1c, respectively.

The applied current density allowed controlling the chemical composition. The functional t_{on} and t_{off} values for pulsed electrodeposition were found to be 0.3 s and 3 s, respectively. It was determined that the temperature does not influence the composition of the alloys and at 45°C it is possible to obtain stress-free deposits. Functional results were obtained with the addition of 2 g/L saccharine to the electrolyte. Three T-structures were electrodeposited by applying different current densities, i.e. -35 mA/cm², -60 mA/cm² and -90 mA/cm² for the duration of 15 h, 12 h and 2 h, respectively. These current densities were defined used only the active area of the recessed through the mask.

XRD measurements were performed to determine the crystallographic structure and crystalline size of the alloys. Figure 6.3 shows the X-ray diffractograms of the T-structures grown at a constant current density deposition. Different peaks are seen, possibly associated to the substrate components: Au (JCPDS 040784) and Si (JCPDS 27-1402), along with others corresponding to CuNi (JCPDS 09-0205). All components exhibit three diffraction peaks, (111), (200) and (220).

Harris texture analysis [170] was performed to quantitatively obtain a degree of preferred

6.1. Nanocrystalline copper nickel deposition

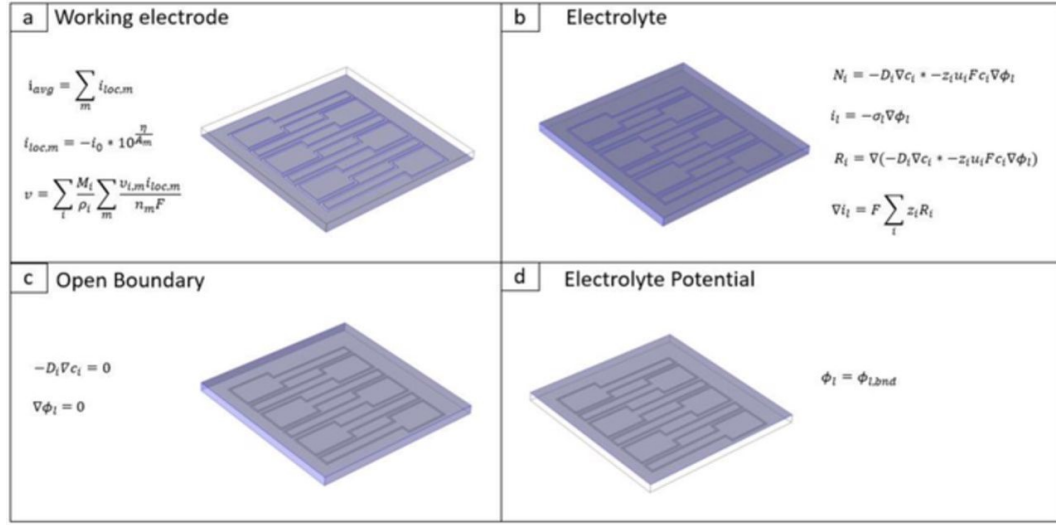


Figure 6.1 – All the parameters found in these equations not mentioned here can be found in Table 6.1. Working electrode boundary conditions (a): i_{avg} , defined current density, $i_{loc,m}$ local current for reaction m , η is the overpotential at the working electrode, v the velocity of growth at the electrode, n_m is the number of electrons transferred in the reaction m . Electrolyte domain conditions (B): N_i , c_i , z_i , u_i , is the flux respectively the concentration, charge and mobility of the ions i , and l is the local electrode potential. i_i is the local current density vector, R_i the total amount of ions. Open boundary conditions (c). Electrolyte boundary conditions (d).

orientation. The equation of the texture coefficient is:

$$TC_{(hkl)} = \frac{\frac{I_{(hkl)}}{I_{(hkl)}^0}}{\frac{1}{N} \sum \frac{I_{(hkl)}}{I_{(hkl)}^0}} \quad (6.5)$$

where: $I(hkl)$ and $I_0(hkl)$ – intensity of a generic peak observed in the experimental XRD and the literature value from the data base (JCPDS), respectively and N - number of reflection considered in the analysis. The standard deviation (δ) indicates the deviation intensity of the experimental XRD from published values of JCPDS and is calculated as:

$$\rho = \sqrt{\frac{\sum (TC_{(hkl)} - 1)^2}{N}} \quad (6.6)$$

The values of the texture coefficient and its standard deviation are shown in Table 6.2.

According to the texture coefficients, the T-structures with 65 at% and 57 at% of Cu are grown along the (111) and (200) diffraction peaks, respectively. However, the T-structure with 43 at% of Cu is oriented along the (111) diffraction peak.

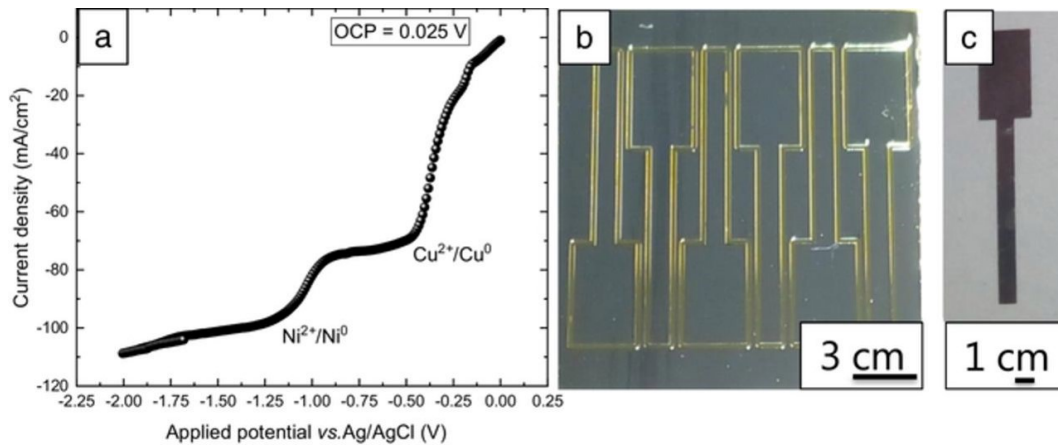


Figure 6.2 – (a) Linear voltammogram between the OCP (open circuit potential) and -2.25 V vs. Ag/AgCl, (b) optical images of T-structures inside the moulds and (c) optical images of a single T-structure.

Table 6.2 – Texture coefficients and standard deviations

Composition	Peak (hkl)	Intensity XRD	Intensity JCPDS	Texture coefficient (TC(hkl))	Standard deviation(σ)	FWHM (111)	Crystallite size (nm)
Cu _{0.65} Ni _{0.35}	111	206	100	1.1815	0.0651	0.432	19.9
	200	78	45	0.9979			
	220	33	23	0.8206			
Cu _{0.57} Ni _{0.43}	111	175	100	1.1371	0.05358	0.447	19.3
	200	72	45	1.0441			
	220	29	23	0.8188			
Cu _{0.43} Ni _{0.57}	111	215	100	1.4681	0.33281	0.471	18.3
	200	53	45	0.8111			
	220	24	23	0.7208			

In order to determine whether the CuNi is nanocrystalline, the crystallite size in the (111) diffraction peak was calculated using the Debye-Scherer equation:

$$D = 0.9\lambda\beta\cos\theta \quad (6.7)$$

where: D – crystallite size, λ – radiation wavelength, β – broadening of full width half maximum (FWHM) of the intense peak and Θ – Bragg angle. As is shown in Table 6.2, the crystallite size was found to be 19.9, 19.3 and 18.3 nm for Cu_{0.65}Ni_{0.35}, Cu_{0.57}Ni_{0.43} and Cu_{0.43}Ni_{0.57}, respectively. It was observed that the crystallite size slightly increases with the increase in copper.

The chemical composition was studied using XRF, where the T-structures grown at a current density of -35, -60 and -90 mA/cm² possess compositions of Cu_{0.65}Ni_{0.35}, Cu_{0.57}Ni_{0.43} and Cu_{0.43}Ni_{0.57}, respectively.

Cross sections of the deposits were made to investigate the samples morphology. As is shown in figure 6.4, Cu_{0.65}Ni_{0.35} and Cu_{0.57}Ni_{0.43} exhibit a granular morphology, the grain size increases with the increase in copper contents (Cu_{0.65}Ni_{0.35}). The morphology of Cu_{0.43}Ni_{0.57} is columnar, typical for the growth of Ni. When the Cu contents exceed 50 at%, the morphology

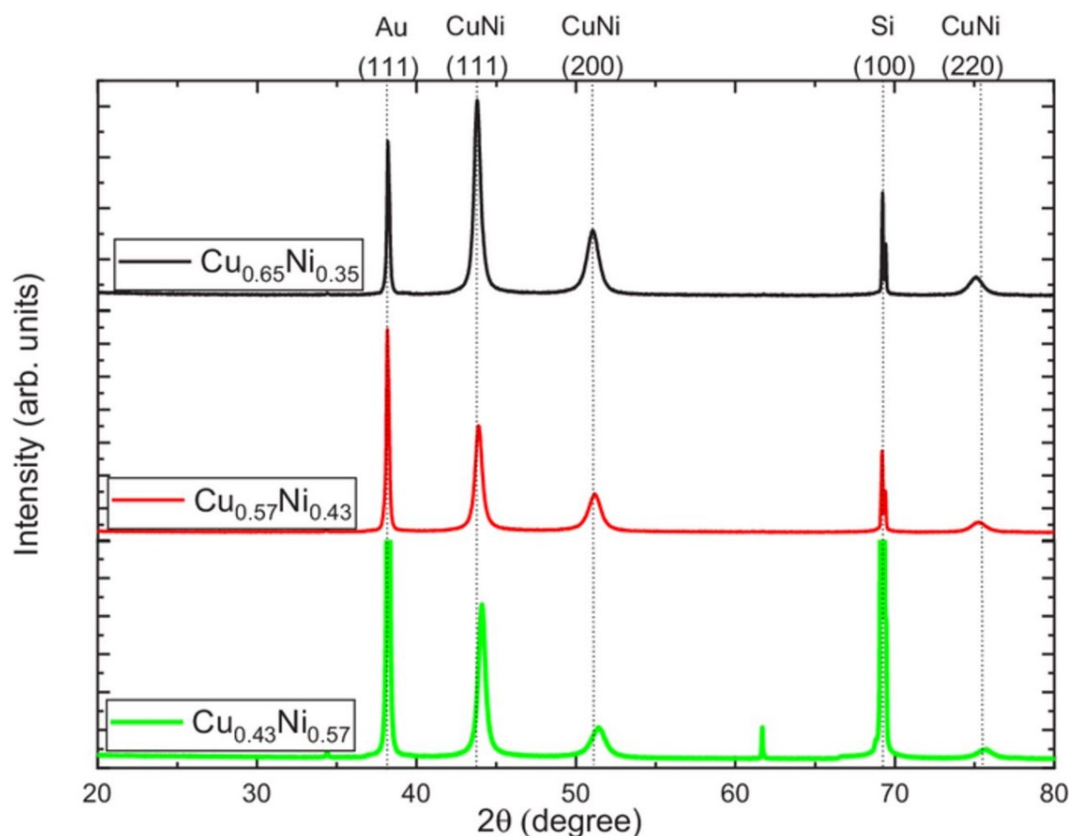


Figure 6.3 – X-ray diffractograms of CuNi T-structures with different compositions.

is more granular, however, when the Ni content exceeds 50 at% it is columnar. This morphology change is due to the change in the crystallographic orientation observed between the T-structures. The T-structures with 65 and 57 at% of Cu present a crystallographic orientation along the [111] and [200] directions and possess a granular morphology, and the sample with 43 at% of Cu exhibits a preferred oriented along the [111] direction, and is characterized by a columnar morphology. Based on the SEM images, the thickness of the samples is approx. 35 μm , 34 μm and 12 μm for $\text{Cu}_{0.65}\text{Ni}_{0.35}$, $\text{Cu}_{0.57}\text{Ni}_{0.43}$ and $\text{Cu}_{0.43}\text{Ni}_{0.57}$, respectively. It should be noted that the applied deposition time was 15 h, 12 h and 2 h for $\text{Cu}_{0.65}\text{Ni}_{0.35}$, $\text{Cu}_{0.57}\text{Ni}_{0.43}$ and $\text{Cu}_{0.43}\text{Ni}_{0.57}$, respectively.

To study the uniformity of the composition along the cross-section of the T-structures, EDX analysis was performed along the thickness of the samples (see Appendix figure 8 and table 5 in the supporting information). The Ni and Cu contents in the areas of interest are presented in Table 6.2. The composition is uniform along the cross-section for $\text{Cu}_{0.65}\text{Ni}_{0.35}$ and $\text{Cu}_{0.43}\text{Ni}_{0.57}$; however, for $\text{Cu}_{0.57}\text{Ni}_{0.43}$ there is a difference of 7%, as the current thief used for this sample was larger than for the other two. This is a good example of how crucial it is to control the area of the current thief to achieve uniform deposits in terms of thickness and composition inside the T-structures.

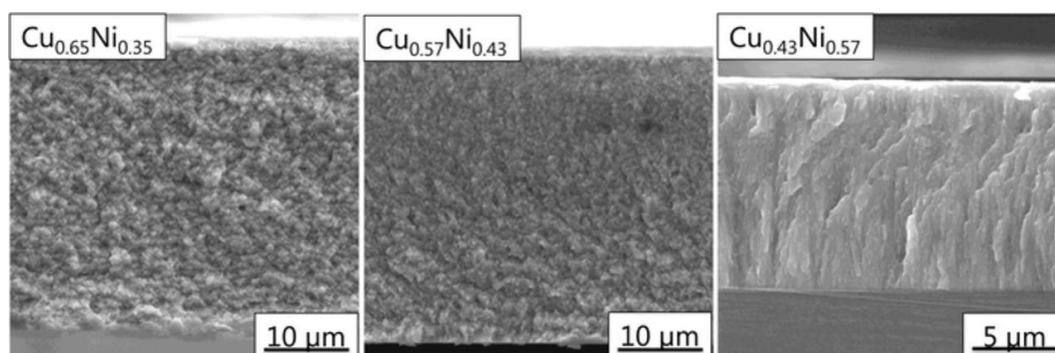


Figure 6.4 – SEM micrograph cross-sections of CuNi T-structures with different compositions.

Simulation electroplating of CuNi T-structures

Three different current densities were applied in the simulation and are shown in figure 6.5. According to the simulations, the composition of the CuNi T-structures for current densities of -35, -60 and -90 mA/cm^2 present a composition of $\text{Cu}_{0.61}\text{Ni}_{0.39}$, $\text{Cu}_{0.55}\text{Ni}_{0.45}$ and $\text{Cu}_{0.46}\text{Ni}_{0.54}$, respectively. The mesh used in the T-structure electrodeposition simulation is shown in the appendix (Appendix figure 11) .

A comparison between the measured copper contents, as well as the simulation can be seen in figure 6.5d. The simulated values fall within or close to the range of the composition measured using EDX. Therefore, the simplified set of chemical reactions is able to predict the alloy composition for a given applied current density.

The experimental and simulated thickness and growth rate cannot be compared, as the samples were polished after deposition to yield the final component. A comparison between the deposited and simulated thickness of the deposit can be found in the following section.

Simulation, deposition and characterization of a CuNi micro-gear

To demonstrate the efficiency and possibilities of this approach, a microscale gear was deposited using a two-photon lithography template. The templates (figure 6.6b, white part) were $60\ \mu\text{m}$ high and produced in an array with a current thief area between the gears of $400\ \mu\text{m}$. The electrodeposition simulation was therefore adjusted to have an area of $800\ \mu\text{m}$ by $800\ \mu\text{m}$ with the template fixed in the center. The boundary conditions can be found in figure 6.3, they were modified with a symmetry boundary condition on the sidewalls to emulate the array of gear templates used in the experiment. The duration of the deposition process was 6 hours using the aforementioned pulse parameters and deposition conditions to yield an unpolished micro-component with minimum internal stress. An SEM image of the produced CuNi micro-gear is shown in figure 6.6a. The simulation was used to predict the composition and estimate the growth rate within the template. The mesh used in the 3D microscopic gear electrodeposition simulation is shown in the appendix (Appendix figure 10). Considering

6.1. Nanocrystalline copper nickel deposition

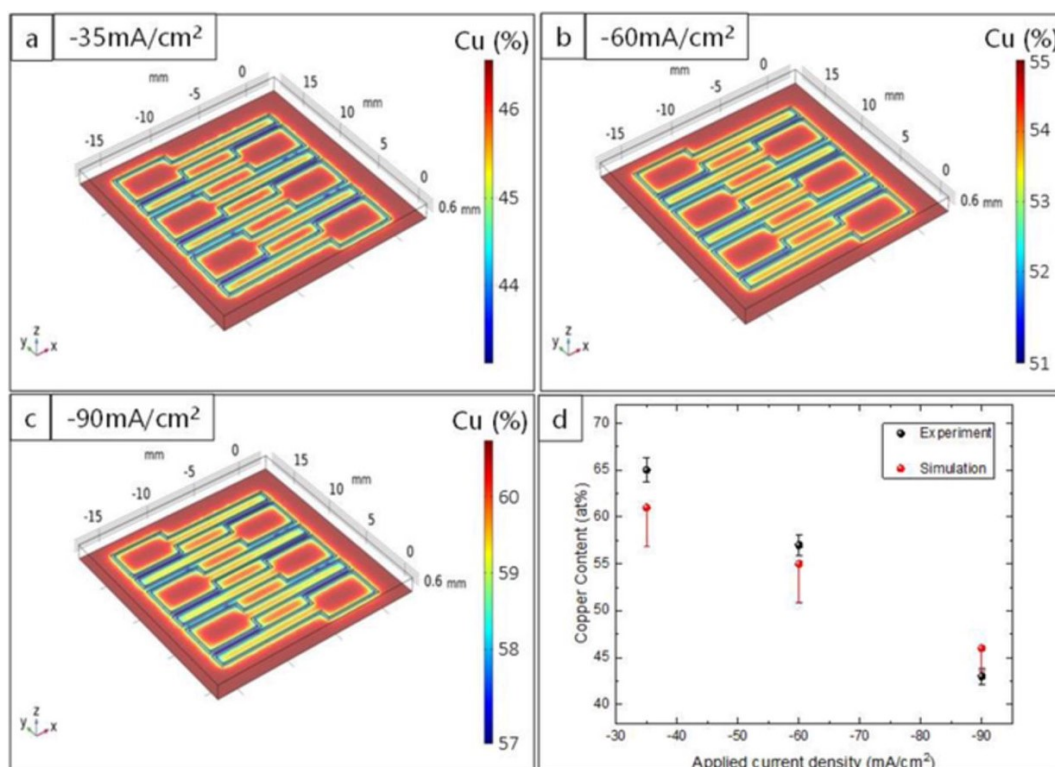


Figure 6.5 – T-structure copper contents (%) according to the simulation for (a) -35 mA/cm^2 , (b) -60 mA/cm^2 , (c) -90 mA/cm^2 and (d) comparison between the simulation and experimental composition of the deposited T-structures.

an equivalent of on-time to the experiment, the simulation shows a composition of 49% of copper, $\text{Cu}_{0.49}\text{Ni}_{0.51}$ and an average growth of $15 \mu\text{m}$, in figure 6.6b respectively 6.6c for the current thief. The deposition in the gear incorporates less copper, 48%, and deposits faster at a thickness of $16 \mu\text{m}$. The reason the simulation shows higher nickel content and thicker deposit, is that due to the insulating nature of the template, the current density is higher closer to the template, similar to the results in figure 6.5.

The final components thickness and composition deviates from the simulation due to the simplified set of chemical reactions used in the model, however the predictive power of the simulation is still within reason. The exclusion of convection in the simulation is most likely the cause for higher uniformity in the simulated compositions and growth rates compared to the final gear. Albeit these differences, the simulation can be used to determine trends in growth rate and compositions within complex templates and assist in the determination of adequate electrodeposition parameters.

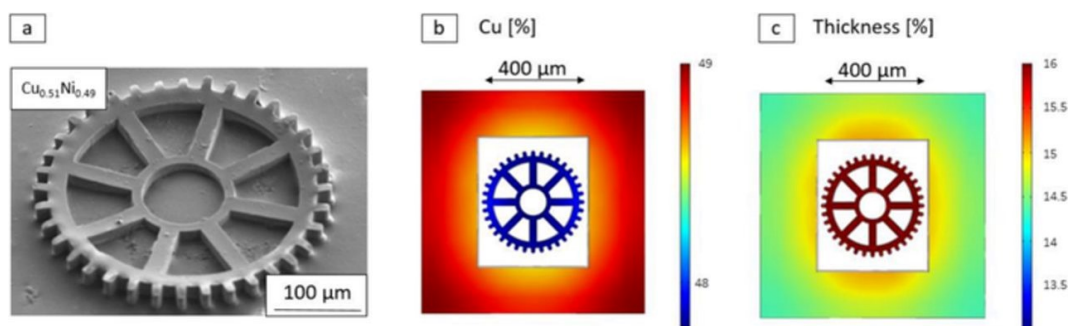


Figure 6.6 – (a) SEM image of a micro-gear deposited at -60 mA/cm^2 after resist and substrate removal. (b) Total deposition thickness of the simulation in μm . (c) Copper contents (%) in the gear according to the simulation

6.1.4 Conclusions

Nanocrystalline CuNi T-structures with different compositions were obtained using UV-LIGA, allowing for thickness control. The thickness of the produced T-structures was between 12-35 μm . A 3D model, applicable to different architectures, was proposed based on the deposition of these T-structures, using COMSOL. The performed experiments and simulations are accurate in respect to the composition, thickness and growth rate of the T-structures. Additionally, to demonstrate the efficiency and possibilities of the approach investigated in this work, a micro-gear was electrodeposited. This study provides vital knowledge for the development of new architectures, which can be used to a wide range of applications.

7 Conclusion and Outlook

The purpose of this thesis was to explore the method of two-photon lithography in combination with electrodeposition as a means of additive manufacturing.

In chapter 4.1, it was possible to show that the control of the electrodeposition process and lithography combined yields geometrical accurate and pristine micropillars. The pillars showed a homogenous response, unmatched by other manufacturing techniques such as FIB-milling. Furthermore, unlike other electrochemical additive manufacturing techniques, the method has substantial potential for batch production.

In chapter 4.2, microsprings were produced. Electrodeposition simulation showed that the pore diameter and total pore length contribute to the current density in a pore, whereas the 3D shape of a pore can be largely neglected. We reported the first metal spring compression tests of fully metallic microsprings this size. The springs proved to be mechanically stiffer than literature, but calculations of the eigenfrequency from experimental values compared to FEM simulation showed good agreement. This agreement proves that mechanical properties can be designed prior to the fabrication and TAE in combination with TPL can be used to manufacture microcomponents with intended mechanical properties. Furthermore, the agreement of theory and experiment is proof that the introduction of a 3D shape did not cause significant flaws in the microstructure of the deposits.

In chapter 5.1, micro-shear test samples were created. We successfully reported for the first time the use of negative photoresist for TAE/TPL method. Differences in template design were investigated. The electrodeposition simulation allowed to show the effectiveness of reverse pulse electrodeposition to fill difficult template features where electrolyte would be trapped. FIB-cuts of the deposit showed grains elongated in the growth direction, allowing to compare the model growth with the experimental deposit. A visible grain boundary accumulation was seen where the electrodeposition growth fronts fuse in the template. The samples showed no significant porosity, a conclusion that was already expected from the mechanical results of chapter 4.

Chapter 7. Conclusion and Outlook

At this point of the thesis, it is reasonable to conclude that for the chosen nickel sulfamate electrolyte and the experimental setup, the simulation works accurately and is not only able to address design possibilities but also helps designing pulse parameters when using pulsed electrodeposition. Due to the high conductivity and high concentration of Ni^{2+} , the influence of convection can be neglected in this system. However, in less optimized electrolytes or more complex electrolytes as discussed in the chapter 6.1, this conclusion would need to be reevaluated.

In chapter 5.2, microlattices were produced. The microlattices could be deposited due to their symmetry and were mechanical tested in compression. The lattices showed extraordinary energy absorption potential due to their sustained high constant stress and their initially high yield point. The lattices show little to no breakage at the grain boundary accumulations where electrodeposit growth fronts met. The specimen behaved according to theory and failed in accordance with the literature, further strengthening the conclusion that TAE/TPL produces structures with excellent mechanical properties.

In chapter 6.1, copper nickel alloy deposition from a citrate-based bath was investigated. The electrodeposition was modeled and the simulation compared to experimental values. Although these are simplified for 3D-simulations, the model proved to be of sufficient accuracy. The deposition was then carried out in a mesoscale 2D gear mold produced by TPL. The gear was successfully deposited into a negative photoresist mold, and the photoresist removed. The gear showed good homogeneity in composition and thickness. This work showed the potential of TPL/TAE for alloy deposition in harsher electrolyte conditions and to carry out long pulse depositions.

To conclude, EcAM by TAE is an excellent 3D manufacturing technique for pristine metallic materials such as architected materials and metamaterials. As an outlook, fully metallic 3D structures could also have various applications. While it is momentarily mainly used in micro-robotics and micromechanics, high-quality metallic structures could also have applications in microfluidics, as host structures for catalysts and other chemically active materials. With a wide range of applications and a large number of metals and alloys possible to deposit, the technique is a powerful tool for scientists to use for microscale manufacturing.

The highlights of this work have been summarized in figure 7.1.

As an outlook, building on these results, it would be possible to continue this work in one of two ways. Either by creating complex components from a single material structure or by creating 3D alloy components. For single material components, the simulation can be used to create templates with nonsymmetrical pores that fuse, thereby creating much more complex structures. The templates could also be used to deposit alloyed 3D components. This would be a challenge as every change in shape and local current density would most likely be accompanied by a change in composition and microstructure. However, accurate use of the simulation to design the template shape, to determine electrodeposition potentials with time and pulse parameters where necessary, should allow taking 3D TAE/TPL to 4D TAE/TPL

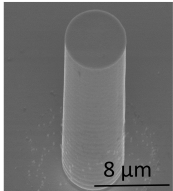
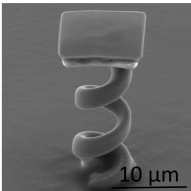
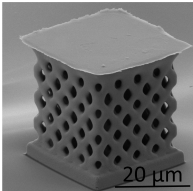
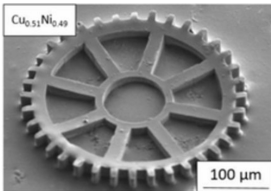
2D structure	3D single pore template	3D complex pore template	Alloy-microcomponents
Chapter 4.1	Chapter 4.2	Chapter 5.1 & 5.2	Chapter 6.1
			
- Highlights: <ul style="list-style-type: none"> • Discussion of array arrangement • Pristine non-fib milled pillars • Almost taper-free • Mechanically uniform response 	- Highlights: <ul style="list-style-type: none"> • Description of pore influence • Nickel spring systems • First cyclic compression test on metal microsprings 	- Highlights: <ul style="list-style-type: none"> • Working 3D pulse deposition simulation • Use of positive and negative photoresist • Excellent mechanical stability for energy absorption 	- Highlights: <ul style="list-style-type: none"> • Working 3D pulse electrodeposition simulation with multiple reactions • 2D metal gear deposition with TPL

Figure 7.1 – A summary showing the various highlights of each chapter.

where the composition is the fourth dimension to be controlled at will.

Bibliography

- [1] C. M. Soukoulis, S. Linden, and M. Wegener, “Negative refractive index at optical wavelengths,” *Science*, vol. 315, no. 5808, pp. 47–49, 2007.
- [2] J. Y. Qu, M. Kadic, A. Naber, and M. Wegener, “Micro-structured two-component 3d metamaterials with negative thermal-expansion coefficient from positive constituents,” *Scientific Reports*, vol. 7, p. 8, 2017.
- [3] R. Lakes, “Foam structures with a negative poissons ratio,” *Science*, vol. 235, no. 4792, pp. 1038–1040, 1987.
- [4] R. Lakes, “Advances in negative poissons ratio materials,” *Advanced Materials*, vol. 5, no. 4, pp. 293–296, 1993.
- [5] E. Armstrong and C. O’Dwyer, “Artificial opal photonic crystals and inverse opal structures - fundamentals and applications from optics to energy storage,” *Journal of Materials Chemistry C*, vol. 3, no. 24, pp. 6109–6143, 2015.
- [6] M. Q. Wang and X. G. Wang, “Electrodeposition zinc-oxide inverse opal and its application in hybrid photovoltaics,” *Solar Energy Materials and Solar Cells*, vol. 92, no. 3, pp. 357–362, 2008.
- [7] C. Accoto, A. Quattieri, F. Pisanello, C. Ricciardi, C. F. Pirri, M. De Vittorio, and F. Rizzi, “Two-photon polymerization lithography and laser doppler vibrometry of a su-8-based suspended microchannel resonator,” *Journal of Microelectromechanical Systems*, vol. 24, no. 4, pp. 1038–1042, 2015.
- [8] T. Fukushige, S. Hata, and A. Shimokohbe, “A mems conical spring actuator array,” *Journal of Microelectromechanical Systems*, vol. 14, no. 2, pp. 243–253, 2005.
- [9] T. Frenzel, C. Findeisen, M. Kadic, P. Gumbsch, and M. Wegener, “Tailored buckling microlattices as reusable light-weight shock absorbers,” *Advanced Materials*, vol. 28, no. 28, pp. 5865–, 2016.
- [10] T. A. Schaedler, A. J. Jacobsen, A. Torrents, A. E. Sorensen, J. Lian, J. R. Greer, L. Valdevit, and W. B. Carter, “Ultralight metallic microlattices,” *Science*, vol. 334, no. 6058, pp. 962–965, 2011.

Bibliography

- [11] A. Schroer, J. M. Wheeler, and R. Schwaiger, "Deformation behavior and energy absorption capability of polymer and ceramic-polymer composite microlattices under cyclic loading," *Journal of Materials Research*, vol. 33, no. 3, pp. 274–289, 2018.
- [12] J. U. Surjadi, L. B. Gao, K. Cao, R. Fan, and Y. Lu, "Mechanical enhancement of core-shell microlattices through high-entropy alloy coating," *Scientific Reports*, vol. 8, p. 10, 2018.
- [13] S. Q. Yuan, C. K. Chua, and K. Zhou, "3d-printed mechanical metamaterials with high energy absorption," *Advanced Materials Technologies*, vol. 4, no. 3, p. 9, 2019.
- [14] K. Wei, Q. D. Yang, B. Ling, H. Q. Xie, Z. L. Qu, and D. N. Fang, "Mechanical responses of titanium 3d kagome lattice structure manufactured by selective laser melting," *Extreme Mechanics Letters*, vol. 23, pp. 41–48, 2018.
- [15] S. Krodel and C. Daraio, "Microlattice metamaterials for tailoring ultrasonic transmission with elastoacoustic hybridization," *Physical Review Applied*, vol. 6, no. 6, p. 9, 2016.
- [16] C. Xu, B. M. Gallant, P. U. Wunderlich, T. Lohmann, and J. R. Greer, "Three-dimensional au microlattices as positive electrodes for li-o-2 batteries," *Acs Nano*, vol. 9, no. 6, pp. 5876–5883, 2015.
- [17] M. S. Saleh, J. Li, J. Park, and R. Panat, "3d printed hierarchically-porous microlattice electrode materials for exceptionally high specific capacity and areal capacity lithium ion batteries," *Additive Manufacturing*, vol. 23, pp. 70–78, 2018.
- [18] T. Chen, S. Y. Li, and H. Sun, "Metamaterials application in sensing," *Sensors*, vol. 12, no. 3, pp. 2742–2765, 2012.
- [19] "Lateral trapezoid microfluidic platform for investigating mechanotransduction of cells to spatial shear stress gradients," *Sensors and Actuators B: Chemical*, vol. 251, pp. 963 – 975, 2017.
- [20] T. T. Li, Y. Y. Chen, X. Y. Hu, Y. B. Li, and L. F. Wang, "Exploiting negative poisson's ratio to design 3d-printed composites with enhanced mechanical properties," *Materials & Design*, vol. 142, pp. 247–258, 2018.
- [21] A. Alderson and K. E. Evans, "Molecular origin of auxetic behavior in tetrahedral framework silicates," *Physical Review Letters*, vol. 89, no. 22, p. 4, 2002.
- [22] D. C. Jang and J. R. Greer, "Transition from a strong-yet-brittle to a stronger-and-ductile state by size reduction of metallic glasses," *Nature Materials*, vol. 9, no. 3, pp. 215–219, 2010.
- [23] S. Alvo, D. Decanini, L. Couraud, A. M. Haghiri-Gosnet, G. Hwang, and Ieee, "Assembly and mechanical characterizations of polymer microhelical devices," in *IEEE/RSJ International Conference on Intelligent Robots and Systems (IROS)*, IEEE International Conference on Intelligent Robots and Systems, (NEW YORK), pp. 4656–4661, Ieee, 2014.

-
- [24] B. J. Nelson, I. K. Kaliakatsos, and J. J. Abbott, *Microrobots for Minimally Invasive Medicine*, vol. 12 of *Annual Review of Biomedical Engineering*, pp. 55–85. Palo Alto: Annual Reviews, 2010.
- [25] M. A. Zeeshan, R. Grisch, E. Pellicer, K. M. Sivaraman, K. E. Peyer, J. Sort, B. Ozkale, M. S. Sakar, B. J. Nelson, and S. Pane, “Hybrid helical magnetic microrobots obtained by 3d template-assisted electrodeposition,” *Small*, vol. 10, no. 7, pp. 1284–1288, 2014.
- [26] V. G. Veselago, “Electrodynamics of substances with simultaneously negative values of sigma and mu,” *Soviet Physics Uspekhi-Ussr*, vol. 10, no. 4, pp. 509–&, 1968.
- [27] V. G. Veselago and E. E. Narimanov, “The left hand of brightness: past, present and future of negative index materials,” *Nature Materials*, vol. 5, no. 10, pp. 759–762, 2006.
- [28] D. R. Smith, W. J. Padilla, D. C. Vier, S. C. Nemat-Nasser, and S. Schultz, “Composite medium with simultaneously negative permeability and permittivity,” *Physical Review Letters*, vol. 84, no. 18, pp. 4184–4187, 2000.
- [29] H. J. Lee, H. S. Lee, K. H. Yoo, J. G. Yook, and Ieee, “On the possibility of biosensors based on split ring resonators,” *2008 European Microwave Conference, Vols 1-3*, pp. 1071–+, 2008.
- [30] M. S. Boybay and O. M. Ramahi, “Material characterization using complementary split-ring resonators,” *Ieee Transactions on Instrumentation and Measurement*, vol. 61, no. 11, pp. 3039–3046, 2012.
- [31] A. Salim and S. Lim, “Complementary split-ring resonator-loaded microfluidic ethanol chemical sensor,” *Sensors*, vol. 16, no. 11, p. 13, 2016.
- [32] W. Ding, Y. X. Wang, H. Chen, and S. Y. Chou, “Plasmonic nanocavity organic light-emitting diode with significantly enhanced light extraction, contrast, viewing angle, brightness, and low-glare,” *Advanced Functional Materials*, vol. 24, no. 40, pp. 6329–6339, 2014.
- [33] C. M. Soukoulis and M. Wegener, “Past achievements and future challenges in the development of three-dimensional photonic metamaterials,” *Nature Photonics*, vol. 5, no. 9, pp. 523–530, 2011.
- [34] R. Malureanu, A. Alabastri, W. Cheng, R. Kiyon, B. Chichkov, A. Andryieuski, and A. Lavri-nenko, “Enhanced broadband optical transmission in metallized woodpiles,” *Applied Physics a-Materials Science & Processing*, vol. 103, no. 3, pp. 749–753, 2011.
- [35] M. Goeppert-Mayer, “Elementary processes with two quantum transitions,” *Annalen Der Physik*, vol. 18, no. 7-8, pp. 466–479, 2009.
- [36] A. Vyatskikh, S. Delalande, A. Kudo, X. Zhang, C. M. Portela, and J. R. Greer, “Additive manufacturing of 3d nano-architected metals,” *Nature Communications*, vol. 9, p. 8, 2018.

- [37] D. Gailevicius, V. Padolskyte, L. Mikoliunaite, S. Sakirzanovas, S. Juodkasis, and M. Malinauskas, "Additive-manufacturing of 3d glass-ceramics down to nanoscale resolution," *Nanoscale Horizons*, vol. 4, no. 3, pp. 647–651, 2019.
- [38] M. Mieszala, M. Hasegawa, G. Guillonneau, J. Bauer, R. Raghavan, C. Frantz, O. Kraft, S. Mischler, J. Michler, and L. Philippe, "Micromechanics of amorphous metal/polymer hybrid structures with 3d cellular architectures: Size effects, buckling behavior, and energy absorption capability," *Small*, vol. 13, no. 8, p. 13, 2017.
- [39] J. F. Fan, K. Sugioka, and K. Toyoda, "Low-temperature growth of thin-films of Al_2O_3 by sequential surface chemical-reaction of trimethylaluminum and H_2O_2 ," *Japanese Journal of Applied Physics Part 2-Letters & Express Letters*, vol. 30, no. 6B, pp. L1139–L1141, 1991.
- [40] S. M. George, "Atomic layer deposition: An overview," *Chemical Reviews*, vol. 110, no. 1, pp. 111–131, 2010.
- [41] M. S. Rill, C. Plet, M. Thiel, I. Staude, G. Von Freymann, S. Linden, and M. Wegener, "Photonic metamaterials by direct laser writing and silver chemical vapour deposition," *Nature Materials*, vol. 7, no. 7, pp. 543–546, 2008.
- [42] J. Song, L. B. Gao, K. Cao, H. T. Zhang, S. Xu, C. C. Jiang, J. U. Surjadi, Y. M. Xu, and Y. Lu, "Metal-coated hybrid meso-lattice composites and their mechanical characterizations," *Composite Structures*, vol. 203, pp. 750–763, 2018.
- [43] C. Frantz, N. Stein, L. Gravier, S. Granville, and C. Boulanger, "Electrodeposition and characterization of bismuth telluride nanowires," *Journal of Electronic Materials*, vol. 39, no. 9, pp. 2043–2048, 2010.
- [44] X. H. Li, E. Koukharenko, I. S. Nandhakumar, J. Tudor, S. P. Beeby, and N. M. White, "High density p-type $\text{Bi}_{0.5}\text{Sb}_{1.5}\text{Te}_3$ nanowires by electrochemical templating through ion-track lithography," *Physical Chemistry Chemical Physics*, vol. 11, no. 18, pp. 3584–3590, 2009.
- [45] M. S. Sander, R. Gronsky, T. Sands, and A. M. Stacy, "Structure of bismuth telluride nanowire arrays fabricated by electrodeposition into porous anodic alumina templates," *Chemistry of Materials*, vol. 15, no. 1, pp. 335–339, 2003.
- [46] J. N. Balaraju, T. Narayanan, and S. K. Seshadri, "Electroless ni-p composite coatings," *Journal of Applied Electrochemistry*, vol. 33, no. 9, pp. 807–816, 2003.
- [47] C. Levy-Clement and J. Elias, "Optimization of the design of extremely thin absorber solar cells based on electrodeposited ZnO nanowires," *Chemphyschem*, vol. 14, no. 10, pp. 2321–2330, 2013.
- [48] J. Garcia-Torres, A. Serra, P. Tierno, X. Alcobe, and E. Valles, "Magnetic propulsion of recyclable catalytic nanocleaners for pollutant degradation," *Acs Applied Materials & Interfaces*, vol. 9, no. 28, pp. 23859–23868, 2017.

- [49] C. Croenne, J. O. Vasseur, O. B. Matar, M. F. Ponge, P. A. Deymier, A. C. Hladky-Hennion, and B. Dubus, "Brillouin scattering-like effect and non-reciprocal propagation of elastic waves due to spatio-temporal modulation of electrical boundary conditions in piezoelectric media," *Applied Physics Letters*, vol. 110, no. 6, p. 5, 2017.
- [50] P. Colson, R. Cloots, and C. Henrist, "Experimental design applied to spin coating of 2d colloidal crystal masks: A relevant method?," *Langmuir*, vol. 27, no. 21, pp. 12800–12806, 2011.
- [51] X. H. Xia, J. P. Tu, X. L. Wang, C. D. Gu, and X. B. Zhao, "Hierarchically porous nio film grown by chemical bath deposition via a colloidal crystal template as an electrochemical pseudocapacitor material," *Journal of Materials Chemistry*, vol. 21, no. 3, pp. 671–679, 2011.
- [52] A. Tal, Y. S. Chen, H. E. Williams, R. C. Rumpf, and S. M. Kuebler, "Fabrication and characterization of three-dimensional copper metallodielectric photonic crystals," *Optics Express*, vol. 15, no. 26, pp. 18283–18293, 2007.
- [53] Y. S. Huang, X. T. Zeng, I. Annergren, and E. Liu, "Development of electroless nip-ptfe-sic composite coating," *Surface & Coatings Technology*, vol. 167, no. 2-3, pp. 207–211, 2003.
- [54] G. Chatzipirpiridis, C. de Marco, E. Pellicer, O. Ergeneman, J. Sort, B. J. Nelson, and S. Pane, "Template-assisted electroforming of fully semi-hard-magnetic helical microactuators," *Advanced Engineering Materials*, vol. 20, no. 9, p. 5, 2018.
- [55] C. C. J. Alcântara, S. Kim, S. Lee, B. Jang, P. Thakolkaran, J.-Y. Kim, H. Choi, B. J. Nelson, and S. Pané, "3d fabrication of fully iron magnetic microrobots," *Small*, vol. 15, no. 16, p. 1805006, 2019.
- [56] X. W. Gu and J. R. Greer, "Ultra-strong architected cu meso-lattices," *Extreme Mechanics Letters*, vol. 2, pp. 7–14, 2015.
- [57] P. Schürch, R. Ramachandramoorthy, L. Pethö, J. Michler, and L. Philippe, "Additive manufacturing by template-assisted 3d electrodeposition: Nanocrystalline nickel microsprings and microspring arrays," *Applied Materials Today*, p. 100472, 2019.
- [58] C. A. Schuh, T. G. Nieh, and T. Yamasaki, "Hall-petch breakdown manifested in abrasive wear resistance of nanocrystalline nickel," *Scripta Materialia*, vol. 46, no. 10, pp. 735–740, 2002.
- [59] R. K. Dube and A. Tewari, "Some aspects of nanocrystalline materials for electrical and magnetic applications," *IETE Technical Review*, vol. 19, no. 5, pp. 317–322, 2002.
- [60] A. M. Pillai*, A. Rajendra, and A. K. Sharma, "Pulse electrodeposition of nanocrystalline nickel on aa 6061 for space applications," *Transactions of the IMF*, vol. 90, no. 1, pp. 44–51, 2012.

- [61] C. Gu, J. Lian, J. He, Z. Jiang, and Q. Jiang, "High corrosion-resistance nanocrystalline ni coating on az91d magnesium alloy," *Surface and Coatings Technology*, vol. 200, no. 18, pp. 5413 – 5418, 2006.
- [62] F. Giro, K. Bedner, C. Dhum, J. E. Hoffmann, S. P. Heussler, L. Jian, U. Kirsch, H. O. Moser, and M. Saumer, "Pulsed electrodeposition of high aspect-ratio nife assemblies and its influence on spatial alloy composition," *Microsystem Technologies-Micro-and Nanosystems-Information Storage and Processing Systems*, vol. 14, no. 8, pp. 1111–1115, 2008.
- [63] P. Chowdhury, H. Sehitoglu, H. J. Maier, and R. Rateick, "Strength prediction in nico alloys – the role of composition and nanotwins," *International journal of plasticity*, vol. 79, pp. 237–258, 2016.
- [64] H. Natter, M. Schmelzer, and R. Hempelmann, "Nanocrystalline nickel and nickel-copper alloys: Synthesis, characterization, and thermal stability," *Journal of materials research*, vol. 13, no. 5, pp. 1186–1197, 1998.
- [65] S. Rode, C. Henninot, and M. Matlos, "Complexation chemistry in nickel and copper-nickel alloy plating from citrate baths," *Journal of the Electrochemical Society*, vol. 152, no. 4, pp. C248–C254, 2005.
- [66] C. R. Carpenter, P. H. Shipway, and Y. Zhu, "Electrodeposition of nickel-carbon nanotube nanocomposite coatings for enhanced wear resistance," *Wear*, vol. 271, no. 9-10, pp. 2100–2105, 2011.
- [67] N. Eliaz, T. Sridhar, and E. Gileadi, "Synthesis and characterization of nickel tungsten alloys by electrodeposition," *Electrochimica Acta*, vol. 50, no. 14, pp. 2893 – 2904, 2005.
- [68] J. K. Gansel, M. Thiel, M. S. Rill, M. Decker, K. Bade, V. Saile, G. von Freymann, S. Linden, and M. Wegener, "Gold helix photonic metamaterial as broadband circular polarizer," *Science*, vol. 325, no. 5947, pp. 1513–1515, 2009.
- [69] S. Coleman and S. Roy, "Effect of ultrasound on mass transfer during electrodeposition for electrodes separated by a narrow gap," *Chemical Engineering Science*, vol. 113, pp. 35 – 44, 2014.
- [70] G. Taylor, "The motion of a sphere in a rotating liquid," *Proceedings of the royal society of london series A - Papers of a mathematical and physical character*, vol. 102, pp. 180–189, NOV 1922.
- [71] P. C. Andricacos, C. Arana, J. Tabib, J. Dukovic, and L. T. Romankiw, "Electrodeposition of nickel-iron alloys .1. effect of agitation," *Journal of the Electrochemical Society*, vol. 136, no. 5, pp. 1336–1340, 1989.
- [72] T. A. Green, A. E. Russell, and S. Roy, "The development of a stable citrate electrolyte for the electrodeposition of copper-nickel alloys," *Journal of the Electrochemical Society*, vol. 145, no. 3, pp. 875–881, 1998.

-
- [73] E. B. Saubestre, "Electroplating on certain transition metals: (groups iv , v , vi)," *Journal of The Electrochemical Society*, vol. 106, no. 4, pp. 305–309, 1959.
- [74] J. P. Hoare, "On the role of boric acid in the watts bath," *Journal of The Electrochemical Society*, vol. 133, no. 12, pp. 2491–2494, 1986.
- [75] Y. Tsuru, M. Nomura, and F. R. Foulkes, "Effects of boric acid on hydrogen evolution and internal stress in films deposited from a nickel sulfamate bath," *Journal of Applied Electrochemistry*, vol. 32, no. 6, pp. 629–634, 2002.
- [76] A. M. Rashidi and A. Amadeh, "The effect of saccharin addition and bath temperature on the grain size of nanocrystalline nickel coatings," *Surface & Coatings Technology*, vol. 204, no. 3, pp. 353–358, 2009.
- [77] D. Gay and J. Gambelin, *Criteria for Dimensioning*, ch. 7, pp. 365–405. John Wiley & Sons, Ltd, 2010.
- [78] D. Gay and J. Gambelin, *Practical Aspects of Finite Element Modeling*, ch. 8, pp. 407–461. John Wiley & Sons, Ltd, 2010.
- [79] J. Fischer and M. Wegener, "Three-dimensional optical laser lithography beyond the diffraction limit," *Laser & Photonics Reviews*, vol. 7, no. 1, pp. 22–44, 2013.
- [80] D. W. Yee, M. D. Schulz, R. H. Grubbs, and J. R. Greer, "Functionalized 3d architected materials via thiol-michael addition and two-photon lithography," *Advanced Materials*, vol. 29, no. 16, p. 9, 2017.
- [81] T. Buckmann, N. Stenger, M. Kadic, J. Kaschke, A. Frolich, T. Kennerknecht, C. Eberl, M. Thiel, and M. Wegener, "Tailored 3d mechanical metamaterials made by dip-in direct-laser-writing optical lithography," *Advanced Materials*, vol. 24, no. 20, pp. 2710–2714, 2012.
- [82] T. Frenzel, M. Kadic, and M. Wegener, "Three-dimensional mechanical metamaterials with a twist," *Science*, vol. 358, no. 6366, pp. 1072–1074, 2017.
- [83] A. Mata, A. J. Fleischman, and S. Roy, "Fabrication of multi-layer su-8 microstructures," *Journal of Micromechanics and Microengineering*, vol. 16, no. 2, pp. 276–284, 2006.
- [84] J. K. Gansel, M. Latzel, A. Frolich, J. Kaschke, M. Thiel, and M. Wegener, "Tapered gold-helix metamaterials as improved circular polarizers," *Applied Physics Letters*, vol. 100, no. 10, p. 3, 2012.
- [85] J. Qu and M. Cherkaoui, *Introduction*, ch. 1, pp. 1–10. John Wiley & Sons, Ltd, 2007.
- [86] D. Casari, L. Petho, P. Schurch, X. Maeder, L. Philippe, J. Michler, P. Zysset, and J. Schwiedrzik, "A self-aligning microtensile setup: Application to single-crystal gaas microscale tension-compression asymmetry," *Journal of Materials Research*, vol. 34, no. 14, pp. 2517–2534, 2019.

Bibliography

- [87] E. Pellicer, A. Varea, S. Pane, K. M. Sivaraman, B. J. Nelson, S. Surinach, M. D. Baro, and J. Sort, "A comparison between fine-grained and nanocrystalline electrodeposited cu-ni films. insights on mechanical and corrosion performance," *Surface & Coatings Technology*, vol. 205, no. 23-24, pp. 5285–5293, 2011.
- [88] F. Ebrahimi, G. R. Bourne, M. S. Kelly, and T. E. Matthews, "Mechanical properties of nanocrystalline nickel produced by electrodeposition," *Nanostructured Materials*, vol. 11, no. 3, pp. 343–350, 1999.
- [89] G. Guillonneau, M. Mieszala, J. Wehrs, J. Schwiedrzik, S. Grop, D. Frey, L. Philippe, J. M. Breguet, J. Michler, and J. M. Wheeler, "Nanomechanical testing at high strain rates: New instrumentation for nanoindentation and microcompression," *Materials & Design*, vol. 148, pp. 39–48, 2018.
- [90] G. Mohanty, J. Wehrs, B. L. Boyce, A. Taylor, M. Hasegawa, L. Philippe, and J. Michler, "Room temperature stress relaxation in nanocrystalline ni measured by micropillar compression and miniature tension," *Journal of Materials Research*, vol. 31, no. 8, pp. 1085–1095, 2016.
- [91] G. Mohanty, J. M. Wheeler, R. Raghavan, J. Wehrs, M. Hasegawa, S. Mischler, L. Philippe, and J. Michler, "Elevated temperature, strain rate jump microcompression of nanocrystalline nickel," *Philosophical Magazine*, vol. 95, no. 16-18, pp. 1878–1895, 2015.
- [92] S. K. Griffiths, R. H. Nilson, A. Ting, R. W. Bradshaw, W. D. Bonivert, and J. M. Hruby, "Modeling electrodeposition for liga microdevice ice fabrication," *Microsystem Technologies*, vol. 4, no. 2, pp. 98–101, 1998.
- [93] S. K. Griffiths, R. H. Nilson, R. W. Bradshaw, A. Ting, W. D. Bonivert, J. T. Hachman, and J. M. Hruby, "Transport limitations in electrodeposition for liga microdevice fabrication," in *SPIE Conference on Micromachining and Microfabrication Process Technology IV*, vol. 3511 of *Proceedings of the Society of Photo-Optical Instrumentation Engineers (Spie)*, (BELLINGHAM), pp. 364–375, Spie-Int Soc Optical Engineering, 1998.
- [94] S. K. Griffiths, J. A. W. Crowell, B. L. Kistler, and A. S. Dryden, "Dimensional errors in liga-produced metal structures due to thermal expansion and swelling of pmma," *Journal of Micromechanics and Microengineering*, vol. 14, no. 11, pp. 1548–1557, 2004.
- [95] A. C. West, "Theory of filling of high-aspect ratio trenches and vias in presence of additives," *Journal of the Electrochemical Society*, vol. 147, no. 1, pp. 227–232, 2000.
- [96] A. C. West, C. C. Cheng, and B. C. Baker, "Pulse reverse copper electrodeposition in high aspect ratio trenches and vias," *Journal of the Electrochemical Society*, vol. 145, no. 9, pp. 3070–3074, 1998.
- [97] E. W. Becker, W. Ehrfeld, D. Munchmeyer, H. Betz, A. Heuberger, S. Pongratz, W. Glashauser, H. J. Michel, and R. Vonsiemens, "Production of separation-nozzle sys-

- tems for uranium enrichment by a combination of x-ray-lithography and galvanoplas-
tics," *Naturwissenschaften*, vol. 69, no. 11, pp. 520–523, 1982.
- [98] L. Philippe, N. Kacem, and J. Michler, "Electrochemical deposition of metals inside high
aspect ratio nanoelectrode array: Analytical current expression and multidimensional
kinetic model for cobalt nanostructure synthesis," *Journal of Physical Chemistry C*,
vol. 111, no. 13, pp. 5229–5235, 2007.
- [99] K. S. Drese, "Design rules for electroforming in the liga process," *Journal of the Electro-
chemical Society*, vol. 151, no. 6, pp. D39–D45, 2004.
- [100] S. K. Verma and H. Wilman, "Epitaxy and oblique face development in nickel electrode-
posits on a copper cube face, in relation to rate of deposition, deposit thickness, degree
of stirring and bath temperature," *Journal of Physics D-Applied Physics*, vol. 4, no. 8,
pp. 1167–8, 1971.
- [101] G. Kenanakis, A. Xomalis, A. Selimis, M. Vamvakaki, M. Farsari, M. Kafesaki, C. M. Souk-
oulis, and E. N. Economou, "Three-dimensional infrared metamaterial with asymmetric
transmission," *Acs Photonics*, vol. 2, no. 2, pp. 287–294, 2015.
- [102] G. S. Huang and Y. F. Mei, "Helices in micro-world: Materials, properties, and applica-
tions," *Journal of Materiomics*, vol. 1, no. 4, pp. 296–306, 2015.
- [103] R. N. Dean, P. C. Nordine, and C. G. Christodoulou, "3-d helical thz antennas," *Microwave
and Optical Technology Letters*, vol. 24, no. 2, pp. 106–111, 2000.
- [104] S. J. Mazlouman, A. Mahanfar, C. Menon, and R. G. Vaughan, "Reconfigurable axial-
mode helix antennas using shape memory alloys," *Ieee Transactions on Antennas and
Propagation*, vol. 59, no. 4, pp. 1070–1077, 2011.
- [105] S. V. Kesapragada, P. Victor, O. Nalamasu, and D. Gall, "Nanospring pressure sensors
grown by glancing angle doposition," *Nano Letters*, vol. 6, no. 4, pp. 854–857, 2006.
- [106] A. Ambrosi, J. G. S. Moo, and M. Pumera, "Helical 3d-printed metal electrodes as custom-
shaped 3d platform for electrochemical devices," *Advanced Functional Materials*, vol. 26,
no. 5, pp. 698–703, 2016.
- [107] D. J. Bell, Y. Sun, L. Zhang, L. X. Dong, B. J. Nelson, and D. Grutzmacher, "Three-
dimensional nanosprings for electromechanical sensors," *Sensors and Actuators a-
Physical*, vol. 130, pp. 54–61, 2006.
- [108] C. B. Cao, H. L. Du, Y. J. Xu, H. S. Zhu, T. H. Zhang, and R. Yang, "Superelastic and spring
properties of si₃n₄ microcoils," *Advanced Materials*, vol. 20, no. 9, pp. 1738–+, 2008.
- [109] P. X. Gao, W. J. Mai, and Z. L. Wang, "Superelasticity and nanofracture mechanics of zno
nanohelices," *Nano Letters*, vol. 6, no. 11, pp. 2536–2543, 2006.

Bibliography

- [110] Z. R. Yi, Y. Lei, X. Y. Zhang, Y. N. Chen, J. J. Guo, G. J. Xu, M. F. Yu, and P. Cui, "Ultralow flexural properties of copper microhelices fabricated via electrodeposition-based three-dimensional direct-writing technology," *Nanoscale*, vol. 9, no. 34, pp. 12524–12532, 2017.
- [111] R. W. Armstrong and N. Balasubramanian, "Unified hall-petch description of nano-grain nickel hardness, flow stress and strain rate sensitivity measurements," *Aip Advances*, vol. 7, no. 8, p. 5, 2017.
- [112] D. Pan, T. G. Nieh, and M. W. Chen, "Strengthening and softening of nanocrystalline nickel during multistep nanoindentation," *Applied Physics Letters*, vol. 88, no. 16, p. 3, 2006.
- [113] J. Wehrs, G. Mohanty, G. Guillonneau, A. A. Taylor, X. Maeder, D. Frey, L. Philippe, S. Mischler, J. M. Wheeler, and J. Michler, "Comparison of in situ micromechanical strain-rate sensitivity measurement techniques," *Jom*, vol. 67, no. 8, pp. 1684–1693, 2015.
- [114] W. E. G. Hansal, H. Steiner, R. Mann, M. Halmdienst, J. Schalko, F. Keplinger, and P. Svasek, "Microgalvanic nickel pulse plating process for the fabrication of thermal microactuators," *Microsystem Technologies-Micro-and Nanosystems-Information Storage and Processing Systems*, vol. 20, no. 4-5, pp. 681–689, 2014.
- [115] C. D. Gu, J. S. Lian, J. G. He, Z. H. Jiang, and Q. Jiang, "High corrosion-resistance nanocrystalline ni coating on az91d magnesium alloy," *Surface & Coatings Technology*, vol. 200, no. 18-19, pp. 5413–5418, 2006.
- [116] Z. Qi, H. R. Geng, X. G. Wang, C. C. Zhao, H. Ji, C. Zhang, J. L. Xu, and Z. H. Zhang, "Novel nanocrystalline pdni alloy catalyst for methanol and ethanol electro-oxidation in alkaline media," *Journal of Power Sources*, vol. 196, no. 14, pp. 5823–5828, 2011.
- [117] A. J. Vizcaino, A. Carriero, and J. A. Calles, "Hydrogen production by ethanol steam reforming over cu-ni supported catalysts," *International Journal of Hydrogen Energy*, vol. 32, no. 10-11, pp. 1450–1461, 2007.
- [118] A. B. Laursen, K. R. Patraju, M. J. Whitaker, M. Retuerto, T. Sarkar, N. Yao, K. V. Ramanujachary, M. Greenblatt, and G. C. Dismukes, "Nanocrystalline ni₅p₄: a hydrogen evolution electrocatalyst of exceptional efficiency in both alkaline and acidic media," *Energy & Environmental Science*, vol. 8, no. 3, pp. 1027–1034, 2015.
- [119] C. V. Manzano, P. Schurch, L. Petho, G. Burki, J. Michler, and L. Philippe, "High aspect-ratio nanocrystalline cuni t-structures and micro-gears: Synthesis, numerical modeling and characterization," *Journal of the Electrochemical Society*, vol. 166, no. 10, pp. E310–E316, 2019.

-
- [120] K. S. Chen and G. H. Evans, "Two-dimensional modeling of nickel electrodeposition in liga microfabrication," *Microsystem Technologies-Micro-and Nanosystems-Information Storage and Processing Systems*, vol. 10, no. 6-7, pp. 444–450, 2004.
- [121] M. Hasegawa, Y. Negishi, T. Nakanishi, and T. Osaka, "Effects of additives on copper electrodeposition in submicrometer trenches," *Journal of the Electrochemical Society*, vol. 152, no. 4, pp. C221–C228, 2005.
- [122] S. K. Kim, J. E. Bonevich, D. Josell, and T. P. Moffat, "Electrodeposition of ni in submicrometer trenches," *Journal of the Electrochemical Society*, vol. 154, no. 9, pp. D443–D451, 2007.
- [123] U. Landau, *Current Distribution in Electrochemical Cells: Analytical and Numerical Modeling*, pp. 451–501. Modern Aspects of Electrochemistry, New York: Springer, 2009.
- [124] S. Mehdizadeh, J. O. Dukovic, P. C. Andricacos, L. T. Romankiw, and H. Y. Cheh, "The influence of lithographic patterning on current distribution - a model for microfabrication by electrodeposition," *Journal of the Electrochemical Society*, vol. 139, no. 1, pp. 78–91, 1992.
- [125] S. Mehdizadeh, J. Dukovic, P. C. Andricacos, L. T. Romankiw, and H. Y. Cheh, "The influence of lithographic patterning on current distribution in electrodeposition - experimental-study and mass-transfer effects," *Journal of the Electrochemical Society*, vol. 140, no. 12, pp. 3497–3505, 1993.
- [126] C. Wagner, "Theoretical analysis of the current density distribution in electrolytic cells," *Journal of the Electrochemical Society*, vol. 98, no. 3, pp. 116–128, 1951.
- [127] F. Ebrahimi and Z. Ahmed, "The effect of current density on properties of electrodeposited nanocrystalline nickel," *Journal of Applied Electrochemistry*, vol. 33, no. 8, pp. 733–739, 2003.
- [128] F. Nasirpour, "Electrodeposition of nanostructured materials," *Electrodeposition of Nanostructured Materials*, vol. 62, pp. 1–325, 2017.
- [129] W. M. Yin, S. H. Whang, R. Mirshams, and C. H. Xiao, "Creep behavior of nanocrystalline nickel at 290 and 373 k," *Materials Science and Engineering a-Structural Materials Properties Microstructure and Processing*, vol. 301, no. 1, pp. 18–22, 2001.
- [130] N. Wang, Z. R. Wang, K. T. Aust, and U. Erb, "Room temperature creep behavior of nanocrystalline nickel produced by an electrodeposition technique," *Materials Science and Engineering a-Structural Materials Properties Microstructure and Processing*, vol. 237, no. 2, pp. 150–158, 1997.
- [131] R. H. Nilson and S. K. Griffiths, "Natural convection in trenches of high aspect ratio," *Journal of the Electrochemical Society*, vol. 150, no. 6, pp. C401–C412, 2003.

Bibliography

- [132] R. H. Nilson and S. K. Griffiths, "Natural convection in trenches of high aspect ratio," *Journal of the Electrochemical Society*, vol. 150, no. 6, pp. C401–C412, 2003.
- [133] T. H. Tsai, H. Yang, R. Chein, and M. S. Yeh, "Two-dimensional simulations of ion concentration distribution in microstructural electroforming," *International Journal of Advanced Manufacturing Technology*, vol. 57, no. 5-8, pp. 639–646, 2011.
- [134] Y. M. Yeh, C. S. Chen, M. H. Tsai, Y. C. Shyng, S. Y. Lee, and K. L. Ou, "Effect of pulse-reverse current on microstructure and properties of electroformed nickel-iron mold insert," *Japanese Journal of Applied Physics Part 1-Regular Papers Brief Communications & Review Papers*, vol. 44, no. 2, pp. 1086–1090, 2005.
- [135] S. D. Yang, Z. Thacker, E. Allison, M. Bennett, N. Cole, and P. J. Pinhero, "Electrodeposition of copper for three-dimensional metamaterial fabrication," *Acs Applied Materials & Interfaces*, vol. 9, no. 46, pp. 40921–40929, 2017.
- [136] M. Halmdienst, W. E. G. Hansal, G. Kattenhauser, and W. Kautek, "Pulse plating of nickel: influence of electrochemical parameters and composition of electrolyte," *Transactions of the Institute of Metal Finishing*, vol. 85, no. 1, pp. 22–26, 2007.
- [137] M. Power and G. Z. Yang, "Optomechanical force estimation using passive micromanipulator end-effectors," *2016 International Conference on Manipulation, Automation and Robotics at Small Scales (Marss)*, p. 5, 2016.
- [138] J. Marschewski, S. Jung, P. Ruch, N. Prasad, S. Mazzotti, B. Michel, and D. Poulikakos, "Mixing with herringbone-inspired microstructures: overcoming the diffusion limit in co-laminar microfluidic devices," *Lab on a Chip*, vol. 15, no. 8, pp. 1923–1933, 2015.
- [139] R. Soffe, S. Baratchi, M. Nasabi, S. Y. Tang, A. Boes, P. McIntyre, A. Mitchell, and K. Khoshmanesh, "Lateral trapezoid microfluidic platform for investigating mechanotransduction of cells to spatial shear stress gradients," *Sensors and Actuators B-Chemical*, vol. 251, pp. 963–975, 2017.
- [140] J. Pfetting-Micklich, S. Brinckmann, S. R. Dey, F. Otto, A. Hartmaier, and G. Eggeler, "Micro-shear deformation of pure copper," *Materialwissenschaft Und Werkstofftechnik*, vol. 42, no. 3, pp. 219–223, 2011.
- [141] J. Heinze, "Determination of diffusion-coefficients by electrochemical current-time measurements," *Berichte Der Bunsen-Gesellschaft-Physical Chemistry Chemical Physics*, vol. 84, no. 8, pp. 785–789, 1980.
- [142] A. M. Rashidi and A. Amadeh, "The effect of current density on the grain size of electrodeposited nanocrystalline nickel coatings," *Surface & Coatings Technology*, vol. 202, no. 16, pp. 3772–3776, 2008.
- [143] M. Ashby, "Designing architected materials," *Scripta Materialia*, vol. 68, no. 1, pp. 4–7, 2013.

-
- [144] M. F. Ashby, "The properties of foams and lattices," *Philosophical Transactions of the Royal Society a-Mathematical Physical and Engineering Sciences*, vol. 364, no. 1838, pp. 15–30, 2006.
- [145] V. S. Deshpande, M. F. Ashby, and N. A. Fleck, "Foam topology bending versus stretching dominated architectures," *Acta Materialia*, vol. 49, no. 6, pp. 1035–1040, 2001.
- [146] V. S. Deshpande, N. A. Fleck, and M. F. Ashby, "Effective properties of the octet-truss lattice material," *Journal of the Mechanics and Physics of Solids*, vol. 49, no. 8, pp. 1747–1769, 2001.
- [147] M. F. Ashby, "The mechanical-properties of cellular solids," *Metallurgical Transactions a-Physical Metallurgy and Materials Science*, vol. 14, no. 9, pp. 1755–1769, 1983.
- [148] J. Bauer, S. Hengsbach, I. Tesari, R. Schwaiger, and O. Kraft, "High-strength cellular ceramic composites with 3d microarchitecture," *Proceedings of the National Academy of Sciences of the United States of America*, vol. 111, no. 7, pp. 2453–2458, 2014.
- [149] M. Smith, Z. Guan, and W. Cantwell, "Finite element modelling of the compressive response of lattice structures manufactured using the selective laser melting technique," *International Journal of Mechanical Sciences*, vol. 67, pp. 28 – 41, 2013.
- [150] T. A. Schaedler, C. J. Ro, A. E. Sorensen, Z. Eckel, S. S. Yang, W. B. Carter, and A. J. Jacobsen, "Designing metallic microlattices for energy absorber applications," *Advanced Engineering Materials*, vol. 16, no. 3, pp. 276–283, 2014.
- [151] J. Tang, H. Wang, X. Guo, R. Liu, X. Dai, G. Ding, and C. Yang, "An investigation of microstructure and mechanical properties of uv-liga nickel thin films electroplated in different electrolytes," *Journal of micromechanics and microengineering*, vol. 20, no. 2, p. 025033, 2010.
- [152] M. Datta and D. Landolt, "Fundamental aspects and applications of electrochemical microfabrication," *Electrochimica Acta*, vol. 45, no. 15-16, pp. 2535–2558, 2000.
- [153] R. Lontas and J. R. Greer, "3d nano-architected metallic glass: Size effect suppresses catastrophic failure," *Acta Materialia*, vol. 133, pp. 393 – 407, 2017.
- [154] M. Hasegawa, G. Guillonneau, X. Maeder, G. Mohanty, J. Wehrs, J. Michler, and L. Philippe, "Electrodeposition of dilute ni-w alloy with enhanced thermal stability: Accessing nanotwinned to nanocrystalline microstructures," *Materials Today Communications*, vol. 12, pp. 63–71, 2017.
- [155] R. Abdel Karim, Y. Reda, M. Muhammed, S. El Raghy, M. Shoeib, and H. Ahmed, "Electrodeposition and characterization of nanocrystalline ni-fe alloys," *Journal of Nanomaterials*, vol. 2011, pp. 1–8, 2011.

Bibliography

- [156] E. Pellicer, A. Varea, S. Pané, K. M. Sivaraman, B. J. Nelson, S. Suriñach, M. D. Baró, and J. Sort, "A comparison between fine-grained and nanocrystalline electrodeposited cu-ni films. insights on mechanical and corrosion performance," *Surface & coatings technology*, vol. 205, no. 23-24, pp. 5285–5293, 2011.
- [157] V. V. N. Reddy, B. Ramamoorthy, and P. K. Nair, "A study on the wear resistance of electroless ni-p/diamond composite coatings," *Wear*, vol. 239, no. 1, pp. 111–116, 2000.
- [158] E. H. Williams, "Magnetic properties of copper-nickel alloys," *Physical review*, vol. 38, no. 4, pp. 828–831, 1931.
- [159] N. Yusop, N. Shariff, S. Chow, and A. Ismail, "Structural and electrical characterizations of cuni thin film resistors," *Procedia chemistry*, vol. 19, pp. 619–625, 2016.
- [160] H. Muta, K. Kurosaki, M. Uno, and S. Yamanaka, "Thermoelectric properties of constantan/spherical sio₂ and al₂o₃ particles composite," *Journal of alloys and compounds*, vol. 359, no. 1-2, pp. 326–329, 2003.
- [161] R. Y. Ying, P. K. Ng, Z. Mao, and R. E. White, "Electrodeposition of copper-nickel-alloys from citrate solutions on a rotating-disk electrode .2. mathematical-modeling," *Journal of the Electrochemical Society*, vol. 135, no. 12, pp. 2964–2971, 1988.
- [162] N. Ibl, "Electrodeposition of alloys, principles and practice. band i," *Angewandte Chemie*, vol. 76, no. 13, pp. 620–620, 1964.
- [163] E. Pellicer, A. Varea, S. Pane, B. J. Nelson, E. Menendez, M. Estrader, S. Surinach, M. D. Baro, J. Nogues, and J. Sort, "Nanocrystalline electroplated cu-ni: Metallic thin films with enhanced mechanical properties and tunable magnetic behavior," *Advanced Functional Materials*, vol. 20, no. 6, pp. 983–991, 2010.
- [164] R. Y. Ying, "Electrodeposition of copper-nickel-alloys from citrate solutions on a rotating-disk electrode .1. experimental results," *Journal of the Electrochemical Society*, vol. 135, no. 12, pp. 2957–2964, 1988.
- [165] S. Rode, C. Henninot, and M. Matlos, "Complexation chemistry in nickel and copper-nickel alloy plating from citrate baths," *Journal of the Electrochemical Society*, vol. 152, no. 4, pp. C248–C254, 2005.
- [166] S. Ahn, H.-Y. Park, I. Choi, S. Yoo, S. Hwang, H.-J. Kim, E. Cho, C. Yoon, H. Son, J. Hernandez, S. Nam, T.-H. Lim, S.-K. Kim, and J. Jang, "Electrochemically fabricated nicu alloy catalysts for hydrogen production in alkaline water electrolysis," *International journal of hydrogen energy*, vol. 38, no. 31, pp. 13493–13501, 2013.
- [167] A. Varea, S. Pané, S. Gerstl, M. Zeeshan, B. Özkale, B. Nelson, S. Suriñach, M. Baró, J. Nogués, J. Sort, and E. Pellicer, "Ordered arrays of ferromagnetic, compositionally graded cu₁-xni_x alloy nanopillars prepared by template-assisted electrodeposition," *Journal of Materials Chemistry C: Materials for optical and electronic devices*, vol. 1, no. 43, p. 7215, 2013.

- [168] R. G. Delatorre, M. L. Sartorelli, A. Q. Schervenski, A. A. Pasa, and S. Güths, “Thermoelectric properties of electrodeposited cuni alloys on si,” *Journal of applied physics*, vol. 93, no. 10, pp. 6154–6158, 2003.
- [169] P. Schürch, L. Pethö, J. Schwiedrzik, J. Michler, and L. Philippe, “Additive manufacturing through galvanofarming of 3d nickel microarchitectures: Simulation-assisted synthesis,” *Advanced Materials Technologies*, vol. 3, no. 12, p. 1800274, 2018.
- [170] G. B. Harris, “X. quantitative measurement of preferred orientation in rolled uranium bars,” *The London, Edinburgh and Dublin philosophical magazine and journal of science*, vol. 43, no. 336, pp. 113–123, 1952.

Appendix

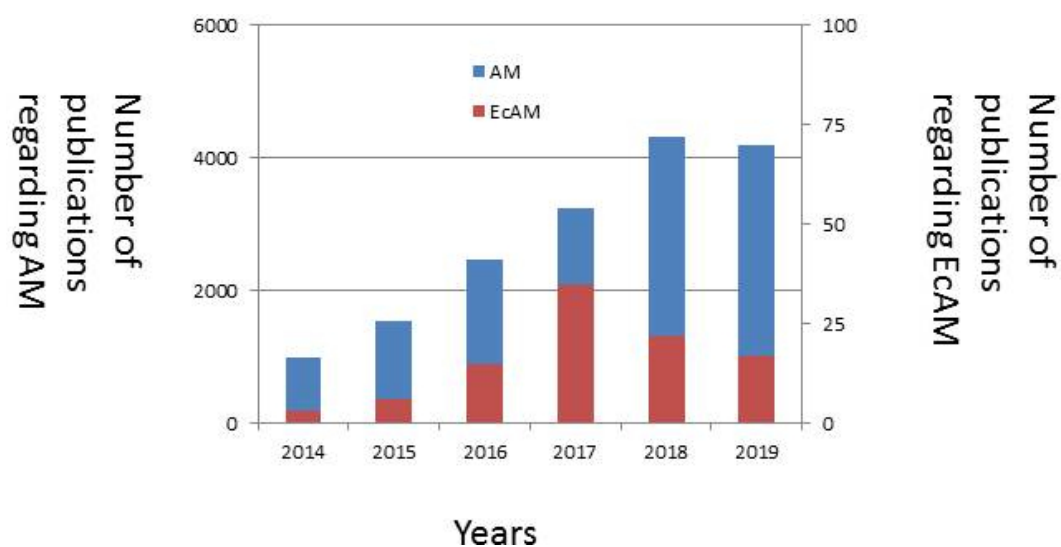


Figure 1 – Number of publications - Additive Manufacturing versus electrochemical additive manufacturing, gotten from Clarivate Analytics' Web of Science.

Initial concentration [molm^{-3}]	1300
System temperature [K]	333
Relative equilibrium potential [V vs Ag/AgCl]	-0.5
Temperature dependence of the equilibrium potential [VK^{-1}]	0
Cathode potential [V vs Ag/AgCl]	-1.2
Electrolyte potential at 100 μm distance from working electrode [V l]	-0.5
Diffusivity, Ni^{2+} [m^2s^{-1}]	$1.5 \cdot 10^{-9}$
Charge transfer coefficient: reduction	0.5
Charge transfer coefficient: oxidation	0.5
Conductivity [Sm^{-1}]	4.611
Exchange current density [Am^{-2}]	2.1

Table 1 – Electrodeposition simulation of the nc-nickel electrodeposition simulation

Appendix

Young's modulus [GPa]	173
Poisson ratio	0.34
Nickel density [kgm ⁻³]	8908

Table 2 – Mechanical testing simulation parameters for the nc-nickel microsprings

	single spring, pitch 2	spring array, pitch 1	spring array, pitch 2
Thickness top layer [μm]	2.1	2.2	2.0
Strut diameter [μm]	1.8	2	1.2
Overall spring diameter [μm]	6.0	6.0	6.0
Height of the helical part in the microspring [μm]	19.1	19.0	

Table 3 – Dimensions of the nc-nickel microsprings measured by SEM

Species in solution	Mol/l
Ni ²⁺	0.12
NiCit ⁻	0.18
NiHCit	1.90·10 ⁻⁹
Cu ²⁺	1.70·10 ⁻¹³
Cu ₂ Cit ₂ H ₂ ⁴⁻	0.36·10 ⁻¹
Cu ₂ Cit ₂ H ₁ ³⁻	0.40·10 ⁻²
CuHCit	2.20·10 ⁻¹⁰
Cit ³⁻	6.40·10 ⁻¹⁶
HCit ²⁻	4.80·10 ⁻¹⁴
H ₂ Cit ⁻	8.30·10 ⁻¹⁴
H ₃ Cit	3.35·10 ⁻¹⁵

Table 4 – Electrolyte Constituents of copper nickel electrolyte

Current density	-35 mA/cm ²		-60 mA/cm ²		-90 mA/cm ²	
at. % values	Ni	Cu	Ni	Cu	Ni	Cu
Full cross-section	35.5	65.5	45.0	55.0	57.0	43.0
Area 1	36.2	64.8	49.0	51.0	57.8	42.2
Area 2	35.3	64.7	46.9	53.1	57.6	42.4
Area 3	35.0	65.0	45.5	54.5	57.3	42.7
Area 4	34.5	65.5	44.5	55.5	56.3	43.7
Area 5	34.1	65.9	43.6	56.4		
Area 6	33.7	66.3	41.7	58.3		
Composition	Cu _{0.65} Ni _{0.35}	Cu _{0.57} Ni _{0.43}	Cu _{0.43} Ni _{0.57}			

Table 5 – EDX measurements of thin films deposited at different current density. The measurements were made in each section for the entire areas in figure 8.

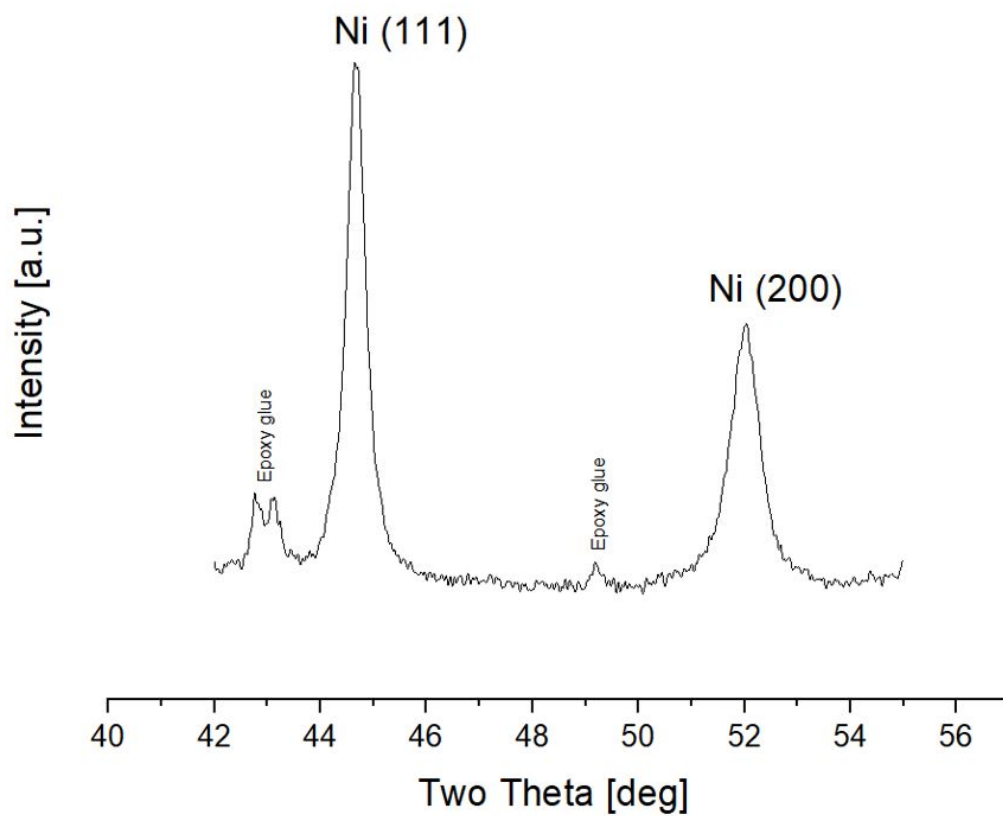
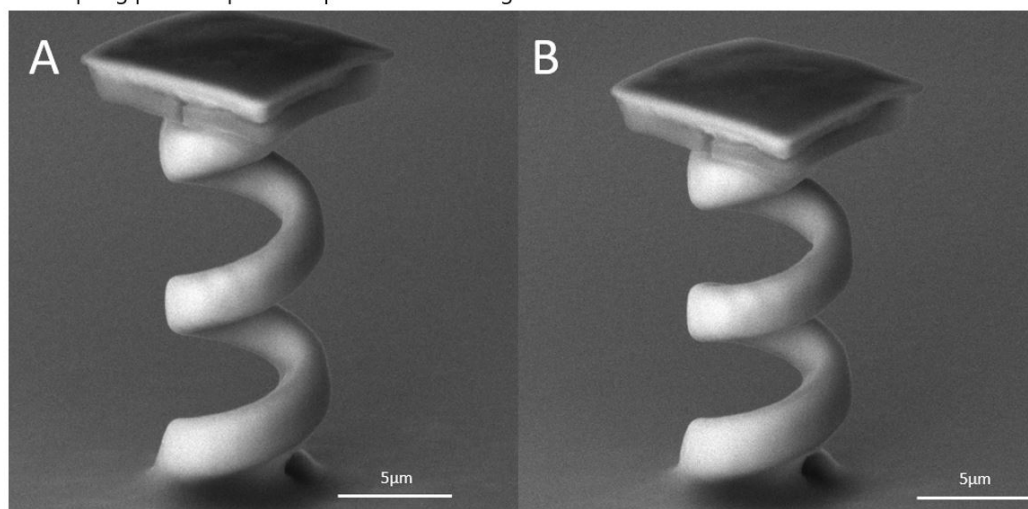


Figure 2 – Sample XRD showing nc-nickel and epoxy glue peaks

Microspring pre- and post-compression SEM images



A) Pre-compression testing

B) Post-compression testing

Figure 3 – nc-nickel microsprings pre and post compression

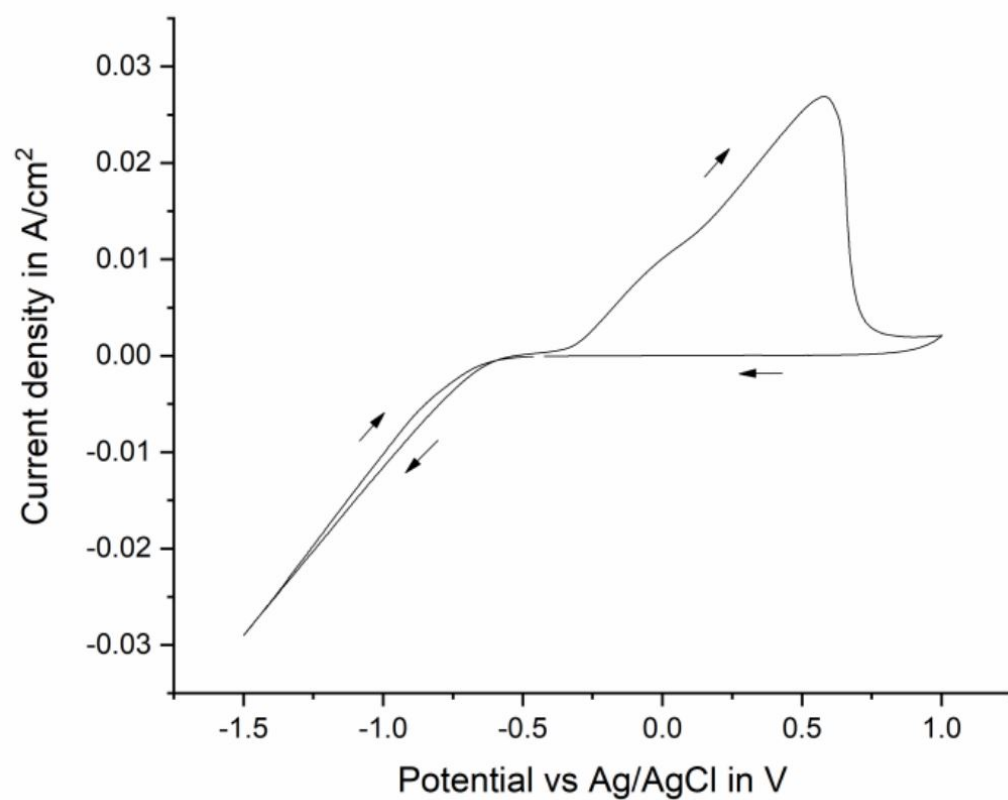


Figure 4 – Nickel sulfamate electrodeposition cyclic voltamogram performed at 5 mV/s

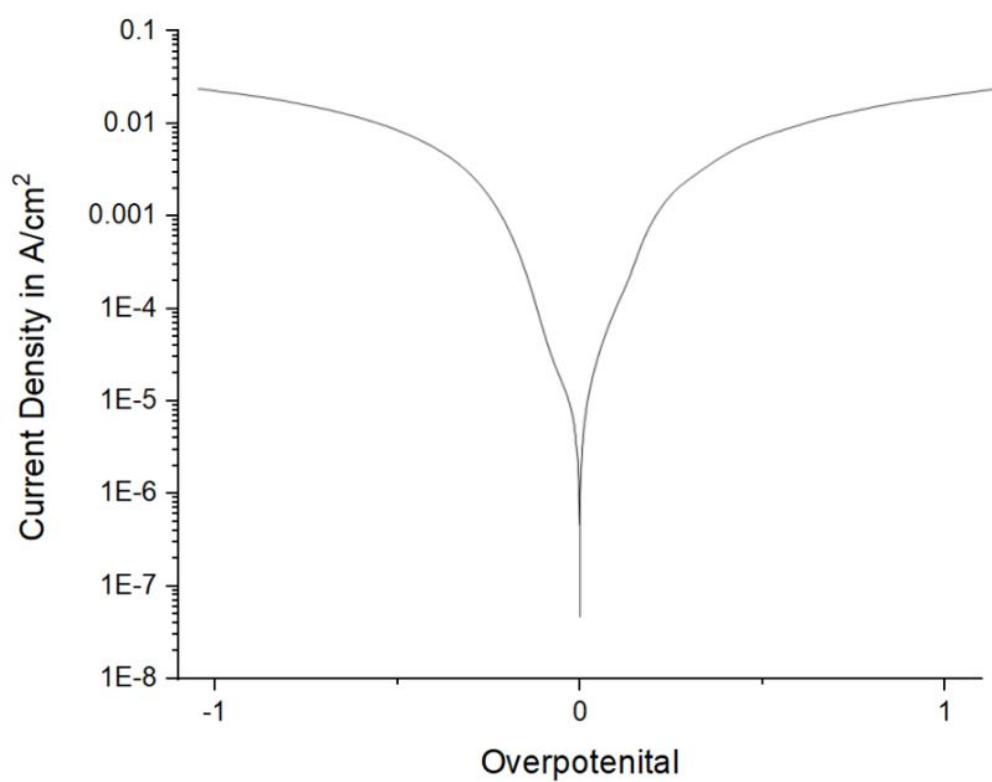


Figure 5 – Nickel sulfamate electrodeposition Tafel plot

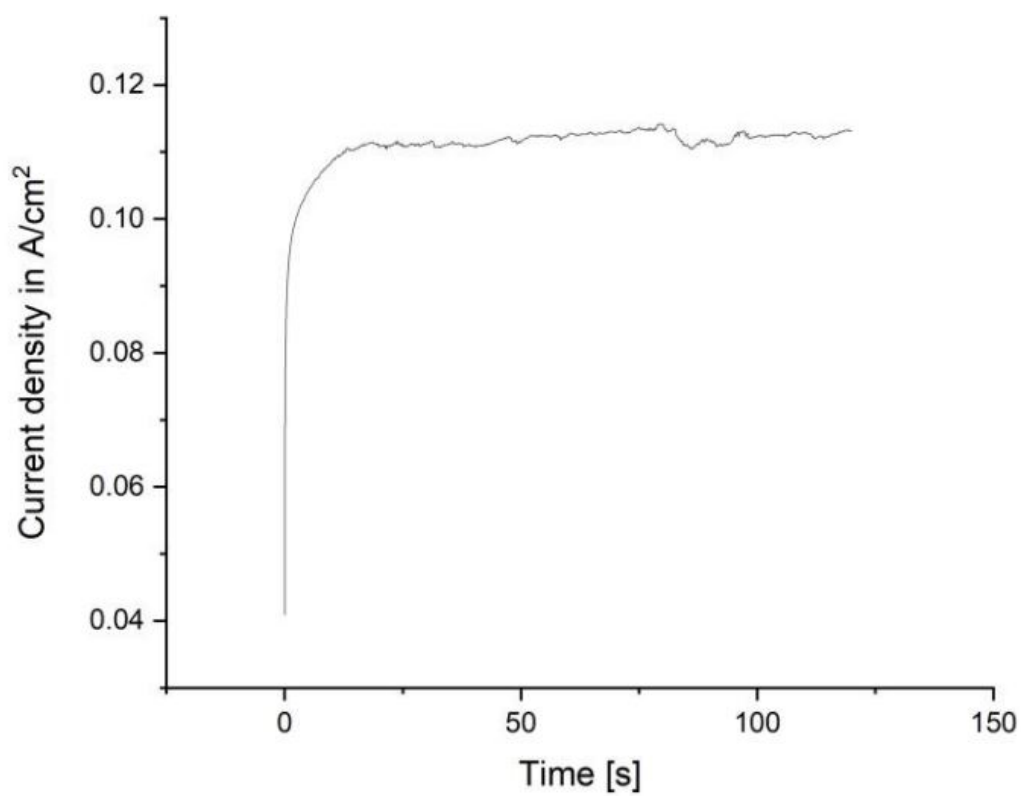


Figure 6 – Chronoamperometry of nickel sulfamate electrodeposition

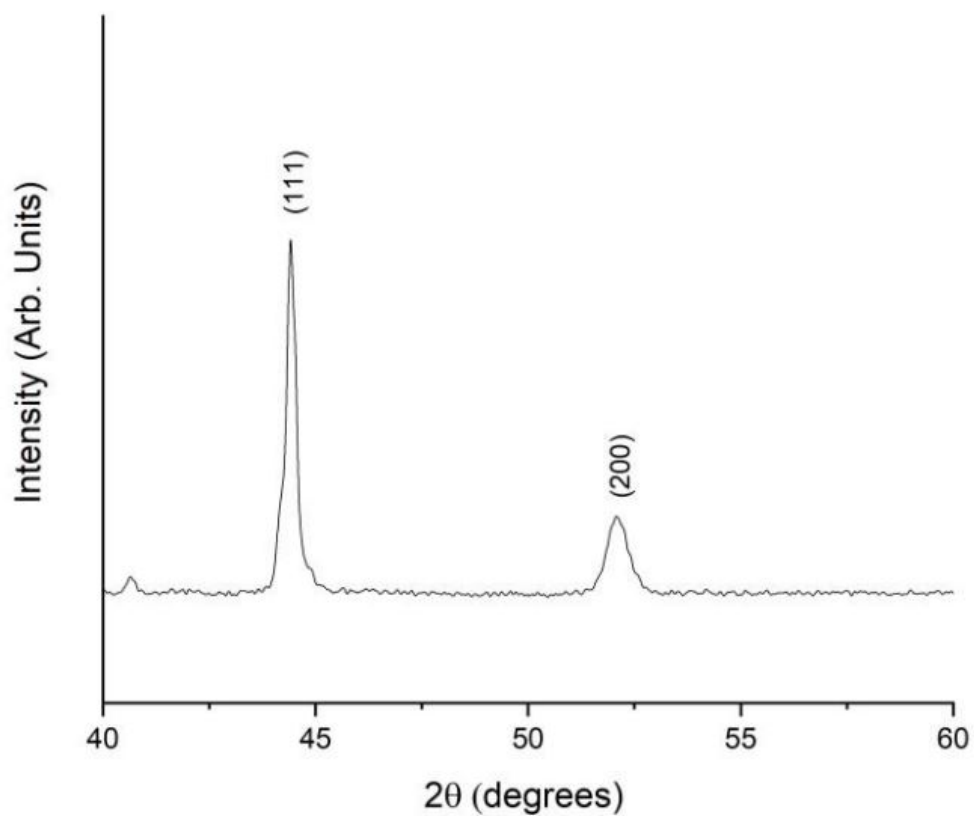


Figure 7 – XRD of nc-nickel microshear specimen on FTO-coated borosilicate glass.

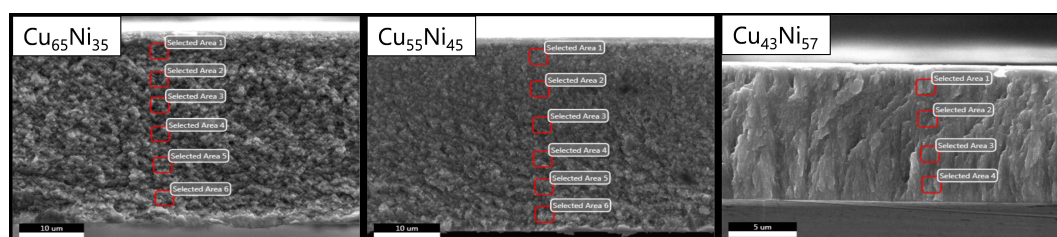


Figure 8 – EDX measurements of copper nickel thin film cross sections.

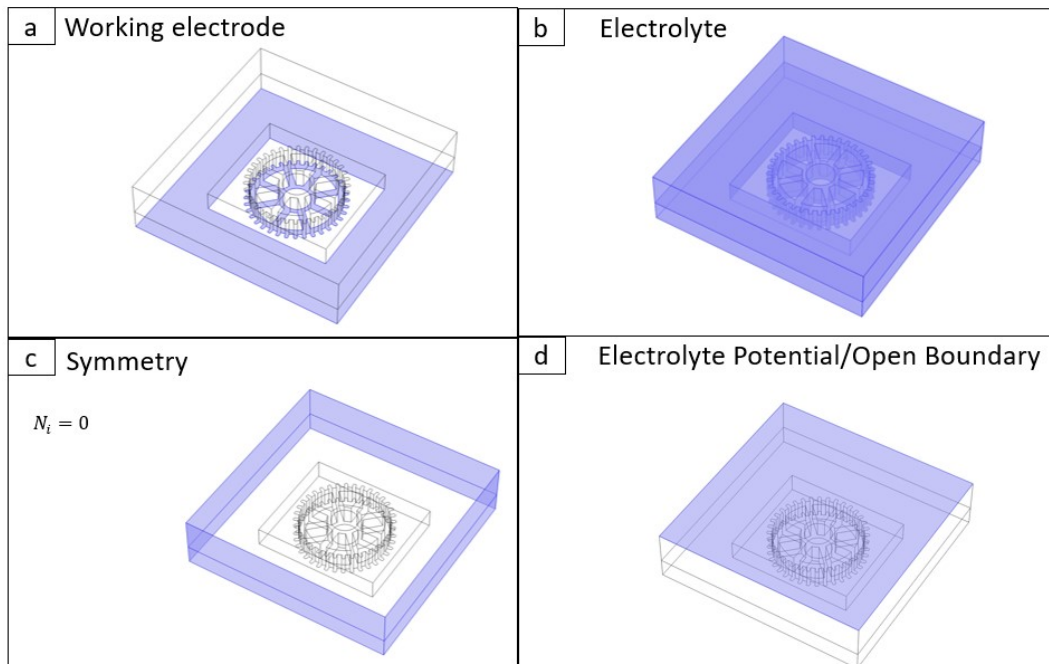


Figure 9 – Boundaries of the copper nickel micro-gear deposition simulation

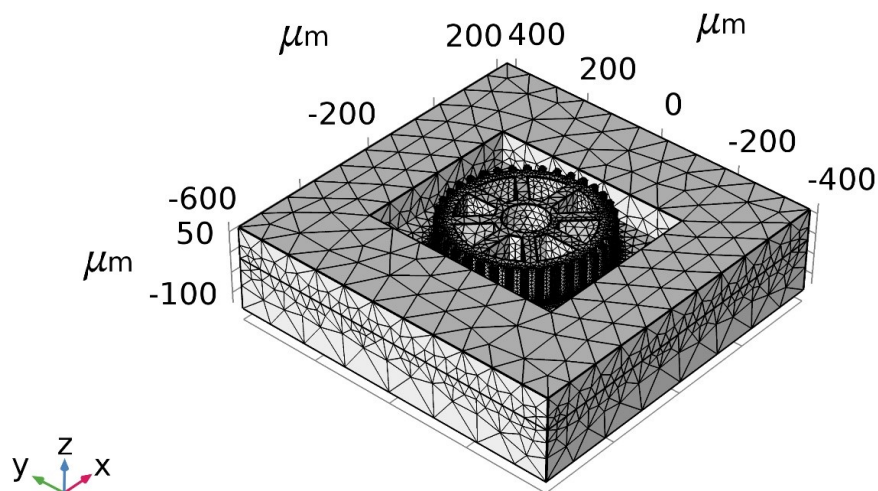


Figure 10 – FE Meshing of the copper nickel deposition simulation for the micro-gear

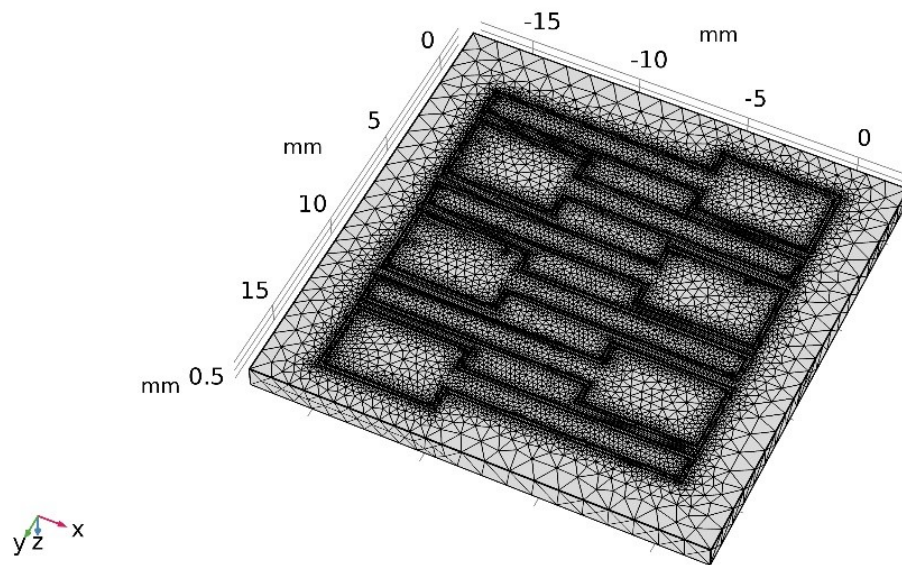


Figure 11 – FE Meshing of the copper nickel deposition simulation for the T-components

CV

Personal Information

Name: Patrik Schürch
Address: Neufeldstrasse 21
3012 Bern
Date of birth: 10.10.1990
Nationality: Swiss
Email: Patrik@schuerch.net
ORCID: 0000-0001-6816-8553

Education

01/2016 – Present: **EPFL Lausanne – EDMX Doctoral School**
Doctoral research student at EMPA, Thun
Project: Template-assisted electrodeposition and 3D electrodeposition modelling

09/2014 – 03/2015: **University of Bern, Switzerland**
Master of Science in Chemistry and Molecular Sciences with special qualification in Physical chemistry
Master thesis title: Electrodeposition of Bismuth chalcogenide nanowire arrays for the fabrication of thermoelectric microdevices

09/2010 – 08/2013: **University of Bern, Switzerland**
Bachelor of Science in Chemistry and Molecular Science

Employment history

01/2016 – Present: **Empa Thun**
Doctoral research assistant at Empa Thun in the laboratory of Mechanics of Materials and Nanostructures
Project: Template-assisted Electrodeposition
Supervisor: Dr. Laetitia Philippe and Prof. Frank Nüesch

03/2015 – 01/2016: **Empa Thun**
Master Thesis student at Empa Thun in the laboratory of Mechanics of Materials and Nanostructures
Project: Bismuth chalcogenide electrodeposition
Supervisor: Dr. Laetitia Phillippe and Dr. Peter Broekmann

09/2010 – 03/2015:

Trivadis IT, Bern

Part-time to full time position as database and GUI tester and documentation writer

08/2013– 08/2015:

Medi, Bern

Teaching of a class of 20-30 for the yearly "Introduction to Chemistry" course

Prizes, awards, fellowships

08/2017:

Best presentation award at the electrodeposition summer school in Schwäbisch-Gmünd organized by European COST-action e-MINDS.

Personal skills

Technical competences

- Electrochemical analysis (CV, LV, LSV, RDE, RRDE, IS)
- Electrodeposition methods (Potentiostatic, Galvanostatic, pulse deposition, reverse pulse deposition) for , Cu, CuNi, Au, Rh, Co, Zn, ZnO, WO₃
- Electroless Deposition (NiB)
- Template-assisted electrodeposition
- UV-Lithography via Mask aligner or direct laser writing
- Two-photon lithography
- Colloidal lithography via self-assembly
- Greyscale Lithography
- Scanning electron Microscopy with EDX
- X-ray diffraction in bragg-brenatno and gracing incidence configuration
- X-ray fluorescence
- UV/VIS spectroscopy of liquids and solids
- CAD design and 3D printing with macroscale 3D printers (Formlabs, Prusa)
- Computing: PLSQL; MATLAB; Mathematica; Autodesk Inventor; Blender; Origin; ImageJ, Windows office software

Language skills

- German: Native
- English: Proficient (Cambridge Certificate of Advanced English, 2010)
- French: Conversant
- Spanish: Beginner

Publication list:

Published:

- **Schürch, P.**; Pethö, L.; Schwiedrzik, J.; Michler, J. and Philippe, L. Additive Manufacturing through galvanofarming of 3D Nickel Microarchitectures: Simulation□Assisted Synthesis, *Advanced Materials Technologies* **2018**, 3 (12), 8.
- **Schürch, P.**; Ramachandramoorthy, R.; Pethö L.; Michler J and Philippe L., Template Additive Manufacturing by Template-assisted 3D Electrodeposition: Nanocrystalline Nickel Micro-springs and Micro-spring Arrays, *Applied Materials Today*, **2019**, p. 100472.
- Manzano, C. V.; **Schürch, P.**; Pethö, L.; Bürki, G.; Michler, J.; Philippe, L., High Aspect-Ratio Nanocrystalline CuNi T-Structures and Micro-Gears: Synthesis, Numerical Modeling and Characterization, *Journal of the Electrochemical Society* **2019**, 166 (10), E310-E316.
- Casari, D.; Pethö, L.; **Schürch, P.**; Maeder, X.; Philippe, L.; Michler, J.; Zysset, P.; Schwiedrzik, J., *Journal of Materials Research* **2019**, 34 (14), 2517-2534.

Submitted and in review:

- Second revision:
Schürch, P.; Philippe, L., Chapter 4.11 Composite metamaterials: types and synthesis, *Encyclopedia of Materials: Composites*, Elsevier, 2020
- Submitted:
Rohbeck, N.; Ramachandramoorthy, R.; Casari, D.; **Schürch, P.**; Edwards, T.; Schilinsky, L.; Philippe, L.; Schwiedrzik, J.; Michler, J., Effect of high strain rates and temperature on the micromechanical properties of 3D-printed polymer structures made by Two-Photon Lithography, *ACS Nano*